Proceedings of the Summer School 2011

Graduate School 1483

Process Chains in Production:
Interaction, Modelling and Assessment of Process Zones

Rüdiger Pabst, Volker Schulze (eds.)

KIT Scientific Publishing

Rüdiger Pabst, Volker Schulze (eds.)

Proceedings of the Summer School 2011

Graduate School 1483

Process Chains in Production: Interaction, Modelling and Assessment of Process Zones

Karlsruhe Institute of Technology

KIT SCIENTIFIC REPORTS 7611

Proceedings of the Summer School 2011

Graduate School 1483

Process Chains in Production:
Interaction, Modelling and Assessment of Process Zones

von
Rüdiger Pabst
Volker Schulze
(eds.)

Report-Nr. KIT-SR 7611

Preamble of publishers

In the last years the meaning of simulation of manufacturing technologies becomes more and more important. Strategies to simulation single manufacturing processes are already developed and often successfully implemented. Now it is necessary to link the individual simulation steps, in order to be able to reliably simulate complete process chains from the semi-finished material to the complete part. This is the central research idea of the Graduate School 1483. Simulation methods to describe, evaluate and optimize the state of component parts have to be developed for chained manufacturing processes and have to be verified by experimental investigations

Rüdiger Pabst
Volker Schulze

Index

Graduate School 1483
Process Chains in Production:
Interaction, Modelling and Assessment of Process Zones

Graduate School 1483

Broaching is a highly effective manufacturing method to create complex structures on inner or outer surfaces. It is characterized by short machining times, simple machine technique and high automation. To identify the effects of broaching on the components, experiments with different tools and cutting speeds have been performed on SAE 5120 low alloyed steel. Parts machined with determined sets of process parameters have been subjected to a subsequent case hardening step to show the effect of residual stress formation after broaching to potentials of distortion. In addition, the influence of the tool´s minor cutting edges to the formation of cutting forces has been shown.

1. Main areas of research

The importance of simulation for manufacturing engineering has risen over the past years. The vision of multi-scale and multi-process simulation promises major competitive advantages not only in factory and production planning, but also in product engineering. These advantages result from complex experimental studies for the identification of process parameters becoming redundant and from a significant reduction of product development times.

Strategies for the simulation of single isolated manufacturing processes are already highly advanced and have been widely and successfully implemented. Before simulation-based production process development can become a reality, though, two crucial development steps are yet to be completed: It must be possible to 1. link simulation steps so that entire process chains can be simulated with a high degree of reliability, and, 2. transfer the primary simulation result, i.e. the component condition, into a reliable prognosis for component behaviour under operating conditions.

The main research idea of the Research Training Group is to devise simulation methods for the description, evaluation and optimisation of component conditions in interlinked manufacturing processes and have them verified by means of experimental studies. This places the focus of research mainly on process chains ranging from semi-finished to finished components as opposed to previous research, which was mainly centred on process chains from the liquid phase to the semi-finished part.

The consistent combination of process and material modelling accompanied by the use of state-of-the-art methods of experimental process analysis and microstructural and mechanical component characterisation is expected to yield major advances in engineering with a high potential for industrial application.The general approach of the Research Training Group is to modell the process chains covering the transition from the semi-finished part to the finished component in all relevant process steps. The respective simulation chain is built up in parallel. For experiment and simulation to match, the evolution of the condition of the finished part or the component, respectively, is experimentally characterised. The complexity and dimension of the research issues at hand do not only render any attempts to model all possible process chains impossible. They make it an idle effort to begin with. Scientific excellence is accomplished by deliberately and exclusively concentrating on processes, materials and types of components for which there already is a broad basis of outstanding research skills and expertise among project applicants, and it is achieved by combining well-established basic processes and novel procedures promising great potential that are primarily

developed by the project applicants or the associated members of the Research Training Group. The research programme comprises three topic areas:

A. Process chains in sheet metal component manufacturing with main focus on steel as a material and the processes rolling, deep drawing and press hardening,

B. Combinations of different manufacturing processes for solid components with main focus on steel as a material and the process steps soft machining, case hardening, hard machining and surface treatments,

C. Simulation technologies for process chains with main focus on multi-scale and generic models, similarity mechanics and parallel algorithms.

2. A. Process chains in sheet metal manufacturing

High-strength steels and ultra-high-strength steels are of extraordinary importance, especially in the field of vehicle construction. The reason is that with these modern materials, a combination of both simple and functional car body concepts with a high innovation potential can be realized. The necessary process chain for the sheet metal manufacturing for modern car bodies is characterized by complex partial processes (milling, interstage annealing, deep drawing / press hardening), where each process step has a significant influence on the subsequent production steps and the material behavior. The forming process is often performed by deep drawing. Procedures like, e.g., press hardening, however, are more convenient, since they offer the possibility of adjusting the specific local characteristics. In order to be able to appropriately model the complexity of the process chain and the sheet metal manufacturing, the subject area A has been decomposed into six dissertation projects being closely interrelated by the following common aim: The description and optimization of the process chain of the sheet metal manufacturing based on advanced material models which allow to describe the evolution of the microstructure.

3. Combinations of different manufacturing processes for solid components

The linkage of different manufacturing processes within the process chain "soft machining – case hardening – hard machining – surface treatments" is supposed to be studied both experimentally and theoretically. The process of manufacturing a gearshift sleeve for a passenger car gearbox from case-hardening steel

20 MnCr5 will be the master process chain studied both experimentally and in simulation. This method allows for the development of interlinked models and for their validation through a comparison with experimentally determined process parameters and data from component characterisation concerning the component condition.

Existing single process models need to be extended by means of new approaches to the description of relevant mechanisms (e.g. cutting processes during machining) taking into consideration inhomogeneous starting conditions with depth gradients. These process models then need to be linked as required for their practical application. The multi-scale consideration ranging from local process impacts to the global component condition represents a particular challenge for modelling. If the material at hand is inhomogeneous without a depth gradient, the multi-phase structure increases the complexity if combined surface treatment processes are to be modelled. The Research Training Group aims to develop processes allowing for the component condition, e.g. the inherent stress and the solidification condition, to be transferred from a mesh of the entire component to a local mesh and vice versa in the form of condition variables for the purpose of taking into consideration the impact of premachining steps.

Validation will require experimental studies to be carried out for the systematic identification of these cause/effect relationships. They will help to obtain a more detailed understanding of these interdependencies and to verify the simulation results. These simulations are meant to not only facilitate the determination of optimum values for process parameters of individual processes but also for a combination of processes. These strategies will be validated in dissertations with a focus on production engineering. The setting of form and dimensions of a component prior to heat treatment, for example, is to allow for case hardening to produce components with near target dimensions and for hard machining efforts to be minimised. Another advantage is that through the combination of heat treatment and hard machining inherent compressive stress going very deep into the component surface layer can be made one of the optimisation goals. This makes available optimisation strategies aiming to improve process chain efficiency and the resulting component characteristics.

These aspects are also to be treated by the Research Training Group. Starting from local considerations, the qualitatively novel simulation approaches are to be transferred to components with complex surface geometries. Subsequently, the systematic optimisation of

component fatigue limits is to be achieved. To that end, a machining database is to be set up containing the main component characteristics in relation with prior manufacturing processes and taking into consideration local component geometries. Data are to be entered via interlinked simulation calculations which mainly take into consideration and adjust component curvatures, component thicknesses and initial surface layer conditions. The database will provide data on core and surface layer condition for the material and material conditions selected by the user. Non-available conditions required to evaluate a component can be obtained by initiating and evaluating the respective simulation calculations. Subsequently, the local component conditions are added to the components by means of finite element simulations, and their fatigue limits are assessed. The parameters of surface treatments, for example, are systematically varied until the best possible fatigue limit is achieved.

The calculation methods are to be verified by means of fatigue limit tests with grooved samples resembling the component and with components which have complicated and locally strongly curved surface geometries. This concept will allow for the unprecedented determination of surface treatment parameters for the achievement of optimum fatigue limits with components of any geometry.

4. Simulation technologies for process chains

Complex production processes are so far sub-divided in a sequence of controllable process steps. The result of each of these steps is an intermediate product with a sufficiently low variance of its properties. This low variance qualifies the intermediate product to serve as an input of a sub-sequent, independent production step.The process steps are characterised by accordingly specific conditions, which are reflected by corresponding microscopic models of the process progression, by corresponding macroscopic process control variables, by characteristic process observables and by specific resulting macroscopic part properties. The process control variable values of such process steps are determined from modelling and simulation with the goal to reach the required macroscopic properties of the intermediate product as precisely as possible. This view of disjoint process steps is not sufficient in the sense of an overall optimisation of the total pro

duction process. Instead, an overall model of the process chain is required, which captures the complex impact of –for instance- the microscopic properties on subsequent process steps. In the ideal case, a single process step would define an object, which represents all microscopic state quantities and models for its temporal evolution. The requirements on data (initial values and boundary conditions) determine the set of input data, which allow for a perfect simulation. From such a perfect simulation, the values of the process control variables can be derived, which guarantee, that the process step produces exactly the required result. Unfortunately, a major part of these input data is either missing or they come only with high uncertainty or even both. This implies, that the simulation is only capable of treating idealised conditions.

As a consequence the object representing a process step needs to possess methods for the abstraction from the microscopic models. These methods could either use the systematics of similarity analysis or they could extract the relations between observables and microscopic state variables via statistical and generic models and relate them by mathematical observer methods. The process step object requires also an impact model for the macroscopic process control quantities as well as optimisation methods to adapt them to the temporal process evolution. Additional object methods derive an on-line process assessment result from the observed process evolution. The object propagates all data (the received data and the generated data) completely to the subsequent object in a well-structured and standardised way. The input side of such an object now needs a filter component to select the input data relevant for its own processing purposes. This enables the object to have only one single interface to its predecessor but still to have access to all data of the previous process chain. To support the overall optimisation, a process step object should not only react to the previous chain elements, but also model the impact of its own control cycle on subsequent process steps.

5. Acknowledgement

Graduate School 1483
Process Chains in Production:
Interaction, Modelling and Assessment of Process Zones
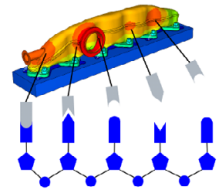
Experimental investigation of microstructure evolution in cold rolled DC04 sheet during annealing

P. Bienger[1,2], D. Helm[1]

1) Fraunhofer Institute for Mechanics of Materials IWM
2) Institute of Applied Materials Reliability of Components and Systems, KIT

The process chain for the production of sheet metal components is very complex and makes highest demands on its numeric description. At the beginning of the regarded process chain, a hot-rolling process is followed by cold-rolling. The microstructure of the material is strongly deformed in these process steps, whereby the macroscopic characteristics change. In order to prepare the material for the deep-drawing process, a heat treatment is required for activating recovery and recrystallization processes. The ferritic deep drawing steel DC 04 is investigated. Samples from a real process are taken before and after the heat treatment. These samples are investigated regarding their texture and the macroscopic behavior. These recrystallization experiments shall give information about the mechanisms during the heat treatment especially the texture change during the process. For these investigations EBSD and EDX is applied.

Texture evolution, recrystallization, carbides

1. Introduction

After casting, the process chain for the production of semi-finished sheet metals consists of different rolling. The process chain starts with a hot-rolling process, where the steel slab is rolled to a thickness, which is required for the following rolling steps. In the following cold-rolling process, the band is rolled almost to the final thickness and a deformation state is adjusted for controllingthe recrystallization behaviour with desired grain structure in the annealing process. After the annealing, the metal sheet is rolled to the final thickness in a skin pass mill. Therafter, the semi-finished product is manufactured by further forming proceses like deep drawing.

Due to the occurring finite plastic deformations and the accompanied increase in dislocation density during the cold rolling process, the grain structure is extremely deformed and the orientations of the grains are changed. In contrast to hot-rolled metals, the cold-rolled metals owns a state which leads to significant recrystallization by temperature rise. These are necessary to adjust the mechanical behaviors in the annealed material. For process optimization, it is essential to understand the combined process of cold-rolling and annealing: i.e. the microstructure evolution like grain orientation and also the resulting mechanical behavior. Only the detailed knowledge about the microstructural evolution allows the optimal design of such process chains.

The scope of this work is the investigation of the microstructure evolution during the annealing process. In chapter 2 the experimental setup is specified. Therafter, the results are reported and discussed in chapter 3..

2. Experimental setup

2.1. Material

The investigated material is a ferretic steel (DC 04) with a bcc structure. The material consists of iron and has typically the following alloying elements: carbon ($\leq$ 0.08 wt.%), manganese ($\leq$ 0.4 wt. %), phosphor ($\leq$ 0.03 wt. %), and sulphur ($\leq$ 0.03 wt. %) [1]. The thickness of the hot-rolled material is 3.1 mm. The thickness reduction during the industrial cold-rolling process is 62.9 % to the size of cold-rolled material of 1.15 mm.

2.2. Techniques for microstructure characterization

An electron microscope with electron back scattering diffraction pattern is used for the structural analysis of the material. The analyses were performed on sections parallel to the transverse direction of the rolled metal sheet. The TSL OIM Analysis software version 5 is used to analyse the measured data. The raw data were cleaned with an grain dilation algorithm. These algorithms compare neighbour points around the measurement error and record the orientation of the majority orientations into the error point. Additionally, the Energy Dispersive X-ray spectroscopy (EDX) technique is applied to analyse the chemical compostion. This method will be applied to determine the existence and role of carbides on the recrystallization process.

2.3. Annealing procedure

Different investigations on low alloyed ferritic steels (cf. [2]) have shown that recrystallization starts strongly above 600°C. Therefore, the annealing experiments are done by 600°C to investigate the recrystallization behavior. The annealing is executed in a furnace with oxygen atmosphere. Previous studies of the heating process show that the heating rate is too low to analyse the recrystallization process, because recovery processes occur. First tests in air show that 120 seconds decay until the annealing temperature is reached. In order to suppress the recovery processes, the heating time of the sample must be much faster. Therefore, the samples are pressed between massive steel plate and the recrystallization temperature is reached within in 25 seconds. After reaching the annealing time, the sample are quenched in water.

3. Experimental results

3.1. Initial microstructure after cold rolling

During the cold-rolling process, the material and its microstructure is highly deformed. The grains deforms from nearly globular to ellipsoidal shaped grains with an aspect ration greater than 8.5. Figure 1 shows the grain average missorientation of the investigated sample. Blue lines are grainbounderies with a missorientation angle large than 15 degree, green lines are between 5 and 15 degree, and red lines shows angles smaller than 5 degree. After cold rolling, a typical bcc rolling texture is observed (s. figure 2). The material shows a preferred orientation in {111} direction.
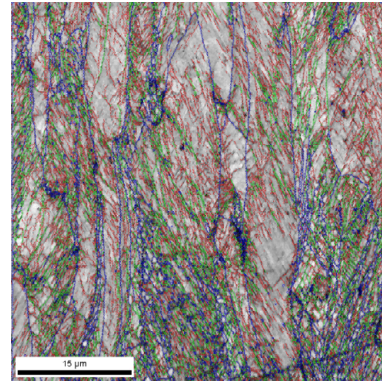
Figure 1: Grain morphology after cold rolling
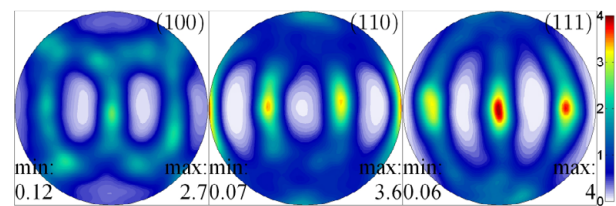
Figure 2: Pole figures after cold rolling

3.2. Morphology and texture evolution during the annealing processes

Using the optimized experimental set-up (cf. section 2.3), different annealing times are carried out. Thereafter, the microstructure is analyzed by using the EBSD method. To determine the fraction of recrystallized area, the grain average missorientation is plotted (s. figure 3). The areas with no miss¬orientations inside a grain are inendified as fully recrystallized grains. For the annealing temperature of 600°C, the fraction of recrystallized area is depicted in figure 4.
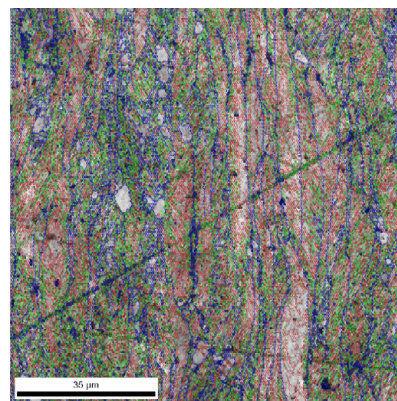
Figure 1: Partially recrystallized sample

The expected recrystallization values are fitted with the Johnson-Mehl-Avrami-Kologorov (JMAK) model [3]

$$A(t) = 1 - e^{-\beta \cdot t^n}.$$

The Parameter β is set to 0.0081 and n to 0.9997 to get the best fit of the model with the experimental data. The experiments show an incompleted recrystallization with an area fraction of 81.9 % after 900 seconds of heat treatment (figure 4). Experiments with higher temperatures show the same effect: A recrystallization fraction of 92.2 % is detected at 630 °C and 95.4 % at 700 °C.
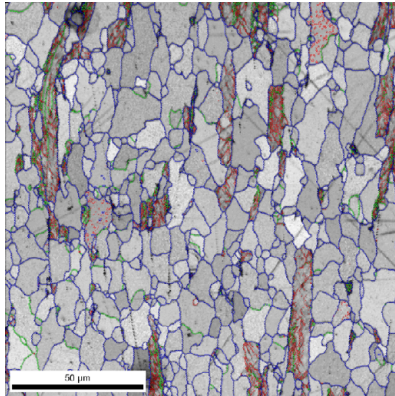
Figure 4: Incomplete recrystallization after 900 seconds
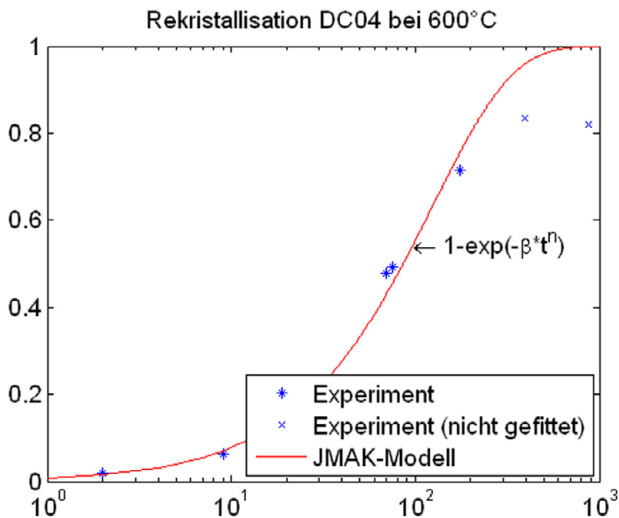
Figure 5: Fraction of recrystallized area vs. time at an annealing temperature of 600°C

The comparison between the experimentally annealed specimens and the samples of the real process chain shows some differences (figure 6) in the final annealing texture. Most notably, the {100} and {111} pole figures differ. One reason could be the fact, that the experimentally annealed samples are not fully recrystallized. It is to be that the texture changes in the last few percents of recrystallization.
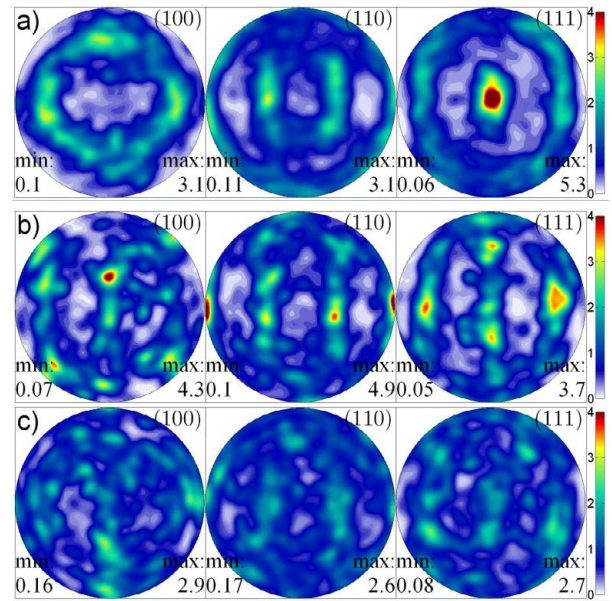
Figure 6: Polfigures of annealed material (a) Process, (b) 600 °C, (c) 630 °C

3.3. EDX analysis of the annealed samples

In order to clarify the physical reason for the observed incomplete recrystallization, further investigations at non-recrystallized areas has been performed. Based on the physical understanding and the published knowledge (cf. [4]), the existence of carbides could be responsible for the incomplete recrystallization. Due to the size of the expected carbides, the microstructural investigations are carried out at a higher resolution. The investigated sample is annealed at 600°C for 900 seconds. Figure 7 shows an Forward Scatter Detector (FSD) image of the sample with deformed grains surrounded by recrystallized grains. The dark spots on the grain boundaries suppose to be carbides.
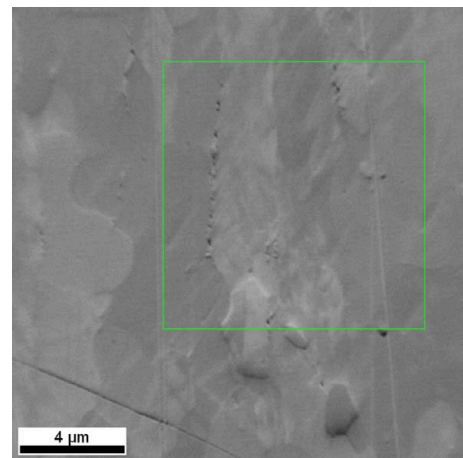
Figure 7: FSD image of the investigated grain structure

7

A coupled EBSD-EDX scan provides information about the grain orientation and the element distribution. Figure 8 shows the grain orientations of the sample. In the middle of the picture, non-recrystallized grains and are surrounded from fully recrystallized grains. The map shows, that the recrystallization stops at the grain boundaries and that the grains in the middle do not recrystallize into each other.
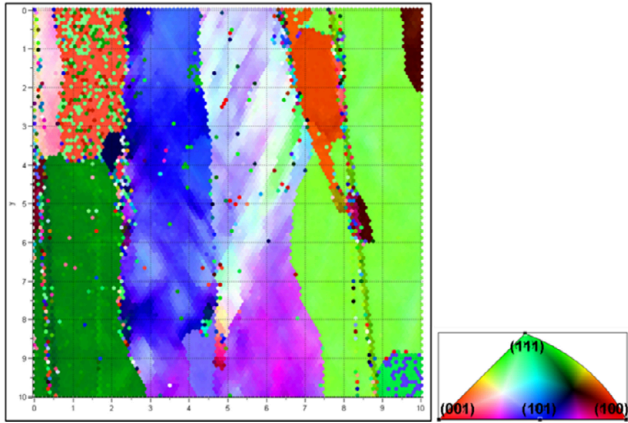
Figure 8: Inverse polfigure of the investigated area

For the detection of the carbides a EDX map is done. It shows the distribution of the detected element carbonate (figure 9). The EDX method shows a higher concentration of carbonate on the same location as the FSD map shows the dark spots. The increase of the carbnate on the grain boundaries is plotted in a darker colour.
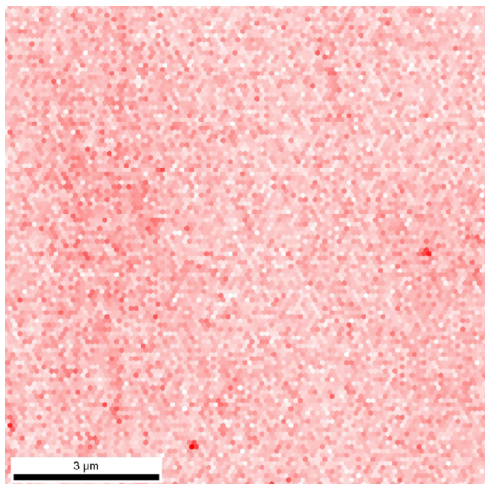
Figure 9: Distribution of carbon

3.4. Discussion

As expected, the experimental observation shows a connection between temperature and annealing time. Higher temperature accelerates the recrystallization process and the area fraction of recrystallized grains rises. Depending on temperature, the recristsallisation process stops due to inhomogenities in the microstruacture,. The EDX measurements indicate on carbides on grain boundaries. This carbides seem to be suppress the grain boundary mobility and therefore constrain the recrystallization. The recrystallized grains cannot grow over these boundaries. The recrystallization stops and the stored energy of the remaining grains are to low to recrystallize.

At temperatures above the A1-A3-line carbides disband and the carbon solute into the iron atom lattice [5]. Therefore an almost complete recrystallization seems to be feasible at temperatures above A1-A3-line.

4. Acknowledgement

5. References

[1] Wegst, C. Stahlschlüssel, 2007, volume 21, ISBN 978-3-922599-24-1

[2] Martinez-deGuerenu, A., Arizti, F., Diaz-Fuentes, M., Gutierrez, I., 2004, Recovery during annealing in a cold rolled low carbon steel. Part I: Kinetics and microstructural characterization, Acta Materialia 52, p. 3657-3664

[3] Fanfoni, M., Tomellini, M., 1998, The Johnson-Mehl-Avrami-Kologorov model: A brief review, Il Nuovo Cimento D, volume 20, p 1171-1182

[4] Belyakov, A., Wei, F.G., Tsuzaki, K., Kimura, Y., Mishima, Y., 2007, Incomplete recrystallization in cold worked steel containing TiC, Materials Science and Enineering, A 471, p 50-56

[5] Maxwell, H. L., Hayes, A., 1926, The free energy and heat of formation of iron carbide for the temperature interval 650° to 700°, Journal of the American Chemical Society, 48(3), p 584-593

Graduate School 1483
Process Chains in Production:
Interaction, Modelling and Assessment of Process Zones
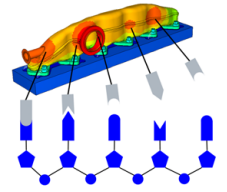
Micromechanical Modelling for Texture Evolution and Deformation Localization in Metal Forming Operations

Tung van Phan, Katja Jöchen and Thomas Böhlke

Institute of Engineering Mechanics, Chair for Continuum Mechanics, Karlsruhe Institute of Technology (KIT)
{tung, joechen, boehlke}@itm.uni-karlsruhe.de

A two-scale Taylor model for elastoviscoplastic polycrystals [7, 10, 11, 12] is applied to investigate the local and global mechanical behavior of a ferritic stainless DC04 steel. In the first step, the material parameters are estimated based on a two-scale simulation of fundamental tensile tests and subsequently used to simulate the local deformation behavior on the grain scale. A discretization procedure by finite elements and homogeneous displacement boundary conditions is applied to two-dimensional EBSD data in a grain scale simulation of the tensile test. The computed local grain reorientations are compared to experimental data at different states of elongation. In addition, by using the aforementioned micromechanical model, the strain localization is investigated and dicussed for different strain paths.

Crystal plasticity; Ferritic steel DC04; Taylor type homogenization; Forming limit diagram

1 . Introduction

The present work aims to describe and discuss the application of a large strain crystal plasticity model for a body-centered cubic (BCC) material (DC04 steel). The material parameters are estimated by uniaxial tensile tests and the crystallographic texture based on experimental electron backscatter diffraction (EBSD) data for a DC04 steel. Computational results using a two-scale Taylor model are compared with experimental tensile tests in terms of stress-strain curves to estimate the underlying material parameters. In order to validate the material model, we compare the local grain reorientation in a heterogeneous tension sample with experiments at different strain states by performing a full-field finite element (FE) simulation based on EBSD data. The two-dimensional EBSD data are discretized by finite elements and subjected to homogeneous displacement boundary conditions. For slip mechanisms, attention is focused on the combination of {110}<111> + {112}<111> slip systems [9]. In total, there are 24 slip systems of this type.

This paper is organized as follows. In Section 2 we discuss the constitutive equations of the large strain crystal plasticity model. The estimation of the material parameters obtained from the uniaxial tensile test simulation is given in Section 3. In Section 4, the grain scale simulation is discussed and described in detail. Finally, in Section 5, a formability prediction based on the two-scale model is analyzed by applying two classical localization criteria for different strain paths.

Notation. Throughout the text, a direct tensor notation is preferred. The scalar product and the dyadic product are denoted by $\boldsymbol{A} \cdot \boldsymbol{B} = \mathrm{sp}(\boldsymbol{A}^\mathsf{T} \boldsymbol{B})$ and $\boldsymbol{A} \otimes \boldsymbol{B}$, respectively. A linear mapping of 2nd-order tensors is written as $\boldsymbol{A} = \mathbb{C}[\boldsymbol{B}]$. Symmetric and traceless tensors are designated by a prime, e.g., $\boldsymbol{A}'$.

2 . Constitutive Equations

The deformation gradient can be decomposed multiplicatively into an elastic part $\boldsymbol{F}_e$ and a plastic part $\boldsymbol{F}_p$

$$\boldsymbol{F} = \boldsymbol{F}_e \boldsymbol{F}_p, \qquad (1)$$

combined with an elastic law and a flow rule. The elastic law is given by

$$\boldsymbol{\tau} = \boldsymbol{F}_e \tilde{\mathbb{C}}[\boldsymbol{E}_e]\boldsymbol{F}_e^\mathsf{T}, \qquad (2)$$

with $\boldsymbol{\tau}$ the Kirchhoff stress tensor, $\boldsymbol{E}_e = (\boldsymbol{C}_e - \boldsymbol{I})/2$ Green's strain tensor, $\boldsymbol{C}_e = \boldsymbol{F}_e^\mathsf{T} \boldsymbol{F}_e$ the right (elastic) Cauchy-Green tensor and $\tilde{\mathbb{C}}$, respectively the stiffness tensor in the reference system.

The plastic flow is governed by an evolution equation for the plastic part of the deformation gradient

$$\dot{\boldsymbol{F}}_p \boldsymbol{F}_p^{-1} = \sum_{\alpha=1}^{24} \dot{\gamma}_\alpha \tilde{\boldsymbol{M}}_\alpha, \qquad (3)$$

$$\dot{\gamma}_\alpha(\tau_\alpha, \tau^C) = \dot{\gamma}_0 \mathrm{sign}(\tau_\alpha) \left| \frac{\tau_\alpha}{\tau^C} \right|^m, \qquad (4)$$

where the exponent m quantifies the strain-rate sensitivity of the material, $\dot{\gamma}_0$ is the reference slip rate and τ^C denotes the critical resolved shear stress. For each slip system α, the resolved shear stress is computed by

$$\tau_\alpha = \boldsymbol{T}_e' \cdot \tilde{\boldsymbol{M}}_\alpha, \qquad (5)$$

where $\boldsymbol{T}_e = \boldsymbol{C}_e \boldsymbol{S}_e^{2\mathrm{PK}}$ is the Mandel stress tensor with the second Piola-Kirchhoff stress tensor $\boldsymbol{S}_e^{2PK} = J \boldsymbol{F}_e^{-1} \boldsymbol{\tau} \boldsymbol{F}_e^\mathsf{T}$. $J = \det(\boldsymbol{F}_e)$ is the determinant of $\boldsymbol{F}_e$. The slip system tensors $\tilde{\boldsymbol{M}}_\alpha = \tilde{\boldsymbol{d}}_\alpha \otimes \tilde{\boldsymbol{n}}_\alpha$ are rank-one tensors, where $\tilde{\boldsymbol{d}}_\alpha$ are the slip directions and $\tilde{\boldsymbol{n}}_\alpha$ are the slip plane normals. Additionally, a rate-dependent Kocks-Mecking hardening model [7]

$$\dot{\tau}^C(\tau_\alpha, \tau^C) = \Theta_0 \left(1 - \frac{\tau^C}{\tau_V^C(\tau_\alpha, \tau^C)}\right) \dot{\gamma}\left(\tau_\alpha, \tau^C\right) \quad (6)$$

is used, where the critical Voce stress is

$$\tau_V^C\left(\tau_\alpha, \tau^C\right) = \tau_{V0}^C \left| \frac{\dot{\gamma}(\tau_\alpha, \tau^C)}{\dot{\gamma}_0^*} \right|^{\frac{1}{n}}, \qquad (7)$$

with the asymptotic critical resolved shear stress τ_{V0}^C, the initial hardening modulus Θ_0, the hardening exponent n and $\dot{\gamma}(\tau_\alpha, \tau^C) = \sum_{\alpha=1}^{24} |\dot{\gamma}_\alpha(\tau_\alpha, \tau^C)|$. The initial conditions for these ordinary differential equations are $\boldsymbol{F}_e(0) = \boldsymbol{Q}_0 \in SO(3)$, and the initial critical resolved shear stress $\tau^C(0) = \tau_0^C$. The crystal orientation with cubic symmetry is defined by mapping the orthonormal basis $\boldsymbol{e}_i$ onto the orthonormal crystallographic basis $\boldsymbol{g}_i$, described by a proper orthogonal tensor $\boldsymbol{Q} = \boldsymbol{g}_i \otimes \boldsymbol{e}_i$. The initial orientation of the single crystal $\boldsymbol{Q}_0 = \boldsymbol{g}_i(0) \otimes \boldsymbol{e}_i$ is defined in terms of the orthonormal lattice vectors $\boldsymbol{g}_i(0)$ at the time $t = 0$.

3 . Estimation of material parameters based on tensile test

In this section, a crystallographic texture data set representatively reduced [13] from the EBSD measurements is applied to simulate uniaxial tensile tests of a sheet of heat treated DC04 steel. The two-scale Taylor model taking into account the reduced crystallographic texture at integration points is used to perform FE uniaxial tensile simulations. Computed tensile stress-strain curves are compared to the experiment at the macro level and shown in Figure 1. The experimental data are provided by Project A6 (Research Training Group GRK1483). An estimated set of material parameters is summarized in Tables 1 and 2.
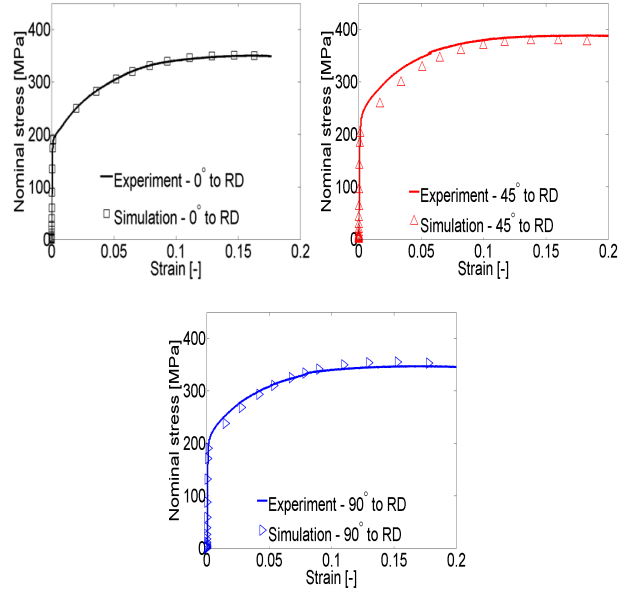
Figure 1: Uniaxial tensile stress-strain curves for different angles to rolling direction (RD).

C_{1111} [Gpa]	C_{1122} [GPa]	C_{1212} [GPa]
231.5	135.0	116.0

Table 1: Elastic constants of DC04 steel, see, e.g. [8].

τ_0^C [MPa]	67
τ_{V0}^C [MPa]	130
Θ_0 [Mpa]	755
m [-]	20
$\dot{\gamma}_0$ [1/s]	0.001
n	5

Table 2: Material parameters for the flow and hardening rule.

4 . Grain scale simulation

By using the MTEX toolbox [14], the EBSD-data file was imported and processed to receive a computable 2D grain structure shown in Fig. 2. After the FE discretization of the grain structure, it is subjected to homogeneous displacement boundary conditions describing a tensile test. A comparison of the local grain reorientation between the experiment and FE simulations is shown in Fig. 3 for three selected local grains at different states of deformation. In average, the local grain reorientation in the FE simulations agrees qualitatively with the experiment. However, the simulations do not sufficiently reproduce the heterogeneity of the reorientation distribution in the grain. This can be explained by the neglection of the 3D interaction of the three-dimensional microstructure in the 2D simulations.
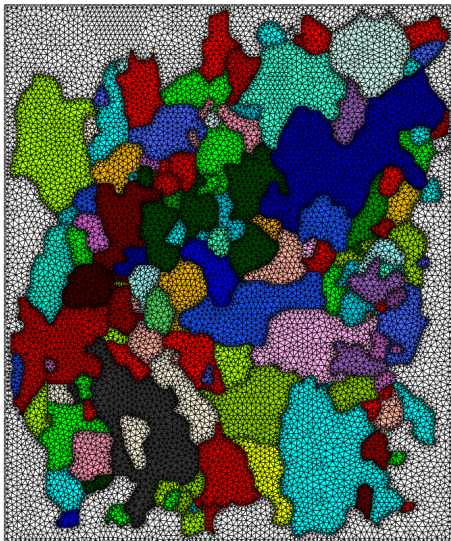
Figure 2: Mesh generation of a heterogeneous sample cut from a tensile specimen.

5 . Grain scale simulation

In order to evaluate the formability of sheet metals, the prediction of forming limit diagrams (FLDs) needs to be considered. proposed and investi-
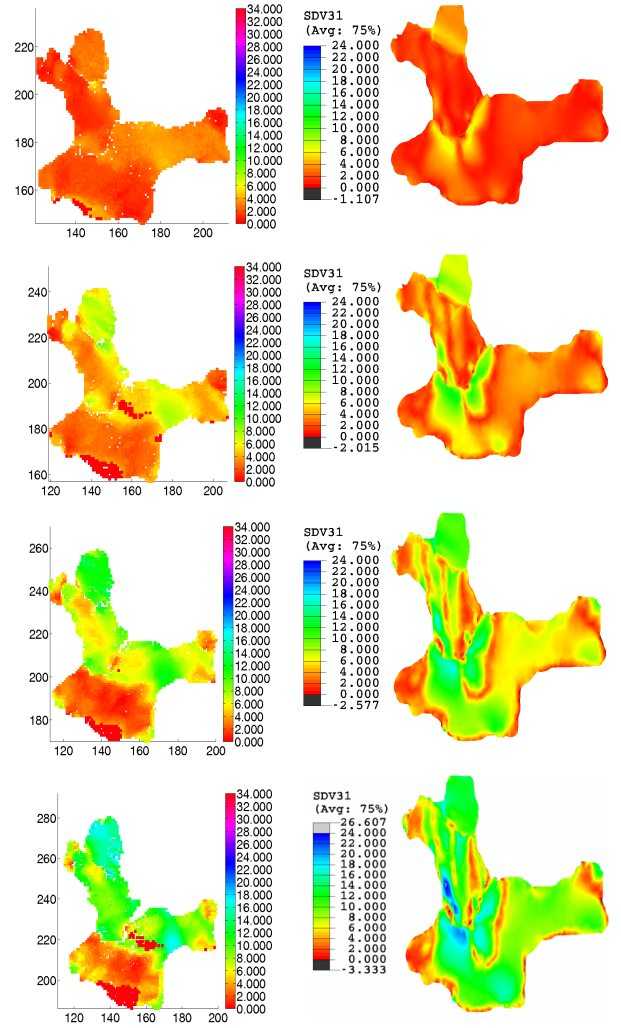
Figure 3: Local grain reorientation (degree) at the state of 5%, 10%, 15% and 20% deformation: (left) Experiment (Project A6, Research Training Group GRK 1483) and (right) FE simulations using {110}+{112}<111> slip systems.

gated by [1, 2, 3, 4, 6] for various materials, the forming limit curves can be used to predict metal forming behavior in industrial manufacturing processes. For a given sheet material, a forming limit diagram (FLD) is the curve representing strain localization [2, 4, 6] in strain space using the major strain ε_1 and the minor strain ε_2 at failure (Fig. 4).

In this contribution, two criteria are considered in the localization analysis to determine the FLD (see, e.g., Chapter 5, [5]). In the positive minor strain region ($\varepsilon_2 > 0$) of the FLD, criterion 1 is established based on the maximum of the stress power per unit volume. This corresponds to the maximum force criterion by Hill [1]. In the negative minor strain region ($\varepsilon_2 < 0$), criterion 2 is based on the maximum tension T (membrane stress). The relation of macroscopic principal strains is given by

$$\varepsilon_2 = \rho\varepsilon_1, \qquad (8)$$

where each strain path is specified by the ratio $\rho \in [-1/2, 1]$. Both criteria are applied in FE simulations based on a Taylor-type polycrystal model accounting for the aforementioned crystallographic texture data at integration points. By rotating the texture 0°, 10°, 20°,..., 90° about the normal direction (ND), 10 computed forming limit curves are obtained. In Fig. 4, the lowest localization point for fixed ρ is shown. The applied simple localization criteria correspond to conservative localization estimations for diffuse necking.
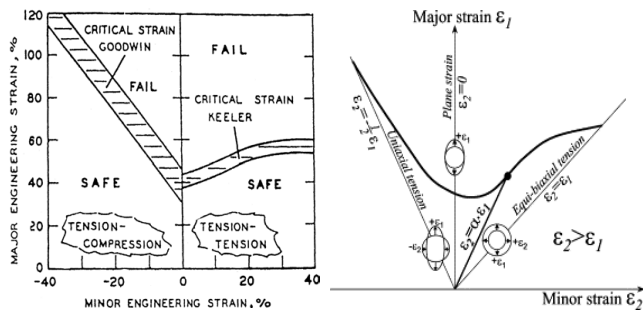
Figure 4: Forming limit diagrams [2, 4, 6].
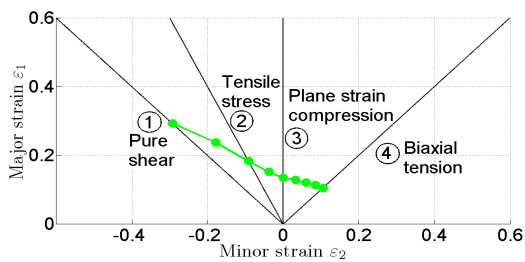
Figure 4: Predicted lowest bound of FLD.

6 . Summary and conclusions

In this paper, a finite strain crystal plasticity model for BCC materials is described, which has been implemented in ABAQUS. The single crystal orientations extracted from 2D EBSD data of a heat treated DC04 steel were used in the two-scale simulation. This study illustrates how the real texture data can be incorporated into a continuum mechanical modelling of sheet metal forming processes.

In the first step, a comparison of the crystal plasticity FE simulation with the experimental tensile test for the uniaxial stress-strain curve has been presented. The material parameters have been estimated based on these simulations.

The second step demonstrated the validation of the material model by a full field FE simulation based on a 2D EBSD data set under a tensile load. The average reorientation of the grains is very well reproduced. Due to the lack of experimental 3D data, the heterogeneity of reorientation is underestimated.

In the last step, the formability limit prediction has been presented for different strain paths using real texture information in Taylor-type simulations. The FLD result obtained by the suggested scheme corresponds to a conservative estimation of diffuse necking.

7 . Acknowledgement

8 . References

[1] Hill, R., Journal of the Mechanics and Physics of Solids 1, 19-30 (1952).

[2] Keeler, S. P., Backofen W. A., Transactions of the American Society for Metals 56, 25–48 (1963).

[3] Marniciak, Z., Kuczynski, K., International Journal of Mechanical Sciences 9, 609–620 (1967).

[4] Goodwin G. M., Society of Automotive Engineers No. 680093, 380–387 (1968).

[5] Marciniak Z., Duncan J. L., Hu S. J., Mechanics of sheet metal forming. Butterworth-Heinemann (2002).

[6] Viatkina, E. M., Brekelmans, W. A. M., Geers, M. G. D., Journal of Materials Processing Technology 168, 211–218 (2005).

[7] Böhlke, T., Risy, G., Bertram, A., Computational Material Science 32, 284–293 (2005).

[8] S. A. Kim, W. L. Johnson, Material Science and Engineering A 452-453, 633-639 (2007).

[9] Yalcinkaya T., Brekelmans W. A. M. and Geers M. G. D., Modelling and Simulation in Material Science and Engineering 16(8), 085007 (16pp), (2008).

[10] Schulze, V., Bertram, A., Böhlke, T., Krawietz, A., Technische Mechanik Band 29, Heft 2, 135–159 (2009).

[11] Böhlke, T., Jöchen, K., Kraft, O., Löhe, D., Schulze, V., Mechanics of Material 42, 11–23 (2010).

[12] T. V. Phan, K. Jöchen, T. Böhlke, ESAFORM Conference Proceedings by AIP, Volume 1353, 1215–1219 (2011).

[13] Jöchen, K., Böhlke, T., Proceedings of 10th International Conference on Technology of Plasticity (ICTP), 848-853 (2011).

[14] MTEX quantitative texture analysis software – a Matlab toolbox. http://code.google.com/p/mtex/

Graduate School 1483
Process Chains in Production:
Interaction, Modelling and Assessment of Process Zones
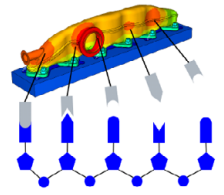
3D Phase-Field Simulation of Static Recrystallization with Stored Energy Driving Forces and Nuclei Selection

A.Vondrous, M. Selzer, B. Nestler

Institute of Materials and Processes, Hochschule Karlsruhe - Technik und Wirtschaft

The prediction of microstructure evolution during static recrystallization after metal working processes permits a reduction of manufacturing costs and enables reliable material property determination. Measurements of microstructure and mechanical properties at certain time steps during processing is difficult and ressource intense. With our combined simulation approach, we provide insight into the correlation of microstructure changes and macroscopic properties. We simulate static recrystallization of cold rolled steel sheets on a microstructure scale. To reconstruct the structure, we incorporate data from mapped 3D finite element crystal plasticity simulations with voronoi tesselation on a regular finite difference grid. The obtained distribution of dislocation densities and crystal orientations is used to identify nuclei depending on the amount of stored work. The phase-field energy functional is extended by an energy density term which enables nucleated grains to grow. The growth is influenced by the crystal orientations between the grains and by the amount of stored energy at the interface of nuclei. Pole figures of the simulation results and experimental EBSD measurements are compared. A weakening of the strong cold rolling texture can be reproduced and characteristic microstructure properties are obtained.

phase-field, static recrystallization, stored energy

1. Introduction

Production and usage of sheet metal involves the knowledge of the material properties. Mechanical properties like deformability, ductility and strength are of great importance for manufacturers. These properties are influenced by many factors like the composition, the microstructure or the stored work. All of the parameters can change during processing. We address in this work the cold rolling process with subsequent annealing of DC04 steel sheet, which is common material in the automotive industry.

An increase in anisotropic mechanical properties after cold rolling can be derived from the prefered crystal orientations (texture). The anisotropic reaction on mechanical forces is visible at the microstructure level with pole figures. Cold rolling introduces dislocations (stored work) too, which decrease deformability. Dislocations are mainly responsible for a strengthening of the deformed sheet. To obtain the initial or similar properties of the sheet before rolling, annealing activates the recrystallization process, which "restores" the microstructure and "removes" the dislocations. The cold rolled sheet has to be heated to the recrystallization temperature, which depends on the material and the applied deformation. During recrystallization, nuclei form and start to grow. It is assumed, that the driving force for recrystallization is the stored work in form of dislocations.

Recrystallization is complex and occurs in diverse forms, such that the words restore and remove have to be interpreted with care. It is a very active field of research. Humphreys, Rollett, Doherty [1], Gottstein [2], Rios [3] and others provide a broad and deep understanding of the physical processes and the current understanding.

1.1. Simulation Techniques

Based on fundamental knowledge of recrystallization, scientists try to simulate and analyse the properties and dynamics. An analytical formulation named Johnson-Mehl-Avraimi-Kolmogerov [4] equation (JMAK) describes the volume fraction over time of the recrystallized grains. The only parameters are the

nucleation rate, the growth velocity and the JMAK exponent to describe the recrystallization process. With this tool, engineers are able to characterize their material behaviour. The limits of the JMAK model are to predict the microstructure and orientation distribution.

Methods like the Potts model, cellular automata, Vertex models or the phase-field method [5] can be applied to predict the microstructure or orientation distribution. The discussion about the advantages and disadvantages of the methods is not in the scope of this paper. But a common challenge for all simulations exists. It is difficult to measure and generate the starting condition for a big 3D domain and to validate the results, because of the large number of grains and accordingly large data sets to store.

It is possible to obtain the microstructure in 3D with EBSD (electron backscatter defraction) measurements in combination with a FIB (focused ion beam) to cut a sample. The disadvantage is the destruction of the sample, such that comparisons with simulation results are difficult. As important as the microstructure is the dislocation distribution or dislocation density to describe the driving forces for recrystallization. To obtain the properties without extensive measurements, deformation simulations with crystal plasticity models are utilized as proposed in [6] or [7].

1.2. Process Chain

We follow the current development and combine finite element deformation simulations with phase-field recrystallization simulations based on EBSD measurements. Our recrystallization simulation of prior cold deformed sheet metal is part of a virtual process chain, which consists of cold rolling and annealing.

A 3D crystal plasticity finite element simulation of a rolled microstructure produced by Pierre Bienger[i] serves as input data for our recrystallization simulation. To compare the results with experimental data and to parametrize the simulation, we use EBSD measurements, which have been produced by Simone Schendel[ii].

Figure 1 gives an overview about the dataflow and the role of the EBSD data. The vertical arrows describe data flow or a simulation step. Data are transferred from the finite element method to the phase field method. The thin arrows illustrate the validation steps with experimental measurements. The EBSD images show a fine and noisy grainstructure directly after cold

rolling in contrast to the coarse grains and detailed picture after annealing.
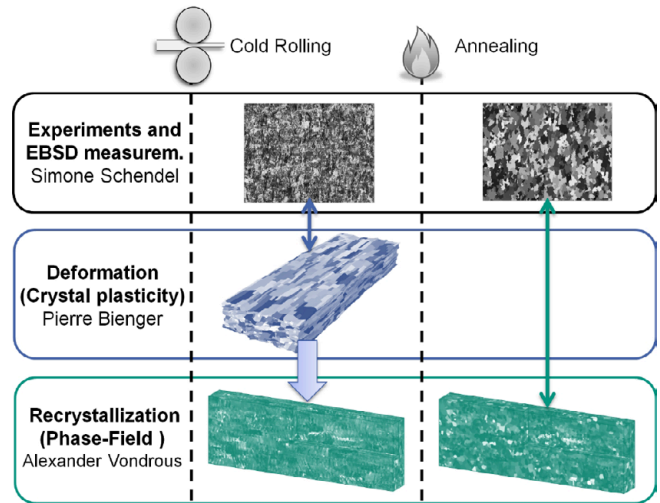
Figure 1: Virtual process chain with EBSD data validation.

2. Method

To simulate recrystallization, we divide the processes into two parts. First the nucleation of recrystallizing grains and second the growth of those grains. Before we model recrystallization, we have to consider interfaces to the prior and following process steps, because we are part of the virtual process chain.

2.1. Data Conversion

The starting condition for the phase-field simulation of the recrystallization process is generated from the finite element deformation simulation. Integration points inside the elements contain information about the crystal orientations and the cumulative shear. A text file is used to transfer the data. Each line of the file contains the position, orientation, and cumulative shear of a single integration point.

To map the irregular finite element integration points to the regular finite difference grid, we make a voronoi construction with the integration points like Raabe in [8]. A drawback is the missing finite element mesh to restrict the voronoi construction. We cope this by cutting the domain, such that no artifacts of the voronoi construction remain. We remove the periodic property of the finite element simulation with this approach. To not lose information about the orientations, we assign each integration point to a phase-field phase and cluster the regular grid depending on the orientation with the algorithm from [9] and a 1° misorientation angle threshold. Now nearly each integration point is occupied by a seperate grain.
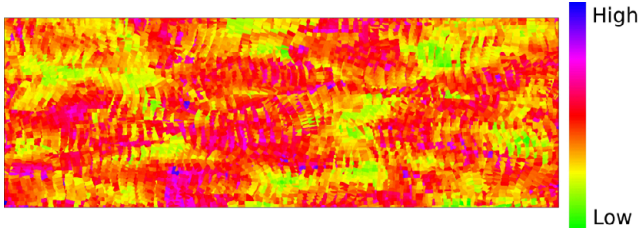
Figure 2: Converted cumulative shear distribution of a 2D cut from the 3D domain.

2.2. Nuclei detection

Nucleation of recrystrallizing grains is still not completely understood [1,3] and often involves to change a simulation model. To find nuclei without an explicit nucleation model, we assume, that nuclei and their orientation are preexisting in the deformed domain and that subgrains with a high amount of cumulative shear are preferred nuclei. Cumulative shear is the sum of the plastic shear over all slip systems and serves as a measure for the stored energy. Figure 2 shows a 2D cut from a 3D domain. Areas with a higher nucleation probability are colored in blue. The higher the cumulative shear, the higher the amount of stored energy. Figure 3 shows the cumulative shear of each subgrain and a nucleation threshold at 4.0.
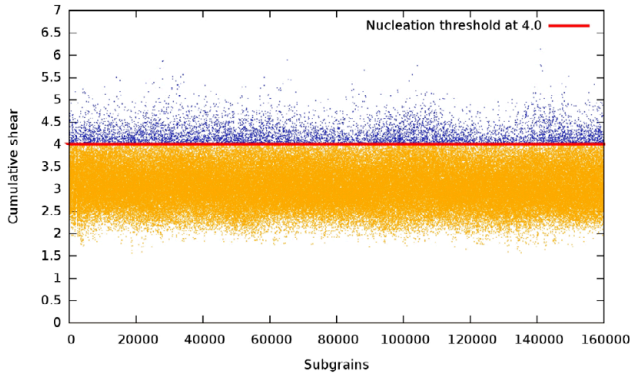
Figure 3: Cumulative shear of each subgrain with a nucleation threshold at 4.0. The blue dots refer to subgrains which select nuclei.

To estimate the nucleation threshold, we create pole figures from the grains above the nucleation threshold (recrystallizing grains) and compare them with the pole figure of the EBSD measurement. The pole figures of the threshold with most agreement to the measured pole figure is used for the simulation.

2.3. Phase-Field Modelling

The multi-phase-field model of Garcke, Nestler and Stinner in [9] is the basis for our nuclei growth description. The phase-field vector $\phi_\alpha = (\phi_1, ..., \phi_N)$

represents with its components ϕ_α grains with orientation α.

Cumulative shear is an external variable and described with Γ. We add the energy density $f(x, \phi; \Gamma)$ to the energy density functional and obtain:

$$\mathcal{F}(\phi; \Gamma) = \int_\Omega \varepsilon a(\phi, \nabla\phi) + \frac{1}{\varepsilon} w(\phi) + f(x, \phi; \Gamma) dx ,$$

where $f(x, \phi; \Gamma)$ can be written as

$$f(x, \phi; \Gamma) = \Gamma(x) \sum_\alpha^N g_\alpha h(\phi_\alpha)$$

The scaling parameter g_α controls the strength of the driving force for grain α. We use the scaling factor to remove the driving force for non recrystallizing grains, such that only recrystallizing grains obtain the stored energy driving force.

For a more sophisticated representation of grain growth, we use the Read Shockley formulation [10] to model the dependence of the surface energy on the misorientation between grains by:

$$\gamma_{\alpha\beta} = \gamma_m \frac{\Theta_{\alpha\beta}}{\Theta_m} \left(1 - \log \frac{\Theta_{\alpha\beta}}{\Theta_m} \right)$$

Here $\gamma_{\alpha\beta}$ describes the surface energy between grain α and β depending on the misorientation angle $\Theta_{\alpha\beta}$ between them. The parameter Θ_m is set to 15° and γ_m chosen to be 1. The mobility $\tau_{\alpha\beta}$ between grains is assumed to be low a small angle grain boundaries and high at large angle grain boundaries:

$$\tau_{\alpha\beta} = 0.9 \frac{1}{1 + e^{-2(\Theta_{\alpha\beta} - 15)}} + 1$$

To create a 3D simulation domain with a sufficient resolution, we generate 641^3 cells. The other phase field parameters are set to establish stable simulation conditions.

3. Results

Data from the irregular finite element mesh to the regular finite difference grid are successfully converted applying a voronoi construction. The phase-field model is extended to describe a driving force, which can explicitly act on selected phases/grains.

Pole figures are used to compare the simulation results with experimental data. It is not possible to reproduce the maximum values of the pole figures, because the number of measurement points differs for each simulation method and for the EBSD measurement.

But the position of the maxima and the shape of the texture must be reproduced to simulate the recrystallization process in a qualitative manner.
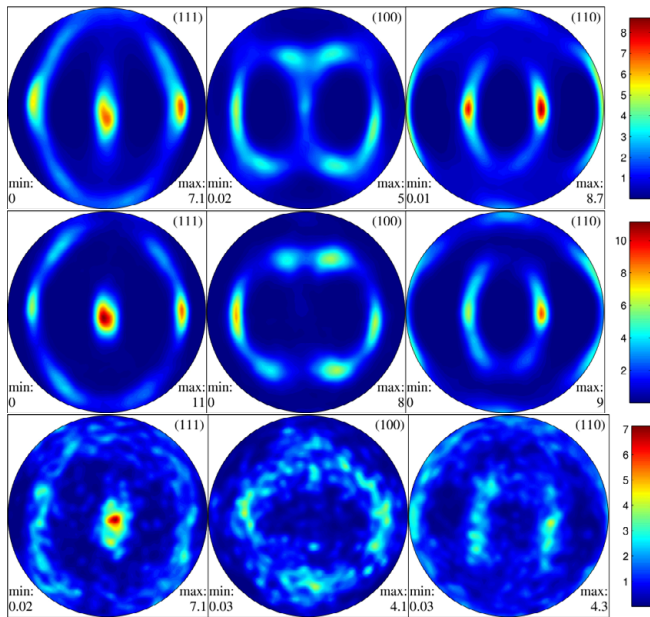
Figure 4: Pole figures obtained at different steps of the phase-field simulation and from EBSD measurements after annealing. Top: Simulated pattern after finite element deformation. Middle: After recrystallization. Bottom: EBSD measurement after annealing for comparison.

The development of the texture from the beginning of the recrystallization simulation to a completely recrystallized microstructure is shown at the top and middle pole figures in Figure 4. A weakening of the deformation texture during recrystallization is visible in (100) direction, whereas an accumulation in (111) direction can be seen which is typical for the DC04 steel.

4. Outlook

Data conversion establishes a link between macroscopic finite element and mesoscopic phase-field simulations of grain structure evolution, which allows to incorporate for multi scale investigations. The "nucleation process" can be generalized in order to account for a temperature or time dependent nucleation threshold. An interface for data transfer from the regular difference grid to the finite element mesh has to be established to provide access to a simulation environment capable to measure mechanical properties of the recrystallized micro-structure.

5. References

[1] Doherty, R.D., Hughes, D.A., Humphreys, et al. 1997, Current issues in recrystallization: a review, Materials Science and Engineering A238: 219 – 274

[2] Gottstein, G, 2007, Physikalische Grundlagen der Materialkunde, Springer, 3. Edition: 303-355

[3] Rios, P.R. , Siciliano Jr, F, Sandimc, H.R.Z., Plaut, R.L., Padilha, A.F., 2005, Nucleation and Growth During Recrystallization, Materials Research, Vol. 8, No. 3: 225-238

[4] Kolmogorov, A.N., 1937, Izv. Akad. Nauk. USSR-Ser-Matemat. 1(3), 355

[5] Langer, J. S., Instabilities and pattern forestation in crystal growth, Rev. Mod. Phys. Vol. 52 Issue 1: 1-28

[6] Muramatsu, M., Tadano, Y., Shizawa, K., 2008, A Phase-Field Simulation of Nucleation from Subgrain and Grain Growth in Static Recrystallization, Materials Science Forum , Volumes 584 – 586: 1045-1050

[7] Takaki, T., Tomita, Y., 2010, Static recrystallization simulations starting from predicted deformation microstructure by coupling multi-phase-field method and finite element method based on crystal plasticity, International Journal of Mechanical Sciences, Volume 52, Issue 2: 320-328

[8] Raabe, D., Becker, R., 2000, Coupling of a crystal plasticity finite-element model with a probabilistic cellular automaton for simulating primary static recrystallization in aluminium, Modelling Simul. Mater. Sci. Eng., 8 (2000): 445–462

[9] H. Garcke, B. Nestler, B. Stinner, A diffuse interface model for alloys with multiple components and phases, SIAM J. Appl. Math. 64: 775-799

[10] Read, W. T., Shockley, W., 1950, Dislocation Models for Crystal Grain Boundaries, Physical Review Vol. 78 Nr. 3: 275-289

[i] Pierre Bienger, Fraunhofer Institute for Mechanics of Materials IWM in Freiburg - Germany
[ii] Simone Schendel, IAM-WBK at the KIT in Karlsruhe - Germany

Graduate School 1483
Process Chains in Production:
Interaction, Modelling and Assessment of Process Zones
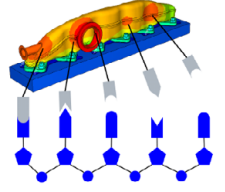
Investigation and modelling of the material behaviour of DC04 steel

M. Baiker[1,2], D. Helm[1]

[1] Fraunhofer Institute for Mechanics of Materials IWM
[2] Institute of Applied Materials - Reliability of Systems and Components IAM-ZBS, KIT

The ferritic steel DC04 is a common material for sheet metal forming processes. The simulation of such forming processes requires the constitutive modelling of the material behaviour like the yield locus and the hardening behaviour in the context of finite deformations and for complex loading paths. In this work, the model includes an anisotropic yield surface as well as isotropic and kinematic hardening. In order to define an appropriate yield function, additional simulations in the framework of crystal plasticity has been performed to calculate yield point for different load cases and thereby predict the shape of the yield surface. On the basis of these results, the plastic anisotropy is represented by means of a Hill-type yield function. The parameters for the macroscopic description of anisotropy are calibrated using the Lankford coefficients and the results from the crystal plasticity calculations. With the calibrated model tension tests in seven directions are simulated and compared to experimental results in order to identify the capability and limitation of this model for representing DC04.

DC04, Anisotropy, Hill'48 yield function.

1. Introduction

The simulation of complex forming processes requires material models and appropriate numerical algorithm that combine good predictions of the material behaviour with optimal performance and robustness. Therefore, the simulations are typically based on phenomenological models as proposed by Chaboche and Rousellier [1], Barlat and Lian [2], Banabic et al. [3]. In the industrial environment, a common approach to model the anisotropy of sheet metals is to use a Hill-type yield function [5]. We will investigate if it is possible to model the anisotropic behaviour of DC04 steel with this approach properly. For that purpose several points on the initial yield surface are calculated using a crystal plasticity model. The determined shape of the yield surface is compared to the shape of the Hill-type yield surface calibrated to the Lankford coefficients in rolling direction, 45° and 90° to rolling direction. Additionally, the experimentally measured stress strain data and Lankford coefficients evaluated at 0.18% plastic strain for tension tests in seven directions are compared to simulation results.

2. Material Modelling

In this work, the material behaviour in complex forming processes is represented by using a macroscopic finite plasticity theory. However, in order to assist the modelling and parameter identification, a polycrystalline unit cell model based on crystal plasticity is used, too.

2.1. Macroscopic Finite Plasticity Model

To model the material behaviour in complex forming processes properly (cf. [4]), isotropic and kinematic hardening concepts as well as plastic anisotropy have to be taken into account. The considered model is based on the additive decomposition of the strain rate tensor.

$$\mathbf{D} = \mathbf{D}_e + \mathbf{D}_p, \tag{1}$$

into an elastic part $\mathbf{D}_e$ and a plastic part $\mathbf{D}_p$. The stress state is modelled by means of a hypoelasticity relation,

$$\overset{\circ}{\mathbf{S}} = 2\mu \left[\mathbf{D}^D - \mathbf{D}_p\right] + \kappa \left[\text{tr } \mathbf{D}\right] \mathbf{1}. \tag{2}$$

Therein $\overset{\circ}{\mathbf{S}}$ is an appropriate objective time derivative of the Kirchhoff stress $\mathbf{S}$. The shear and compression modulus are denoted by μ and κ.

A Hill-type yield function is introduced for describing the anisotropic plastic yielding

$$f = \sigma_H - \left[k_0 + R(s_p) \right]. \tag{3}$$

The scalar valued equivalent stress

$$\sigma_H = \sqrt{(\mathbf{S}^D - \mathbf{X}) \cdot \overset{4}{\mathbf{H}}(\mathbf{S}^D - \mathbf{X})} \tag{4}$$

is represented with the fourth order Hill tensor. In the yield function (3), k_0 is the initial yield radius and $R(s_p)$ models the isotropic hardening (cf. Helm [6])

$$R(s_p) = \sum_{i=1}^{N_R} R_i(s_p) = \sum_{i=1}^{N_R} \frac{\gamma_i}{\beta_i} \left[1 - \exp[- \beta_i s_p] \right] \tag{5}$$

with the material parameters γ_i and β_i and the accumulated plastic strain s_p as defined in equation (9). The kinematic hardening is modelled by the backstress tensor $\mathbf{X}$ as suggested by Chaboche and Rousselier [1]: The kinematic hardening $\mathbf{X}$,

$$\mathbf{X} = \sum_{j=1}^{N_X} \mathbf{X}_j , \tag{6}$$

is the sum of N_X Armstrong-Frederick terms

$$\overset{\circ}{\mathbf{X}}_j = c_j \mathbf{D}_p - b_j \dot{s}_p \mathbf{X}_j , \tag{7}$$

which are introduced in analogy to the small strain kinematic hardening model of Armstrong and Frederick [7]. Therein, c_j and b_j are the material parameters. Finally the plastic flow results from the normality rule

$$\mathbf{D}_p = \lambda \frac{\partial f}{\partial \mathbf{S}} . \tag{8}$$

The plastic multiplier λ is calculated from the consistency condition $df = 0$. Finally, the accumulated plastic strain s_p is defined by the differential equation

$$\dot{s}_p = \sqrt{\frac{2}{3}} \lambda . \tag{9}$$

The material model is implemented with an efficient integration scheme in a material user subroutine Umat for ABAQUS. To determine the parameters of the material model, tension test in rolling direction, tension-compression test, and the Lankford coefficients for tension in rolling direction (RD), transverse direction (TD) and in 45° to rolling direction are required (cf. chapter 3).

2.2. Single Crystal Plasticity Model

From experimental point of view, it is very difficult to determine material properties of sheet metals like the yield surface or the hardening behaviour at large strains. Therefore, additional simulations based on a polycrystal unit cell model are performed using a single crystal plasticity material model [8]. In that so called "Virtual laboratory" [9] the shape of the initial yield surface and the Lankford coefficient are calculated.

The investigated ferritic steel DC04 consists of a body centred cubic (bcc) crystal structure. In this crystal structure, three slip families exist. For the simulations presented in this work, the first two slip families with 12 slip systems are considered. The parameters of the single crystal plasticity model are calibrated using tensile tests in rolling and transverse direction.

In the considered unit cell model, the polycrystalline microstructure consists of 1000 grains and 30^3 elements. For the heat treated material, the grains are nearly globular, which is considered by generating the virtual grain morphology by Voronoi tessellation. The initial unit cell model is pictured in Figure 1. The texture was measured at the Institute for Applied Materials (IAM-WBM) in Karlsruhe in Project A6. The orientation of 2542 singles grains has been detected using Electron Backscatter Diffraction (EBSD). For the simulation, the texture information is reduced to the 1000 grains. The different orientations are marked by the different colours.
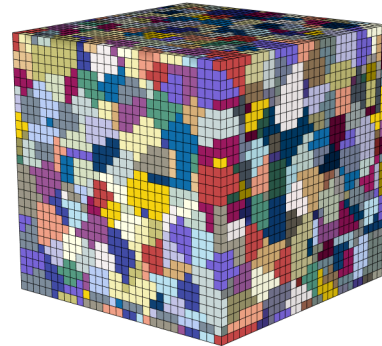
Figure 1: Initial unit cell model with periodic boundary conditions

The pole figures of the EBSD Data and after the reduction to 1000 grains are compared in Figure 2. Small differences can be observed therefore more than

1000 grains seem to be required for a better representation of the texture.

a) Polefigure from EBSD data (2541 grains)

b) Polefigure from reduced data (1000 grains)
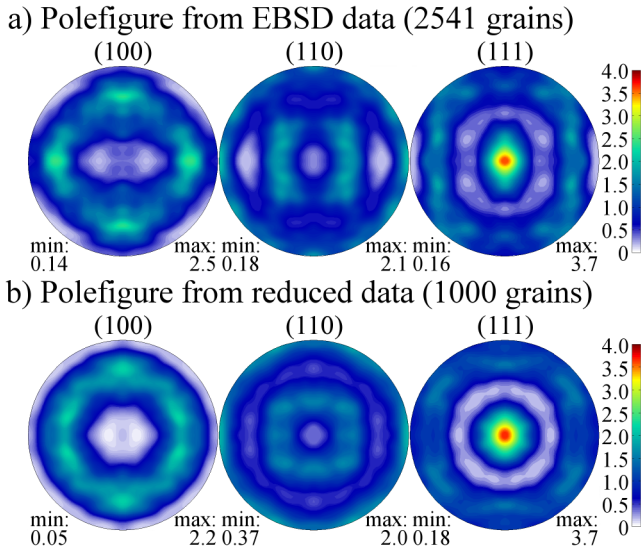
Figure 2: Pole figure of the initial microstructure

3. Results

To present the capabilities and the limitations of the macroscopic model, the initial yield surface from the virtual laboratory will be compared to the shape of the Hill yield surface calibrated by different methods. For the validation, the stress strain curves for tension tests in seven directions and the Lankford coefficients are calculated and compared to experimental results.

3.1. Shape of the Initial Yield Surface

With the calibrated crystal plasticity model several load cases are simulated and the offset yield points at 0.2% strain are determined. In Figure 2 these points are marked with green triangles. The shape of the Hill-type yield surface fitted to the Lankford coefficients and fitted to the results of the "Virtual Laboratory" (i.e. the offset yield points at 0.2%) are plotted in dark blue and light blue. The different sets of Hill parameters are listed in Table 1.

Table 1: Material parameter for Hill-type yield function of finite plasticity model

Calibrated using:	F	G	H	L	M	N
Lankford Co-efficients	0.30	0.35	0.65	1.5	1.5	1.13
"Virtual La-boratory"	0.40	0.42	0.58	1.5	1.5	1.24

Figure 2 shows that it is possible to calibrate the Hill parameters in a way to fit the results of the "Virtual

Laboratory". However the shape of the yield surface is different when we use one common approach to calibrate the Hill parameters to the Lankford coefficients. The two experimental data points for the tension test in rolling and transverse direction are in good agreement for both methods
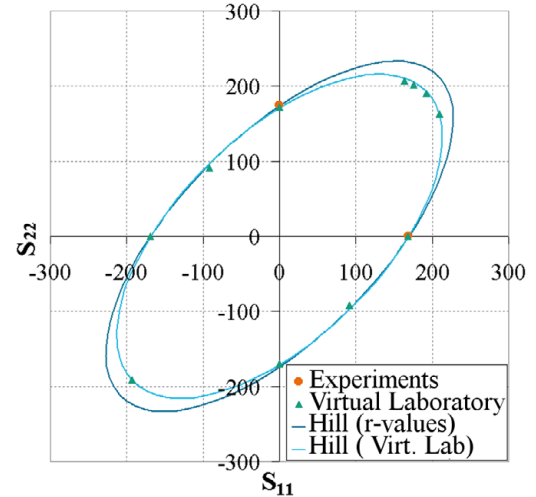
Figure 3: Shape of the initial yield surface

3.2. Tension Tests in Seven Directions

For further investigation on the capability of the description of anisotropy, tension tests in seven directions are simulated with the calibrated model. The results are compared to experiments performed at the IUL in Dortmund. In Figure 3 the stress strain data for the different directions are shown. Due to large amount of data and to improve the perceptibility, the experimental and simulation results are plotted in two separate diagrams. The experimental results can be found in Figure 3 and the results of the simulation with the Hill'48 yield function calibrated to the yield surface determined in the "Virtual Laboratory" are pictured in Figure 4. It can be observed that the stresses predicted by the Hill'48 yield function are slightly too high compared to the experimental results. The results of the simulations calibrated to the Lankford coefficients are spared in the diagram to avoid confusion. But they overestimate the stresses considerably. Besides the Hill'48 parameters all other model parameters are the same for both simulations.

3.3. Lankford Coefficients

During the experiments the changes in length and width have been measured with an extensometer. Based on the assumption of constant volume the evolution of the thickness is calculated. With this information the Lankford coefficients are determined. As the Lankford coefficients develop during the experiment the value at 0.18 Percent plastic strain is used for

the comparison. Figure 5 shows the Lankford coefficients determined in the experiment and in the simulations.
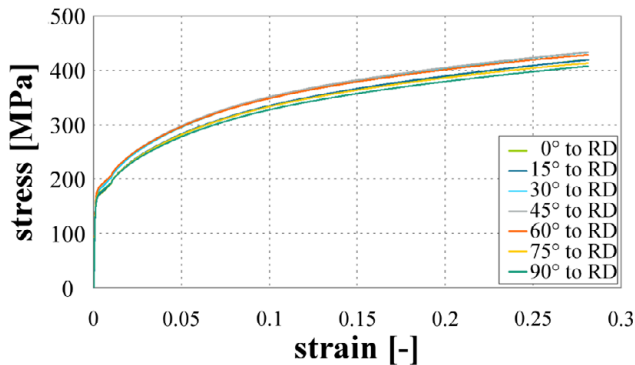
Figure 4: Experimental results of tension tests
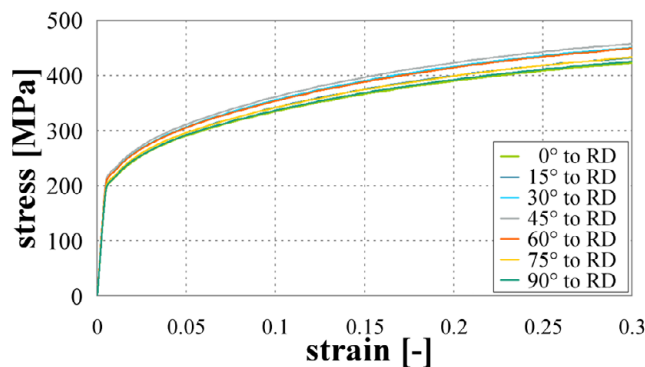
Figure 5: Simulation of tension tests: Hill'48 calibrated to the "Virtual Laboratory"
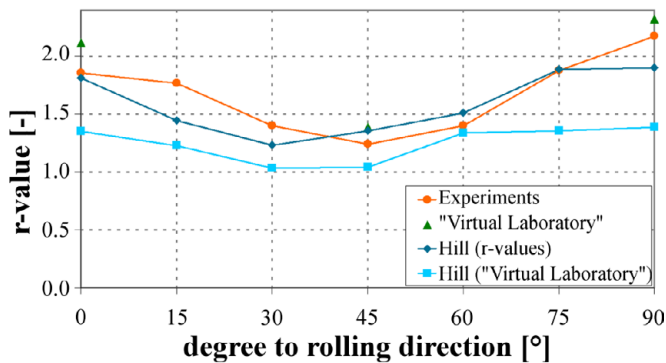
Figure 6: Lankford Coefficients

The Lankford coefficients determined in the "Virtual Laboratory" are higher than the experimental results but the right proportions can be observed between 0°, 45°, and 90°. The Hill-type yield function calibrated to the Lankford coefficients in three directions describes the experimentally determined material behaviour in the intermediate range of angles to rolling directions very well. The Hill-type yield function calibrated to the results of the "Virtual Laboratory" naturally show less developed anisotropy of the Lankford Coefficients.

The results show that the Hill-type yield function is able to represent the yield behaviour of the material. Depending on whether the model is calibrated using the r-Values or the results of the "Virtual Laboratory" the model can describe the Lankford Coefficients or the stress strain data with higher accuracy. Therefore, the way how to calibrate the Parameters should be chosen thoughtfully with regard to the application.

4. References

[1] Chaboche, J.L., Rousselier, G., 1983. On the plastic and viscoplastic constitutive equations – Part I. Rules developed with internal variable concept, J. Press. Vess. Technol. ASME, 105, p. 153-158.

[2] Barlat, F., Lian, J., 1989. Plastic behavior and stretchability of sheet metals. Part I: A yield function for orthotropic sheets under plane stress conditions, International Journal of Plasticity 5, p. 51-66.

[3] Banabic, D., Balan, T., Cosma, D.S., 2000. A new yield criterion for orthotropic sheet metals under plane-stress conditions. In: Proc. 7th Cold Metal Forming Conference, Cluj Napoca, Romania, p. 217-224.

[4] Krasovskyy, A., Schmitt, W., Riedel, H., 2006. Material Characterisation for Reliable and Efficient Springback Prediction in Sheet Metal Forming, Steel Research Int. 77, No. 9-10, p. 747- 753.

[5] Hill, R., 1948. A Theory of the Yielding and Plastic Flow of Anisotropic Metals, Proceedings of the Royal Society of London, 193A, p. 281.

[6] Helm, D., 2010. Thermomechanical representation of the stored energy during plastic deformation, International Journal of Material Research. Vol. 101, No.8, p. 972-980.

[7] Armstrong, P.J., Frederick, C.O., 1966. A mathematical representation of the multiaxial Bauschinger effect, Report RD/B/N731, CEGB, Central Electricity Generating Board, Berkeley, UK.

[8] Huang, Y.G., 1991. A User-material Subroutine Incorporating Single Crystal Plasticity in the ABAQUS Finite Element Program, Mech. Report 178, Harvard University, Cambridge, Massachusetts.

[9] Helm, D., Butz, A., Raabe, D., Gumbsch, P., 2011. Microstructure-Based Description of the Deformation of Metals: Theory and Application, JOM, Volume 63, Issue 4, p. 26-33

Graduate School 1483
Process Chains in Production:
Interaction, Modelling and Assessment of Process Zones
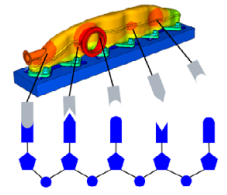
Process Observation and Control:
Identifying functional dependencies between input, hidden state and output

M. Senn, N. Link

Institute of Applied Research (IAF), Karlsruhe University of Applied Sciences

The consideration of process chains in production allows the monitoring of workpieces from pre-products to their final forms. The process state thereby serves as a characterization of the workpiece for each point in time. The holistic modeling enables the optimization of the process chain with respect to final workpiece properties and their associated efforts. Therefore, fast and robust state prediction and control models that describe the functional dependencies between parameters, associated observable quantities, the hidden state and corresponding workpiece properties are needed. The state which is not accessible during process execution is revealed by regression methods based on related observable quantities. Dimension reduction methods reduce the complexity in the high-dimensional regression quantities. The resulting compact feature space can then serve as a basis for process control by meaningful characteristics. The objective in process control is to find the optimal temporal evolution of the parameters with respect to an objective function despite of disturbances occurring during process execution. The optimization problem can be formulated by Dynamic Programming in terms of overlapping sub problems of the evolving system dynamics. However, Dynamic Programming approaches might suffer from the curse of dimesionality in process control which can be overcome by Approximate Dynamic Programming.

Regression, Dimension Reduction, Dynamic Programming.

1. Introduction

The Research Training Group 1483 deals with the characterization and modelling of individual processes as well as their linkage to entire process chains. This allows a holistic consideration of process chains including interactions between the processes which can be compensated by a process chain optimization. The objective is to find optimal parameters for each single process with respect to the final workpiece properties and associated efforts of the adjusted parameters. Therefore, fast models which only describe the characteristic behavior are needed for the observation and control of individual processes.
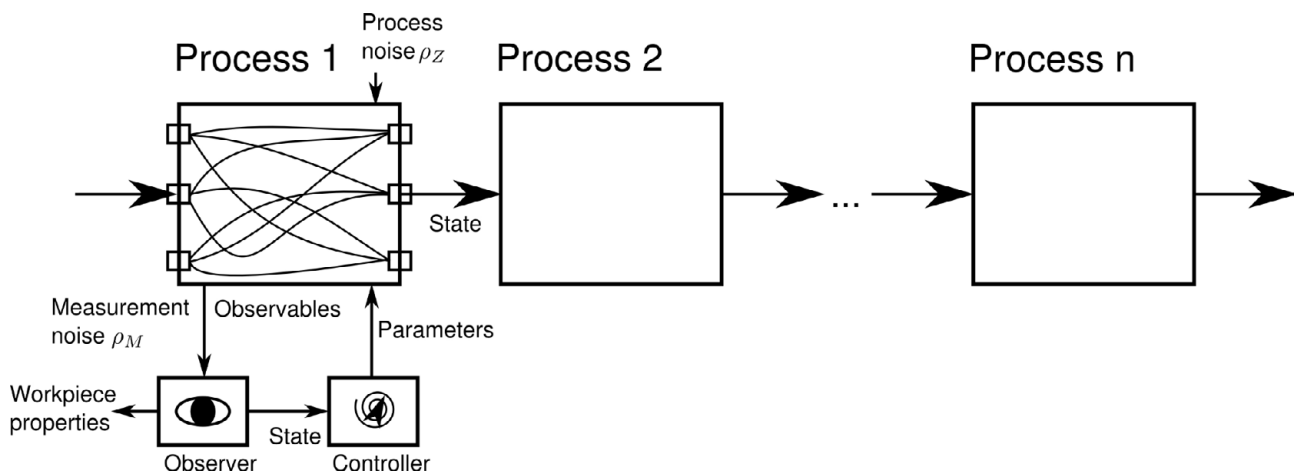
Figure 1: Functional dependencies between parameters, observables, state and workpiece properties.

The generic model depicted in Figure 1 describes the linkage of the individual processes by the state which provides a unique characterization of the workpiece within the process chain. Furthermore, the generic model allows the identification of functional dependencies between parameters, observable quantities, the hidden process state and the corresponding workpiece properties. This generic description of an individual process enables the application to different processes by an adequate selection of the quantities and corresponding data.

2. Process Observation

In process observation, the hidden process state that cannot be measured with reasonable effort during execution is determined from more easily, so-called observable quantities. Statistical process observers are capable of indentifying this relation by regression analysis with data from simulations or experiments. High-dimensional and correlated quantities can previously be reduced to subspaces of meaningful characteristics.

2.1. Statistical Process Observers

A statistical process observer for a deep drawing process has been realized by using an Artifical Neural Network (ANN) with three layers for non-linear regression [1]. During the training of the ANN by given input and output data, the connection weights between the single layers (input, hidden, output) are determined by minimizing the deviation of the predicted output from the target quantity. To reduce the complexity in the regression relation between a history of observable quantities and the current process state, Principal Component Analysis (PCA) is applied to both input and output. PCA allows to reduce the complexity by projecting on a new basis with dimensions of high variance and neglecting dimensions of low variance. The explained variance then corresponds to the characteristic features of the high-dimensional data. A statistical model for the observation of a resistance spot welding process has been created by Partial Least Squares (PLS) Regression [2]. The linear regression analysis contains a dimension reduction in the input and the output under consideration of maximizing the covariance between these quantities. Here, the dimension reduction in the input is performed with respect to the regression relation and the resulting influence on the output quantity. Both methods described so far for reducing the complexity assume linear sub-spaces for the presentation of the data. This might be inefficient or inadequate for the model of the process data under consideration. In this case, a non-linear regression

with integrated non-linear dimension reduction is seeked for.

2.1.1. Principal Function Approximators

The objective of Principal Function Approximators (PFAs) is to realize a results-oriented dimension reduction in the regression of high-dimensional data. This avoids that characteristics of the input which have a crucial influence on the output are removed by variance-based dimension reduction methods such as PCA. PFAs are based on Bottleneck Neural Networks [3] and allow to predict a target quantity in its high-dimensional space at the output layer and to extract features at the bottleneck layer. The bottleneck is the smallest layer and represents the essential characteristics of the regression relation with respect to input and output.
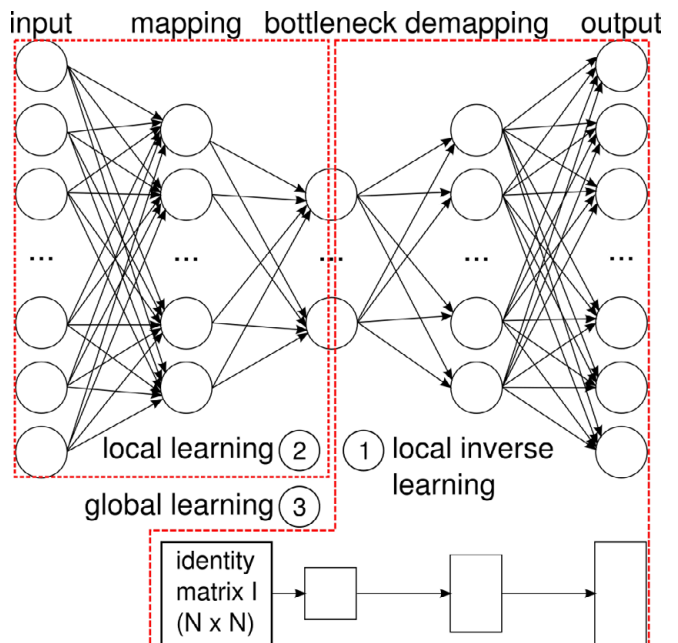
Figure 2: Training of a Principal Function Approximator.

The training of a PFA is illustrated in Figure 2. First, the global network is divided into two local parts which are trained separately. The back part (demapping) is identified by an inverse learning procedure [4]. Here, not only the connection weights are to be determined, but also the bottleneck components which serve as input for the back part. Therefore, an additional layer is added to the back part which is fed by the identity matrix as a training pattern. The adjusted weights between the additional layer and the bottleneck layer correspond to the bottleneck components. These are then used to train the front part of the PFA (mapping). The weights learned by local training of the two subnets are used as an initialization for the global adaption phase in which the weights are again

adjusted with respect to the global network by given input and output. This enables to improve the solution for the approximation compared to ordinary ANNs trained by gradient descent methods which are prone to get stuck in local optima.

3. Process Control

The main concern of classical control is to follow a given reference trajectory to obtain a desired final result due to disturbances which occur during process execution. However, the achievement of these predefined quantities in the controlled variable is associated with a corresponding production effort that depends on the process parameters. Therefore, we define a flexible cost function for the optimization of an individual process with respect to a given final reference quantity and the associated production effort as illustrated in Figure 3. In an industrial application, the user can define the tradeoff between a reference quality and the associated production effort. An example for a flexible optimization of a sample process chain is given in [5]. This optimization goal is addressed by Bellman's Principle of Optimality and Dynamic Programming (DP).
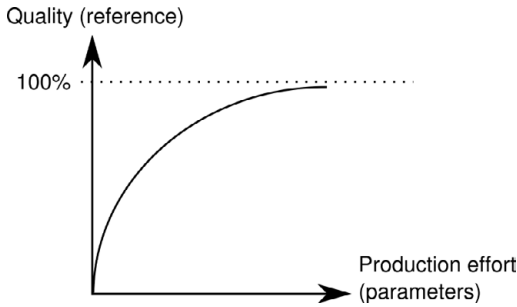
Figure 3: Tradeoff between reference quality and production effort in flexible optimization.

3.1. Dynamic Programming

The process dynamics can be described by state transitions f_k from initial states x_{k-1} to final states x_k based on the selected parameters u_k and the occurring unknown disturbances w_k:

$$x_k = f_k(x_{k-1}, u_k, w_k). \qquad (1)$$

Each state transition generates transformation costs which depend on the process parameters. The summation of all local transformation costs results in the total costs which are to be optimized. In DP, the overall optimization problem can be divided into smaller sub problems. One sub problem only consists of the optimization of the local transformation costs and the resulting successor costs as described by the Bellman Equation [6]. The connection of the sub problems can

be realized by lookup tables to find the overall solution recursively.

The costs $J_k(x_{k-1})$ for a deterministic sub problem at time step k depend on a unique state transition by a given initial state x_{k-1} and selected parameters u_k as indicated by Figure 4 (top):

$$J_k(x_{k-1}) = \min_{u_k}\{g_k(x_{k-1}, u_k) + J_{k+1}(x_k)\}, \qquad (2)$$

where g_k stands for the local transformation costs and J_{k+1} describes the successor costs which depend on the final state x_k of the current time step k.

If stochastic influences by means of unknown disturbances w_k are taken into account, there are multiple state transitions from one initial state with selected parameters u_k as shown in Figure 4 (bottom). The costs $J_k(x_{k-1})$ for a stochastic sub problem as a Markov Decision Process at time step k are described in terms of an expectation:

$$\langle J_k(x_{k-1})\rangle = \min_{u_k}\{g_k(x_{k-1}, u_k) + \langle J_{k+1}(x_k)\rangle\},$$

$$\langle J_{k+1}(x_k)\rangle = \sum_{l=1}^{L} P(x_k^l \mid x_{k-1}, u_k) \cdot J_{k+1}(x_k^l),$$

$$\sum_{l=1}^{L} P(x_k^l \mid x_{k-1}, u_k) = 1. \qquad (3)$$

The disturbances w_k are associated with a probability for each possible state transition $P(x_k^l \mid x_{k-1}, u_k)$.
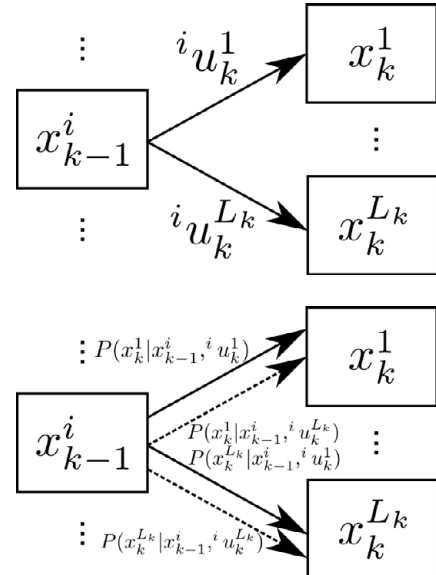
Figure 4: State transitions: deterministic (top) and stochastic (bottom) [5].

At the end of the process, the final state x_N has to be evaluated by defining the costs J_{N+1} with respect to a given quality reference in terms of the function h:

$$J_{N+1}(x_N) = h(x_N) \, . \tag{4}$$

The drawbacks of DP involve large lookup tables resulting from discretized state and parameter spaces and multiple state transitions due to disturbances. This can be overcome by replacing the lookup tables by learning structures of continous approximations of cost functions in Approximate DP (ADP).

3.2. Approximate Dynamic Programming

In ADP [7], the cost functions are created as continous approximations of given data relations by means of samples from simulations or experiments. The approximations can be obtained by regression methods such as ANNs, where the term Neuro-DP (NDP) [8] comes from in this context. By these approximations, the curses of dimensionality that occur in DP can be overcome. It has been shown that ADP can be successfully used in process control [9].

3.3. Flexible ADP Control

We propose an ADP approach for process control by offline learning of the cost function. Deterministic data are given by Finite Element simulations which are modified by inducing stationary disturbances from a given probability distribution. Functions for the final costs and the parameter costs are defined and determined for all states and resulting transitions. In an offline phase, the approximations for the cost functions and the state transitions are learned by ANNs for each time step recursively backwards in time. In an online phase, the found approximations can be used to solve the optimization problem on given validation data that have not been used in the offline training phase.

4. Conclusion

We have proposed different statistical observer models for extracting the characteristic behavior and for predicting the hidden process state. These models have been applied to real production processes by means of data from simulations or experiments.

Ongoing work is concerned with the application of the flexible ADP control approach to deep drawing simulations for selected state variables. Then in a next step, the introduced methodology for observation and control will be combined to enable a feature-based control. Therefore, the features extracted by the PFAs in process observation have to be investigated for their suitability in process control. It has to be assured that the quantities of the generic model are selected with respect to observability and controlability of the process. To identify successfully the functional dependencies between parameters, observables, state variables and material properties, there must exist correlations in the data. Finally, more applications are intended, especially on experimental data including disturbances.

5. References

[1] Senn, M.; Link N., 2010, Hidden State Observation for Adaptive Process Controls, Proceedings of the 2nd International Conference on Adaptive and Self-adaptive Systems and Applications:52-57.

[2] Senn, M.; Link N., 2010, Revealing Effects of Dynamic Characteristics in Process Monitoring and Their Influences on Quality Prediction, Proceedings of the 8th International Conference of Numerical Analysis and Applied Mathematics.

[3] Parviainen, E., 2010, Dimension Reduction for Regression with Bottleneck Neural Networks, Proceedings of the 11th International Conference on Intelligent Data Engineering and Automated Learning 6283.

[4] Scholz, M., Fraunholz, M., Selbig, J., 2007, Nonlinear Principal Component Analysis: Neural Network Models and Applications, Lecture Notes in Computational Science and Engineering 58:44-67.

[5] Senn, M.; Schäfer, J.;Pollak, J.; Link, N., 2011, A System-Oriented Approach for the Optimal Control of Process Chains under Stochastic Influences, Proceedings of the 9th International Conference of Numerical Analysis and Applied Mathematics.

[6] Bertsekas, D. P., 2005 / 2007, Dynamic Programming and Optimal Control.

[7] Powell, W. B., 2007, Approximate Dynamic Programming.

[8] Bertsekas, D. P.; Tsitsiklis J., 1996, Neuro-Dynamic Programming

[9] Lee, J. H.; Wong, W., 2010, Approximate dynamic programming approach for process control, Journal of Process Control, 20/9:1038-1048.

Graduate School 1483
Process Chains in Production:
Interaction, Modelling and Assessment of Process Zones
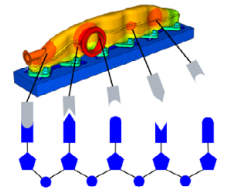
Microstructural investigation and micromechanical behavior of deep drawing steel DC04

Simone Schendel, Reiner Mönig, Oliver Kraft

Institute for Applied Materials, KIT - Karlsruhe Institute of Technology

The production process of DC04 steel sheet metals is composed of several steps including hot rolling, cold rolling, a heat treatment and a final deep drawing step. When DC04 steel runs through this process chain, its microstructure and mechanical behavior are severly altered. In this work the cross sectional microstructure of the heat treated and cold rolled DC04 steel was investigated. The cross sections were prepared by FIB and EBSD and EDX measurement were performed on selected locations to investigate the microstructure and chemical composition of precipitates that were found in the DC04 steel matrix. The micromechanical behavior of the heat treated and cold rolled DC04 steel was investigated by microcompression experiments on single crystalline and polycrystalline pillars with diameters between 2 µm and 22 µm. In the heat treated material, pillars with diameter larger than 4 µm reach the bulk strength that was determined by macrocscopic tensile experiments. I

Microcompression, size effect, heat treated DC04 steel

1. Introduction

Within the Graduate School 1483, research area A focuses on the process chain during sheet metal manufacturing. This process chain is composed of different process steps such as hot rolling, cold rolling, heat treatment and a final deep drawing procedure. The aim of this research area is to describe the material response during and after these process steps with material models that are developed in individual projects. To optimize and verify these material models, experimental investigations and data are necessary. This project focuses on the characterization of the microstructure and the mechanical properties after the individual process steps.

1.1. Material

Investigations were performed on a non-alloyed DC04 steel which is a standard deep drawing steel used for example in the automotive industry [01]. The material consists of a ferrite crystal structure that besides α-Fe contains 0.4 wt.-% manganese and 0.08 wt.-% of carbon [02]. The DC04 steel was produced by Voestalpin AG (Linz, Austria) and all steel samples originate from the same batch and were extracted directly from the manufacturing process either after a cold rolling or after a subsequent heat treatment step.

Cold rolling and heat treatment procedures have a singnificant influence on the microstructure and the mechanical properties of the DC04 steel. In this work the microstructure of the cold rolled and heat treated material was investigated by EBSD and EDX. The deformation behavior on the micrometer scale was investigates with micro compression experiments [03] on cylindrical pillars and the results afterwards compared with macroscopic tensile experiments. The microcompression data on the heat treated material were used in topic A2 to develop a micromechanical model that describes the material response during deep drawing processes.

2. Experimental

2.1. Surface preparation

For EBSD measurements, smooth sample surfaces were needed. In order to achieve surfaces with good quality, the specimens were first ground with SiC paper of decreasing grain size and then polished with diamond pastes with decreasing particle sizes of 6, 3 and 1 µm. Afterwards, the surfaces were electrochemically polished using a Struers D2 electrolyte in order to remove the residual deformation layer.

2.2. Pillar preparation

The sample preparation and inspection were performed inside a FEI Nova Nanolab 200 which is a dualbeam scanning electron and focused ion beam microscope (SEM/FIB). Electron backscatter diffraction (EBSD) measurements were performed using a Nordlys EBSD detector from Oxford Instruments which was attached to the FEI system. Energy dispersive x-ray diffraction (EDX) was used to estimate element concentrations in the precipitates of the DC04 steel and was performed on a Zeiss Supra 55 equipped with a detector from EDAX. After the microstructures of the samples had been determined by EBSD mapping, pillars with diameters of 2 µm and 4 µm were milled inside individual grains using the FIB. The pillars had aspect ratios between 2 and 3. For pillars with diameters of 22 µm, the time for the FIB machining is often too long and electrical discharge machining (EDM) was used instead. A similar way for sample fabrication can be found in [04]. Unfortunately, EDM leads to relatively rough surfaces which had to be removed by a FIB post treatment (Fig. 2.1b).

2.3. Microcompression experiments
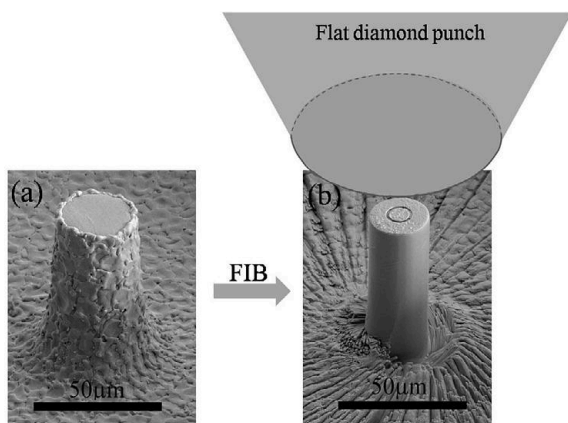
Figure 2.1: Micropillar prepared by EDM (a) and after FIB post treatment (b). Microcompression experiments were performed in a XP nanoindenter that is equipped with a flat diamond punch.

Microcompression experiments were performed in a nanoindenter (MTS, NanoXP) that was equipped with a flat diamond punch (Fig. 2.1b). For pillar diameters smaller than 8 µm, a punch with a diameter of 10 µm was used. For larger pillars, a diamond punch with a diameter of 100 µm was used.

3. Results

3.1. Microstructure of DC04 steel

The microstructure and texture after the hot rolling, cold rolling and heat treatment steps were investigated by EBSD measurements [05]. The results are used to verify texture models and phase field models that describe the evolution of the microstrcuture during cold rolling and recrystallization processes and can be found in the article of topic A1 and A3.

Fig. 3.1 shows EBSD results of cross sections that was machined in the cold rolled DC04 steel by FIB. The grains are strongly compressed and deformed after a cold rolling degree of 62 %. The maximum residual thickness of the grains is in the range of 10 µm, but most of the grains have thicknesses of less than 5 µm.

Figure 3.1: (a) EBSD results of a cross section prepared by FIB into the cold rolled DC04 steel.

For investigating the micromechanical behavior of the heat treated DC04 steel additional information of the microstructure are necessary. The SEM image in Fig. 3.2a shows a cross section that was machined into the heat treated DC04 steel by FIB. The image shows that the grains contain small features that have a mean size of 200 nm and a average spacing of roughly 2 µm. Fig.3.2b shows that these precipitates are also present in the micro machined pillars. EDX measurements performed on the heat treated DC04 steel reveal that the precipitates contain higher amounts of Mn and S (Table 3.1) than the matrix. Fig. 3.3 (a) and (b) show Kikuchi patterns received from EBSD measurement on the matrix and the precipitates. After subtracting the matix pattern from the precipitate pattern (Fig. 3.3c) and manually indexing of the resulting Kikuchi band (Fig. 3.3d), a α-MnS crystal structure can be related to the precipitates.
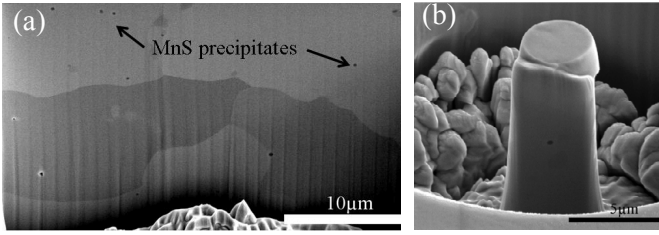
Figure 3.2: (a) Cross section of the heat treated DC04 steel. The matrix contains small precipitates that also were also found in the pillars (b)

Table 3.1: EDX results obtained from the matix and the precipitates

	Matrix	Precipitate
	wt%	wt%
S	0.11	4.01
Mn	0.58	8.15
Fe	99.3	87.84
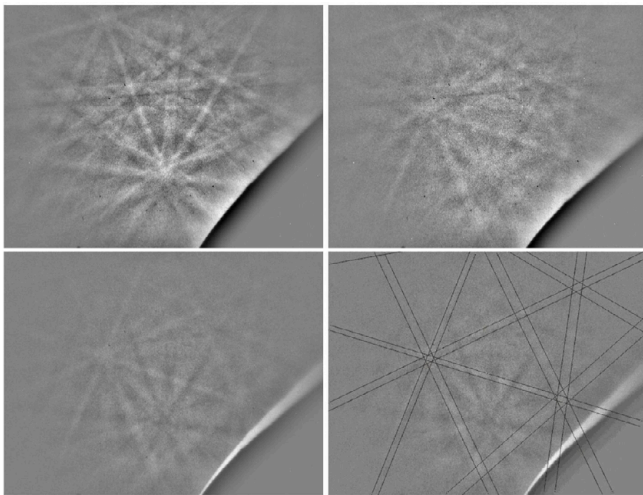
Figure: 3.3: Kikuchi pattern of the DC04 steel matrix (a) and the precipitates (b). The matrix pattern was subtracted from the precipitate patten (c) and the residual kikuchi bands manually indexed (d)

3.2. Microcompression experiments on DC04 steel

Fig 3.4 shows stress-strain data obtained on single crystalline DC04 steel pillars with diameter of 2 µm and 4 µm. The pillars were micromachined into grains with orientaions that were within 10 degrees of grains with <111>, <123> and <001> out-of-plane orientations. The results show that the strength of pillars with 2 µm diameter has a strong orientation dependence which becomes less pronounced with increasing pillar size.
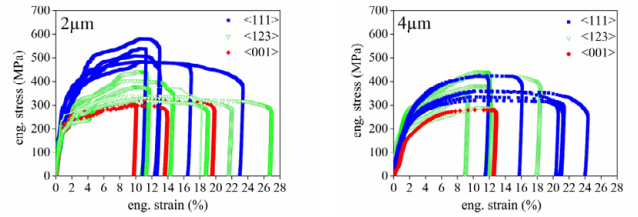
Figure 3.4: stress strain data of single crystalline DC04 steel pillars with diameter of 2 µm and 4 µm.

Afterwards, the deformed pillars were investigated by SEM. Fig 3.5 shows two representative SEM images for deformed pillars. From the images it can be seen that glide processes can occur not only one glide system but also on several glide system.
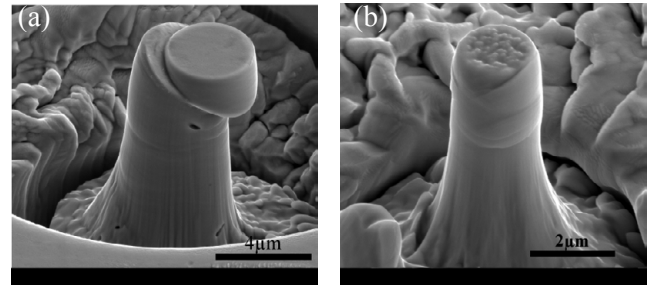
Figure 3.5: SEM images of single crystalline DC04 steel pillars with diameters of 4µm and <111> orientation (a) and 2µm (b) with <001> orientation.

Microcompression experiments were not only performed on single crystalline pillars but also on larger polycrystalline pillars with diamter of 22 µm. Fig. 3.6 shows an image of a compressed polycrystalline pillars and the corresponding stress-strain data. Deformation in the polycrystal is based on glide inside individual grains but glide steps can also extend across grain boundaries. The stress-strain data shows that larger pillars have a deformation behavior and strength that is somewhat similar to what is found for the bulk material in tensile experiments.
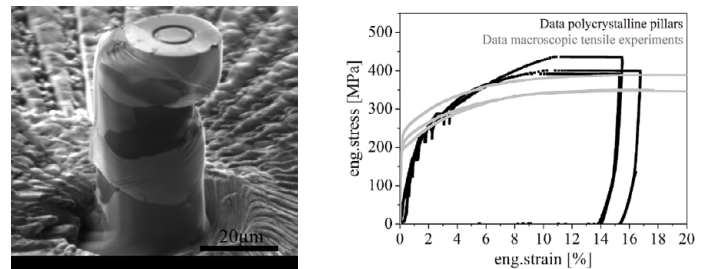
Figure 3.6: SEM image of a compressed polycrystalline DC04 steel pillar and corresponding stress-strain data.

4. Discussion

In the heat treated DC04 steel, a different deformation behavior is found for pillars with diameter of 2 μm and 4 μm. In pillars with a diameter of 2 μm, <111> orientations have higher strength than pillars with <123> and <001> orientations. This strength is even higher than the measured bulk strength that was determined in tensile experiments. The orientation dependence becomes negligible for pillars with diameter of 4 μm. In this case pillars with <123> and <111> orientations have the same strength and reach the bulk strength of the material. Even polycrystalline pillars with diameter of 22 μm show strengths comparable to what was found in tensile experiments. For micromechanical simulations of deep drawing processes (topic A2) compression data of single crystalline pillars with 4 μm diameter were used. Our results show that these data already represent the macroscopic deformation behavior of the material and thus can be used to optimize the material model. Usually, for bcc materials that are mechanically tested with samples sizes in the μm range, a size dependant behavior of the strength [06] can be observed. Within this size dependent region, the flow stress of the material increases with decreasing sample size. For pure α-Fe this size dependent behavior was observed up to sample sizes of 6 μm, where the flow stress was still higher than the expected bulk strength [07]. DC04 steel and α-Fe have both ferrite crystal structures and a similar mechanical behavior for both of them was expected. Instead, in the heat treated DC04, pillars with 4 μm diamters reach the bulk strength. Several reasons can explain this behavior. Compared to pure α-Fe, DC04 steel contains small amounts of C that is partially dissolved in the lattice at room temperature. Wert at al [08] already showed that only few % of C can increase the flow stress significantly. In chapter 3.1 we showed that DC04 steel contains small MnS precipitates with a spacing of ~2 μm that also may influence the motion of dislocations and increase the strength of the material.

5. References

[01] Bleck W. et al., 2004, Determination of input data for numerical design of sheet steels – Report on a common research project of the steel and automotive industry, Mat.-wiss. u. Werkstofftech.35, No. 8

[02] Wegst C., Stahlschlüssel, 21.Auflage, 2007, ISBN 978-3-922599-24-1

[03] Uchic M.D., et al., Sample Dimensions Influence Strength and Crystal Plasticity, 2004, Science 305, 986

[04] Uchic M.D., Dimiduk D.M., A methodology to investigate size scale effects in crystalline plasticity using uniaxial compression testing, 2005, Material Science and Engineering A 400-401 268 – 278

[05] Schendel S., Mönig R., Kraft O., 2010, Experimentelle Charakterisierung der Gefügeentwicklung und des plastischen Verhaltens von DC04 Stahl. Begleitband zur 1. jährlichen Klausurtagung Graduiertenkolleg 1483, Begleitband zum 3. jährlichen Symposium CCMSE, Hrsg: R. Pabst, B. Nestler, V. Schulze, Shaker Verlag, Aachen, 11-15

[06] Schneider A.S., Correlation between Critical Temperature and Strength of Small-Scale bcc Pillars, 2009, PRL 103, 105501

[07] Kaufmann D., 2011, Size Effects on the Plastic Deformation of the BCC-Metals Ta and Fe, Cuvillier E, ISBN: 978-3-86955-654-3

[08] Wert C.A., Solid Solubility of Cementite in Alpha Iron, 1950, Journal of metals, Vol 188: 1242 - 1244

Graduate School 1483
Process Chains in Production:
Interaction, Modelling and Assessment of Process Zones
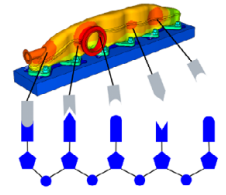
Influence of broaching for evaluation of process chains

V. Schulze, R. Pabst, H. Meier

wbk - Institute of Production Science, KIT - Karlsruhe Institute of Technology

Broaching is a highly effective manufacturing method to create complex structures on inner or outer surfaces. It is characterized by short machining times, simple machine technique and high automation. To identify the effects of broaching on the components, experiments with different tools and cutting speeds have been performed on SAE 5120 low alloyed steel. Parts machined with determined sets of process parameters have been subjected to a subsequent case hardening step to show the effect of residual stress formation after broaching to potentials of distortion. In addition, the influence of the tool´s minor cutting edges to the formation of cutting forces has been shown.

Machining, Force, Broaching

1. Introduction

To produce certain products/components, it is necessary to run through multiple single processes. Each of these single processes affects the component in its (surface) condition and passes the generated component characteristics to the subsequent step of manufacturing. It is inevitable to know the influence of the process parameters of all production steps to control the component's condition and therefore to optimise the final product. The experimental results build a base for continuing simulations which allow to gain further information of tool or component locations that are not accessible during experimental research.

2. Broaching As Part Of A Process Chain

Especially in automotive industry broaching is used to generate complex geometries on inner or outer surfaces, i.e. components assembled in powertrain applications. After machining very often a heat treatment step is carried out to enhance i.e. wear behaviour or to improve material strength. To remove undesired distortions a hard machining step is further conducted. This work describes the effects of broaching to the resulting forces and therefore changes in component behaviour to evaluate the desires of subsequent production steps to keep distortion small or to reduce hard machining steps which will lead to saving in time and costs.

2.1. Experimental Setup

All broaching experiments were performed on a modified inner broaching machine type Karl Klink RISZ 100/1600/500. The workpiece clamping device was installed on a Kistler platform dynamometer (Z 10440) complemented by three charge amplifiers Type Kistler 5015A to record the cutting forces during broaching.
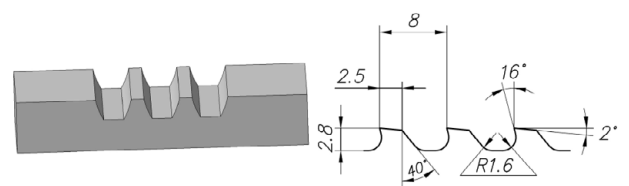
Figure 1: workpiece 'plane plate' (left), broach geometry (right)

Figure 1 (right) shows plane plates which were machined during the experiments. They were prepared from SAE 5120 case hardening steel with dimensions of 50 x 19 x 9 mm³ from bar material. The root/addendum spacewidth of 3.42/4.88 mm with pitch of 7.85 mm was adapted from the demonstrator shift collar. Before broaching the plates underwent a normalizing treatment at 880 °C for one hour with a subsequent isothermal aging (650 °C/30 minutes) and a stress relief annealing (650 °C/60 minutes) after the final milling. A pull broach with 3x88 teeth and a rise per tooth of 40 µm (total cutting depth: 3.5 mm) was

one the one hand coated with a TiAlN layer (friction coefficient $\mu = 0.3$) and on the other hand with an AlCrN layer (friction coefficient $\mu = 0.35$). Other specifications can be taken from Figure 1 (left). The cutting speed was set to 7, 10, 20, 30, 40 and 50 m/min without using any coolant (dry machining). During this research tool wear was not considered. To prevent influence of wear the broach was regrinded permanently.

2.2. Results

The occurring cutting forces during machining were related to the cutting cross section A which consists of tool pitch and width of each tooth to get specific forces. To calculate the specific forces, the cutting forces were measured during the experiment and a mean value over all 88 broach tool teeth was calculated. Figure 2 shows the specific cutting forces of both tools with the two coatings at all 6 different cutting speeds. It can be seen, that both coatings show the same trend in forces, but the values of the AlCrN-coating ly 14 ±2 % above the TiAlN-coating.
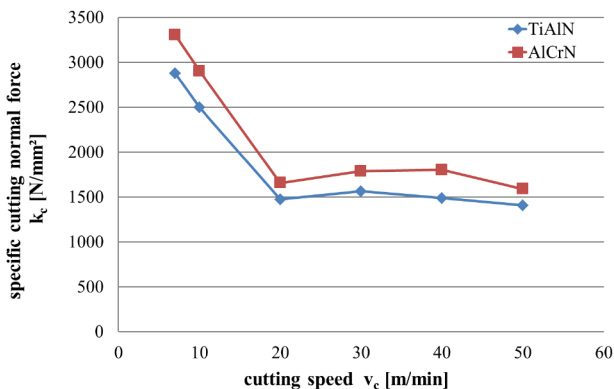
Figure 2: specific cutting forces during machining

This refers to the increase of the friction coefficient of 16 %. The highest specific forces occur at low cutting speeds of 7 m/min with 2877 MPa (TiAlN); 3303 MPa (AlCrN) and 10 m/min with 2497 MPa (TiAlN); 2903 MPa (AlCrN). At a cutting speed of approximately 20 m/min the cutting forces level out at 1500 MPa for the TiAlN-coating and about 1750 MPa for the AlCrN-coating. After broaching residual stress measurements were performed as described in [1]. For decreasing cutting forces at higher cutting speeds dry machining leads to larger normal residual values at the surface levelling out at 480 MPa. At a cutting speed of 7 m/min the residual stress shows its lowest value of 200 MPa. Figure 3 shows the residual stress distribution after broaching using the TiAlN-coating at a cutting speed of 30 m/min. The bulge at a depth of 10-20 μm comes with the electrolytic polishing process due to lack of resolution. It can be seen, that ten-

sile stress occurs at the surface whereas maximum compressive stresses of 258 MPa can be detected at a depth of 22 μm.
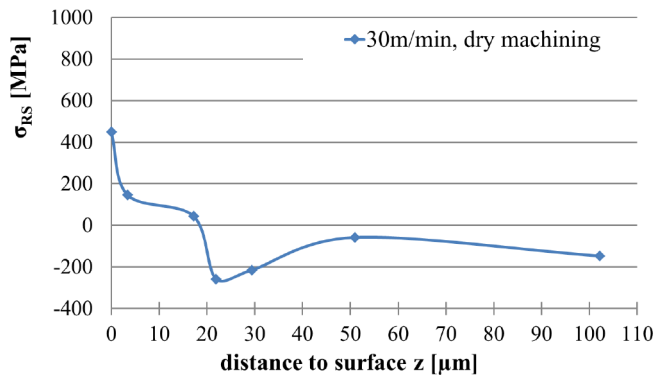
Figure 3: residual stress distribution after broaching

Based on the workpieces machined dry with 30 m/min cutting speed and use of the TiAlN-broach, the subsequent step in the process chain is case hardening and leads to convex tooth root surfaces with low distortion of 12 mm perpendicular to the machined surface [1].

3. Influence Of The Minor Cutting Edge

To describe machining processes, it is necessary to focus on the cutting edge. Depending of its geometry load occurs on the tool itself as well as on the machined surface. This has variable impacts on the generated component condition. Therefore the influence of the minor cutting edge to the development of cutting forces has to be emphasized.

3.1. Experimental Setup

The machine setup and thermal treatment of the workpieces was as described in 1.2. A broach with two single uncoated cutting inserts of ASP 60 (as shown in Figure 5 and Figure 5) was used with a pitch of 45 mm at a rise per tooth of 90 μm applied. The first insert is responsible for a defined cut and a plane resulting surface. Insert two makes the ultimate cut and was further analysed.
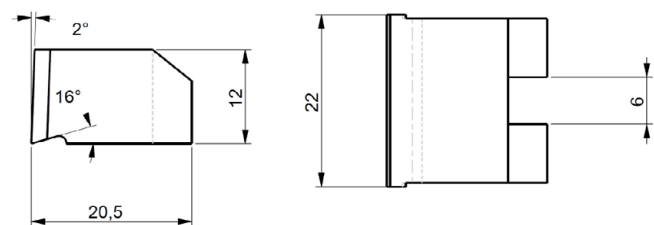
Figure 4: Cutting Insert 1: Prebroaching
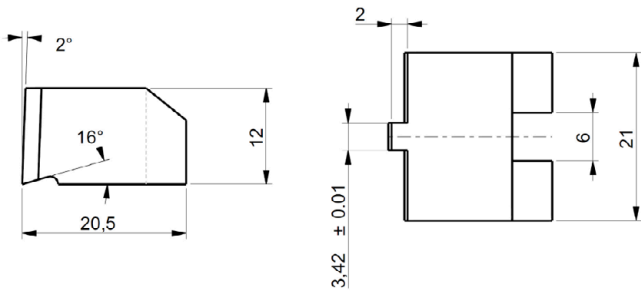
Figure 5: Cutting Insert 2: Main-Cut

The workpiece with a cone-shaped nose-piece is shown in Figure 6 and was designed in a way that insert two starts machining in an orthogonal cut where no influence of the minor cutting edge occurs. Furtheron it merges into a full cut with the minor cutting edges engaged.
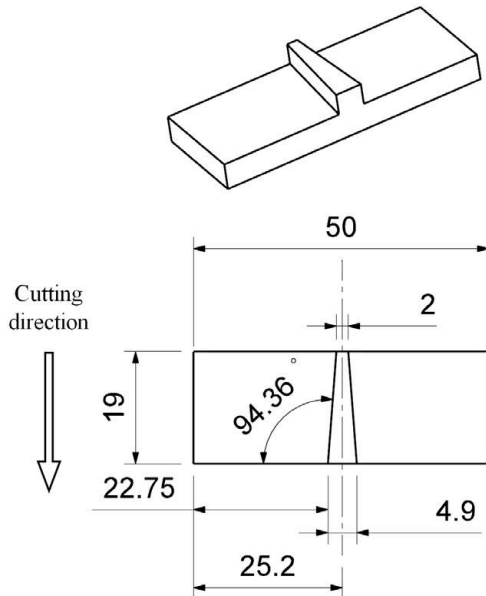
Figure 6: Workpiece 'Cone-Shaped Nose-Piece

Due to the fact that the width of cut during one stroke is not constant, the cutting forces have to be measured and analysed at different points in time. Figure 7 shows the exemplary force plot including the measuring points, depending on the broached distance. First point is the tool entry T_{begin} showing a characteristic local maximum due to elastic-plastic deformation of tool and workpiece. T_{2mm} represents the absolute orthogonal cut after 2 mm cutting distance. The third point was set when the minor cutting edge is definitely in contact (at 10 mm distance). T_{end} was chosen nearly at the end of cut.
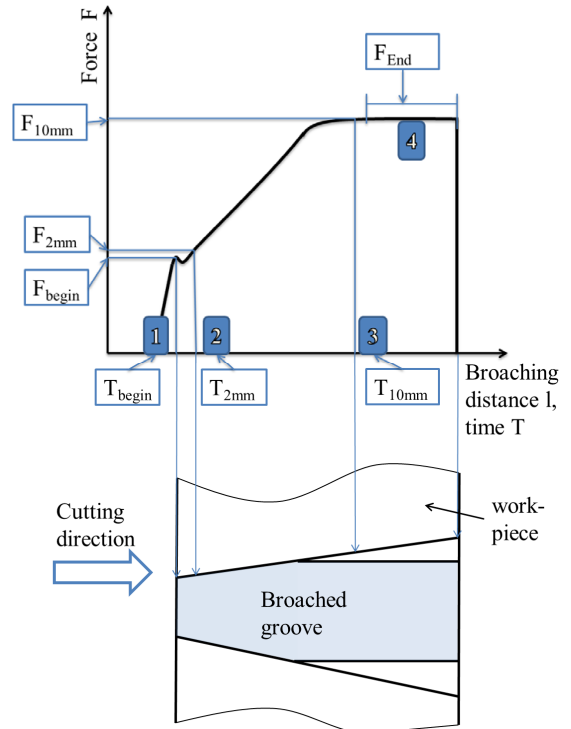
Figure 7: Force Plot With Defined Measuring Points

To gain an optimal analysis it would have been beneficial to set a measuring point directly at the changeover from orthogonal to full cut. This was not possible because one minor cutting edge always was in contact earlier than the other.

3.2. Results

In dry machining at all speeds of cutting the specific forces increase beginning from tool entry to a broaching distance of 10 mm.
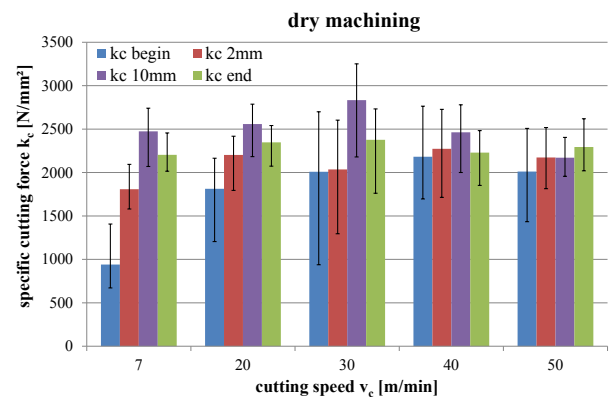
Figure 8: Specific Cutting Forces At Defined Time Steps In Dry Machining

Except at a cutting speed of 50 m/min the cutting force decreases a little before tool exit. As Figure 8 also shows, large scattering within sets of experiments can be detected. This is due to the rigidity of the ma-

chine and the clamping device itself and is also caused by only one cutting edge simultaneously in contact. For low cutting speeds the changeover from orthogonal to full cut is clearly visible (rise of the specific forces from $kc_{\_2mm}$ to $kc_{\_10mm}$). The higher the cutting speed the lower the difference between these two values.

When using the lubrication fluid Cutmax UP8-27, there is a similar trend as in dry machining (Figure 9). In general, the specific cutting forces are lower compared to dry machining which can be traced back to the reduction of the friction coefficient.
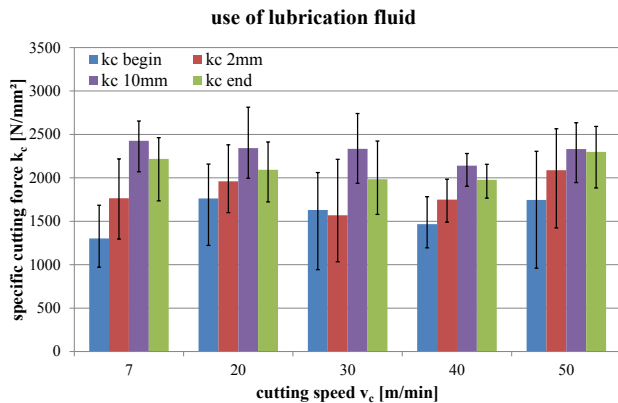
Figure 9: specific cutting forces at defined time steps with use of lubrication fluid

To set up a relationship for the influence of the minor cutting edge to the formation of the cutting forces, a ratio of full contact of the minor cutting edges (kc_end) to orthogonal cut (kc_begin) was built and is shown in Figure 10.

$$\alpha = \frac{k_{c\_end}}{k_{c\_begin}}$$

It can be seen, that α decreases with increasing cutting speed in dry machining as well as with use of lubrication fluid. It decreases from α=2.34 at 7 m/min in dry machining to α= 1.02 (α= 1.7 cutting oil) at 40 m/min. With use of lubrication fluid alpha shows the minimum at 20 m/min and increases slightly with rising speeds. From 20 m/min and higher, alpha levels out at values between 1 and 1.35. This has also been detected from [2] where the minor cutting edge affects the occurring forces during hard turning by the factor 1.15.
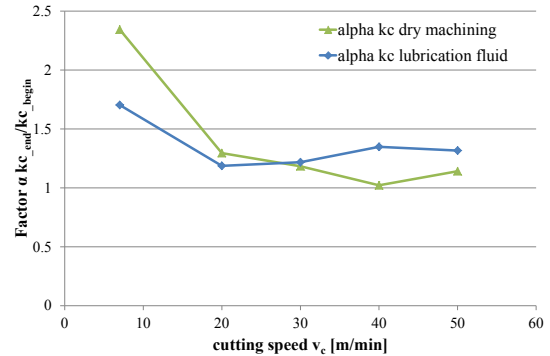
Figure 10: Influence Of The Minor Cutting Edge: Ratio alpha

4. Conclusion and Outlook

The objective of the study was to identify the effects of broaching SAE 5120 with different tools to the formation of cutting forces and its effects to the workpiece. Five different cutting speeds in dry machining were examined and the specific cutting forces were analysed. It has been detected, that at cutting speed higher than 20 m/min the occurring level out at about 1700 MPa. A further analysis on the influence of the minor cutting edge was performed. At low cutting speeds an influence of the minor cutting edge is given (factor 1.5-2.3) which becomes smaller with higher velocities. Further work will focus on the influence of the occurring cutting forces to evolution of residual stress and subsequent to distortion. Additional, cutting speeds higher than 50 m/min and the influence of cutting edge preparation will be taken into account.

5. Acknowledgement

6. References

[1] Schulze, V.; Pabst, R.; Meier, H.: Research Training Group 1483 - Process chains in manufacturing: Interaction, modelling and evaluation of process zones, in: IDE 3rd International Conference On Distortion Engineering 2011, 14. -16. September 2011, Proceedings IDE 3rd International Conference On Distortion Engineering 2011, p. 421-428.

[2] Zhao, W.: On study of cutting forces generated by minor cutting edge; in Materials Science Forum, 2006, issue 532-533; p. 484-487

Graduate School 1483
Process Chains in Production:
Interaction, Modelling and Assessment of Process Zones
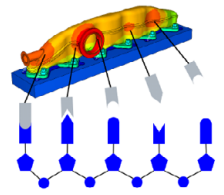
Local analysis of process induced residual stress distributions for complex geometries – example: internal gearing of a gearshift sleeve

T. Strauß, J. Gibmeier, A. Wanner

Institut für Angewandte Materialien – Werkstoffkunde (IAM–WK)

The main objective of this study is the (non-destructive) stress analysis of the local residual stress distribution at the tooth-root-surface of a gearshift-sleeve and the impact of stepwise sectioning of the ring structure on the local residual stress state. Residual stress analyses were carried out by means of energy dispersive diffraction using high energy synchrotron X radiation (EDXRD). The analysed components were examined after subsequent process steps of the industrial process chain, i.e. soft-machining by means of broaching and case hardening. The obtained results are essential for the validation of the process simulations of the graduate-school-1483 (funded by the German-research-foundation, DFG) and in order to develop a strategy to measure local residual stress distribution at the tooth-root-surface of the inner gearing by conventional laboratory X-ray sources. The results show that partial sectioning of the component with the aim to get access to the inner gearing for conventional X-ray stress analyses does have an insignificant impact on the local residual stress state. The residual stresses after broaching are tensile and show a steep gradient in depth in the near surface region. After case hardening compressive residual stresses are observed which have a much larger reach in depth as the tensile residual stress distribution near the surface of the component after soft machining.

process chain, broaching, residual stress, surface layer characterization

1. Objectives

The aim of the current study was to determine the local residual stress distributions at the tooth-root-surface of a gearshift sleeve (Fig. 1) after the process steps soft-machining and case-hardening using high energy synchrotron X-ray diffraction. The strategy for using synchrotron radiation from large scale facilities was chosen, since the inner gearing of the gear shift sleeve is not accessible by means of conventional X-ray stress analysis using laboratory X-ray sources. Here the components have to be sectioned in order to gain access to the inner gearing. Due to the geometry of the inner gearing, the measuring point in the ground of the tooth is difficult to access. For X-ray stress analysis according to the sin²ψ-method the sample has to be tilted with respect to the incident X-ray beam. Here, a shadowing occurs and the applicable ψ-tilts are extremely limited by the geometry of the teeth as explained in [1]. Access to the ground of the tooth can be gained by sectioning of the component. However, the sectioning results in a redistribution of the local residual stress distribution, which has to be taken into account for the valuation of the residual stress data. Using high energy synchrotron radiation enables the possibility to obtain residual stress data from the inner gearing prior to sectioning of the gear shift sleeve. The application of the similar set-up for sectioned parts gives insight into the magnitude of the redistribution due to cutting. Here energy dispersive X-ray diffraction using high energy synchrotron radiation was applied for gear shift sleeves that were intact (not sectioned) to determine the tangential residual stress component using the sin²ψ-method. Further, the same set-up was applied for components that were opened by diamond wire saw cutting and for sections of the ring structure that were first cut and then the teeth being adjacent to the groove were partly removed by means of electrical discharge machining to ensure larger tilt angles necessary for application of X-ray stress analyses at laboratory sources following the sin²ψ-method. The use of EDXRD and photon energies between 20 – 150 keV at the EDDI beamline at

Bessy (Berlin, Germany) enables residual stress analysis for all phases (ferrite/martensite and austenite) that contribute to the diffraction spectrum. Since for diffraction peaks that occur at different photon energies different information depth can be assigned the depth distribution of the phase specific residual stresses can be determined up to information depths of approximately 70 µm [2].

2. Samples geometry and manufacturing

The sample manufacturing and sample preparation is carried out by the project partners B1 and B3 within the GraKo 1483 as well as by a network of associates in industry. The results shown are obtained with an Industrially manufactured automotive gearshift sleeve after broaching and case hardening. Broaching is a viable technique to produce complex geometries on inner or outer surfaces with high accuracy and good surface quality.
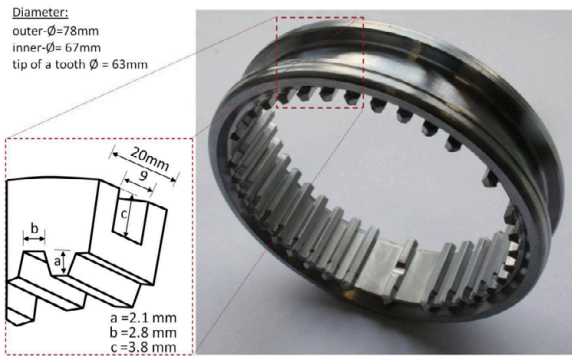
Figure 1: Geometry of the gearshift sleeve including measuring positions 1, 2 and 3(MP1, 2, 3)

To gain extensive information about the residual stress distribution in depth for a single process step and the interlinked manufacturing process chain, soft broached and case hardened gearshift sleeves of case hardening steel SAE 5120 (German grade: 20MnCr5) with an outer diameter of 78 mm and an inner diameter of 67 mm (Fig. 1) were analyzed. The residual stress analysis is concentrated on the internal gearing of the gear shift sleeve with root/addendum spacewidth of 2.8/3.4 mm and a pitch of 6.8 mm manufactured by inside broaching. A cutting speed of $v_c = 7$ m/min with use of cooling lubricant was used. Former investigations showed that best tool wear behavior can be achieved by dry machining and cutting speeds of 7 m/min [3]. At the following process step casehardening the soft-machined gearshift sleeves were carburized at 870°C and slowly cooled down without a transformation of martensite. These precarburized cooled down samples were heated up with electrostatic induction for a second time and quenched directly with the polymer solution.

For each gearshift sleeve the residual stress distribution in the depth has been analysed at three different positions at intervals of 120° (see Fig. 1). In order to analyse the effects of sectioning in detail, residual stress analyses were carried out for non-sectioned and sectioned components. Further a partial removal of adjacent teeth of the gearshift-sleeves was studied. Measuring points differ in the geometry of the adjacent teeth. Measuring point 1 (MS1) (see Fig. 2) has its original tooth geometry without any changes. Measuring points 2 and 3 (MS2 and MS3) are characterized by a partial removal of the surrounding teeth by wire electrical discharge machining. They principally enable the analysis of the surface-near residual stress components along and perpendicular to the broaching direction by conventional laboratory X ray experiments. For example, for the residual stress component perpendicular to the broaching direction (tangential direction) ψ-tilts in the range of ±50° for MS2 and ±60° and more for MP3 are possible when studying the {211}-ferrite peak at 2θ of approximately 156,1°. This can be assumed being sufficient for X-ray stress analysis according to the sin²ψ - method as recommended in [4].
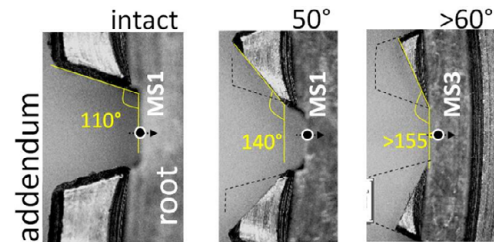
Figure 2: partial removal of adjacent teeth

3. Achievements

3.1. Microstructure and micro hardness analyses

Cross sections of the broached gearshift sleeve were metallographically prepared to analyze the microstructure using optical light microscopy. Micro hardness measurements were carried out by means of a Vickers micro hardness measuring system of type Shimadzu HMV 2000 using a test load of 10 g (HV0.01). For all tested samples a minimum of 30 single measurements was considered necessary to obtain a reliable mean value.

3.2. Residual stress analyses

The residual stress analyses were carried out by means of energy dispersive X-ray diffraction (EDXRD) at the EDDI-beamline at Bessy (Berlin, Germany) according to the sin²ψ-method [5]. The angle between the incident beam and the samples surface was adjusted to 6°.

The detector-system was positioned at 2θ angle of 12°. The primary beam was defined by slits of 1.2 μm × 5 mm. The secondary slit size was adjusted to 120 μm 5 mm (equatorial × axial). Using this set-up the {110}-, {200}-, {211}-, {220}-, {310}-, and {321}-interference lines of ferrite/martensite and the {111}-, {200}-, {220}- and {311}-, {222}-interference lines of austenite were recorded within one X-ray diffraction spectrum. The stress measurements were carried out in tangential direction (perpendicular to broaching direction), which is the direction that is more relevant for the analysis of residual stress redistributions caused by sectioning, in the middle of the tooth-root-surface. All residual stress distributions were determined according to the sin²ψ-method using 32 different sample tilts between ψ = 0°..88°. A mean information depth τ was assigned to the individual diffraction lines according to $\tau = \frac{1}{2} \times (\tau_{max} (\psi = 0°) + \tau_{min} (psi_{max})$, thus a residual depth profile was obtained for the separate phases for each of the individual measuring points.

4. Results

4.1. Microstructure and micro hardness analyses

A metallographic cross-section for samples after the broaching process is presented in Fig 3 (a) showing a ferritic pearlitic structure and a deformation region of approximately 20-30 μm near the very surface caused by the broaching.

(a)   (b)
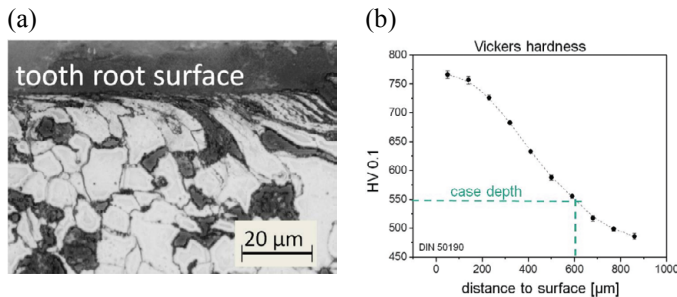
Figure 3: (a) Cross-section of broached samples: general view in broaching direction (b) micro hardness results of the tooth root surface after case-hardening

Here the structure is characterized by sheared grains with its orientation in the direction of broaching. Accordingly, it is expected that the residual stress distribution after soft broaching is concentrated in this surface-near region. Futher, Fig. 3 (b) shows hardness values after case hardening indicating a case depth of approximately 600μm.

4.2. Residual stress analyses

The three measurement points (MS1, 2 and 3) (Fig. 1) have been analyzed at non-sectioned and sectioned

gearshift sleeves after soft machining and case hardening. The part of the results which are shown here are mainly from the ferrite/martensite phase. The residual stress distributions at MS1 of non-sectioned and sectioned gearshift sleeves after soft- and hard-machining and for MS1, 2 and 3 for a non-sectioned case-hardened gearshift sleeve are compared. The impact of the second phase on the macroscopic residual stress state will be addressed briefly
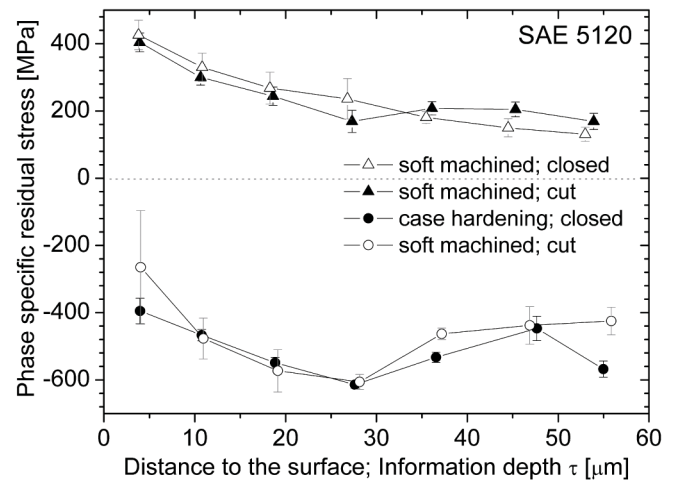
Figure 4: Phase specific residual stress distributions in the depth in the ferrite/martensite phase for non-sectioned (closed) and sectioned (cut) gearshift-sleeves measured at the tooth-root-surface, residual stress component in tangential-direction

In Fig. 4 an example for results of the EDXRD stress analyses is presented for the residual stress component perpendicular to the broaching direction. The residual stress analyses of the ferrite/martensite phase show for all soft-broached gearshift sleeves tensile residual stresses with a steep gradient. Highest normal residual stress values are determined near the surface. As a consequence of the case-hardening process the surface-near tensile residual stresses are transformed into compressive residual stress with a large range in depth in the martensite phase. There are only minor differences between the non-sectioned state and the state after the first cut (opened) in the characteristic distribution of the local residual stress distribution at the tooth-root-surface and in the depth as also shown in Fig. 4

The residual stress distributions for the retained austenite phase for samples after case hardening are presented in Fig 6, showing compressive residual stress with a large range in depth as in the martensite phase. Using the phasespecific residual stress data and the local volume fractions of the two phases macro residual stress distribution were calculated using a simple rule of mixture.The volume fraction was determined by retained austenite analysis using the 6-line-method

at laboratory X-ray sources and Mokα-radiation. The data show that the magnitude of the homogeneous micro residual stresses is only small and that after case hardening predominantly macro residual stresses were determined.

Figure 5: Phase specific residual stress distributions in the depth of the tooth root in martensite caused by removal of the surrounding teeth, residual stress component in tangential-direction

5. Conclusion

The residual stress redistribution at the tooth root caused by stepwise removal of the surrounding teeth and the redistribution caused by sectioning the ring structure was determined non-destructively. These results are an important step for the development of a strategy to measure the residual stress distribution by means of conventional laboratory X-ray sources according to the sin²ψ-method. At the tooth root the soft machined gearshift sleeves show tensile residual stresses with a steep gradient. Highest normal residual stress values are determined near the surface. After the case hardening process the surface-near tensile residual stresses are transformed into compressive residual stress with a large range in depth in the martensite and retained austenite phases. The analyses have shown that predominantly macro residual stresses exist after case hardening.

The residual stress distributions for the retained austenite phase for samples after case hardening are presented in Fig 6, showing compressive residual stress with a large range in depth as in the martensite phase. Using the phasespecific residual stress data and the local volume fractions of the two phases macro residual stress distribution were calculated using a simple rule of mixture. The volume fraction was determined by retained austenite analysis using the 6-line-method at laboratory X-ray sources and Mokα-radiation. The data show that the magnitude of the homogeneous micro residual stresses is only small and that after case hardening predominantly macro residual stresses were determin. With residual stress analysis using high synchrotron X-ray diffraction the impact of sample

preparation on the residual stress distribution at the tooth root was studied in detail.
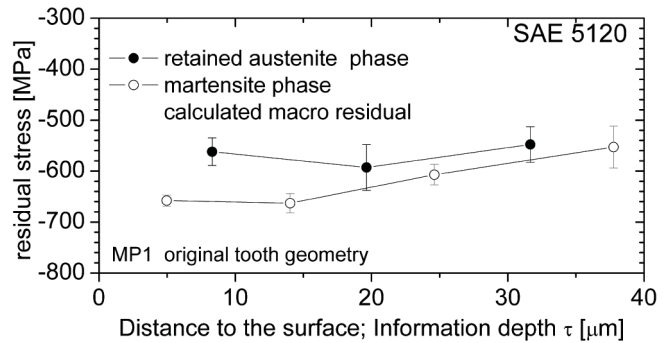
Figure 6: Phase specific residual stress distributions in the depth in the ferrite/martensite phase for non-sectioned (closed) and sectioned (cut) gearshift-sleeves measured at the tooth-root-surface, residual stress component in tangential-direction

The results show that both preparation steps, cutting the ring structure into pieces and the removal of the surrounding teeth by means of electrical discharge machining, do not change the characteristics of the residual stress distribution at a near surface region up to depths of approximately 50 ..70 µm. Thus, in order to measure the residual stress at the tooth root it is principally possible to section the gearshift sleeve to a segment to gain access to the measuring point for X-ray stress analysis using conventional laboratory X-ray sources..

6. References

[1] T. Strauß, J. Gibmeier, A. Wanner: Analyse von prozessbedingten Eigenspannungen –Begleitband zur 1. Klausurtagung 2010

[2] V. Hauk, H.-J. Nikolin,: Evaluation of Deformation Residual Stresses Caused by Uniaxial Plastic Strain of Ferritic and Ferritic-Austenitic Steels, Z. Metallkde. 81 (1990), S. 556-569

[3] H. Meier, R. Rilli, V. Schulze: Nass- u. Trockenräumen von 16MnCr5, Proceedings of Graduate School 1483 and CCMSE, 25.-26.Feb. 2010

[4] B. Scholtes, H.-U. Baron, H. Behnken, B. Eigemann, J. Gibmeier, T. Hirsch, W. Pfeifer: Röntgenographische Ermittlung von Spannung – Ermittlung und Bewertung homogener Spannungszustände in kristallinen, mikroskopisch isotropen Werkstoffen, Verfahrensbeschreibung der AWT e.V., FA 13 (2000),p. 1-55

[5] E. Macherauch, P. Müller: Das sin²ψ-Verfahren der röntgenographischen Spannungsmessung, Z. angew. Physik, 13 (1961),p. 305–312

Graduate School 1483
Process Chains in Production:
Interaction, Modelling and Assessment of Process Zones
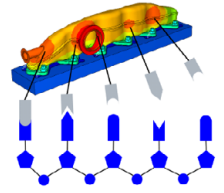
Relaxation of residual stresses induced by soft machining and generation of distortion during the heating step of a case hardening treatment

D. Stancheva, K. Moch, T. Strauß, J. Hoffmeister, V. Schulze

Institute for Applied Materials, Karlsruhe Institute of Technology (KIT)

As a result of soft machining, residual stresses are induced into a component. During heat treatment, these can be reduced by stress relieving, causing distortion. This suggests the assumption that thermal relaxation occurs during the heating step of a case hardening treatment. In order to reproduce a residual stress state of a broached component, notched workpieces were produced and heat treated by differing aging times and temperatures. The relaxed surface residual stresses were determined by X-ray analysis according to the $\sin^2\psi$-Method. Subsequently, the thermal residual stress relaxation was modelled by the Zener-Wert-Avrami approach as well as by the Garofalo approach in order to be used in a finite element simulation model in ABAQUS/Standard. The results of the experimental investigations and the simulations show that the thermal residual stress relaxation during heating increases considerably with higher temperatures, long aging times, and small heating rates. Especially on the surface and its immediate proximity, a strong relaxation rate occurs. However, the distortion due to the heat treatment is negligibly small for the investigated geometry.

Residual Stresses, Thermal Relaxation, Simulation

1. Introduction

Residual stresses are defined as stresses which occur in a workpiece without interaction of exterior forces and moments and can be separated into three categories [1,2]. First and foremost, the residual stresses induced by soft machining like broaching are macro residual stresses (I. Type) which are characterized by the production process they result of. Furthermore, there are micro residual stresses (II. and III. Type) in the material. Depending on annealing temperature, time and heating rate, the residual stresses of first and second type can be reduced considerably through stress relieving by temperatures above the recrystallization temperature [1,2]. Therefore, a relaxation of residual stresses during the heating step of a case hardening is expected. On the other hand, unwanted distortion is generated during the heat treatment as a result of the reduction of residual stresses [3], which has to be evaluated. Therefore, the aim of this research work is the modelling and simulation of thermal relaxation.

2. Experimental and Computational Methods

The first step is the experimental identification of residual stresses occurring in a notched component, followed by a heat treatment with different aging times and temperatures. In a second step, the thermal stress relaxation is described by the Zener-Wert-Avrami approach as well as by the Garofalo approach. The determined residual stresses have to be transferred into a numerical model in ABAQUS/Standard for the heat treatment simulation.

2.1. Experimental Investigation

In order to investigate the thermal relaxation of residual stresses, the case hardening steel AISI 4840 (SAE 5120) (DIN EN 20MnCr5) with the chemical composition given in Table 1 was used. The normalized material was heat treated in a salt bath at 870°C for 1 h followed by isothermal phase transformation at 650°C for 30 min, in order to guarantee the same initial microstructure.

Table 1: Chemical composition of AISI 4840

Element	C	Si	Mn	Cr
[Ma.-%]	0,212	0,169	1,333	1,276

S	Ni	Mo	Cu	Al
0,011	0,059	0,025	0,025	0,033

Specimens with a geometry of a round plate with ground surface (Figure 2) were produced and stress relief annealed (T = 650°C, t = 2h) before further preparation. Afterwards, a groove of 3 mm width was introduced in the middle of the samples (Figure 1). Since no appropriate broaching tool was available, the groove was cut into the specimen by an adjusted turning process, simulating broaching. This allowed a reproducible process in terms of residual stress state while at the same time reflecting the cutting kinetics during broaching. The tap holes at the back of the specimens were used to fix them on a plate with a large diameter. In order to generate samples with relative high residual stresses for the low aging temperatures and such with relative low residual stresses for the high aging temperatures, two different machining parameter sets (cutting speed v_C, chipping thickness h, cutting edge radius r_β, presence of emulsion), as specified in Table 2, were realised. Subsequently, the samples were subjected to thermal aging at four temperatures, namely 250°C and 350°C to produce high residual stresses, in addition to 450°C and 550°C for low residual stresses. Furthermore, for each temperature 5 different times 4 min, 15 min, 1 h, 4 h and 16 h were applied. Except for the treatments at 550 °C, a salt bath was used. In case of 550 °C, a radiation heater was used for the short treatments whereas a vacuum furnace for the long treatments. An X-ray stress analysis according to the $\sin^2\psi$-Method was performed before and after aging on all samples. The {211}-diffraction lines of α-ferrite phase were measured in the range of 148°≤ 2θ ≤164° with step size Δθ = 0,2° at 13 different angles -60°≤ ψ ≤ 60° using Cr-Kα radiation. A pin hole collimator with nominal dimensions of ø 0,5 mm was applied for the primary beam and a symmetrisation slit in front of the detector. The stress calculation was carried out using the Pearson VII fitting function [4], a Young's modulus $E^{\{211\}}$ = 219911 MPa and a Poisson ration $\upsilon^{\{211\}}$=0,28.

Figure 1: Sample with groove

v_C [m/min]	80	50
h [µm]	40	30
r_β [µm]	40	35
Emulsion	yes	no
σ^{RS} [MPa]	450	300

Table 2: Turning parameters
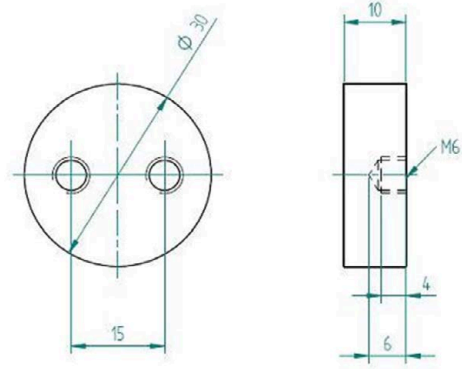
Figure 2: Sample geometry

2.2. Modelling of thermal relaxation

Reduction of the residual stresses occurs by introducing thermal energy into surface treated components. In the temperature range of $T < T_S$ (solidus temperature) this is due to creep and relaxation processes, which are based on two different mechanisms of dislocation motion. At lower temperatures dislocation core diffusion prevails and at higher temperatures volume diffusion characterised by an activation energy, being approximately the half or full activation energy for self-diffusion ($\Delta H_{S,\text{Fe}} = 4,45 \cdot 10^{-19}$ J), respectively. For modelling this behaviour, Vöhringer [5] proposed the Zener-Wert-Avrami approach:

$$\frac{\sigma^{RS}(T,t)}{\sigma_0^{RS}} = \exp\left\{-\left[C \cdot \exp\left(-\frac{\Delta H_A}{k \cdot T}\right) \cdot t\right]^m\right\} \qquad (1)$$

where $\sigma^{RS}(T,t)$ is the residual stress value after a time t at an absolute temperature T, σ_0^{RS} the initial value of the residual stress at room temperature, ΔH_A the activation energy of the process, m an exponent, C an velocity constant and the Boltzmann constant ($k = 1,38065 \cdot 10^{-23}$ J/K).

Another description of the thermal stress relaxation was porposed by Garofalo [6]:

$$\dot{\varepsilon}_p = A \cdot \left[\sinh\left(B \cdot \sigma_m^{RS}\right)\right]^n \exp\left(-\frac{\Delta H_N}{k \cdot T}\right) \qquad (2)$$

with $\dot{\varepsilon}_p$ the plastic strain rate, σ_m^{RS} the average residual stress magnitude, ΔH_N the activation energy, n an exponent and A and B constants. In order to use this approach, a transformation evaluation of the experimental data is necessary. From combining the residual stresses $\sigma_i^{RS}(T,t_i)$ and $\sigma_j^{RS}(T,t_j)$ $(j = i+1)$

remaining after different aging times t_i and $t_j (t_j > t_i)$ at $T = const$ with the temperature dependent Young's modulus $E(T)$, the plastic strain rate

$$\dot{\varepsilon}_{p,i} = -\dot{\varepsilon}_{e,i} = -\frac{\sigma_j^{RS}(T,t_j) - \sigma_i^{RS}(T,t_i)}{E(T) \cdot (t_j - t_i)} \qquad (3)$$

and the average residual stress magnitude

$$\sigma_{m,i}^{RS} = \frac{1}{2} \left| \sigma_j^{RS}(T,t_j) + \sigma_i^{RS}(T,t_i) \right| \qquad (4)$$

can be calculated.

2.3. Computational Method

2.3.1. Mapping of residual stresses

The numerical modelling and calculations in this paper were performed using ABAQUS/ Standard. As first step the residual stresses $\vec{\sigma}_{aim}^{RS}$ introduced by soft machining have to be transferred in the heat treatment simulation $\vec{\sigma}_n^{RS} = \vec{\sigma}_{aim}^{RS}$. Independently of whether the input information is coming from simulations or measurements, the residual stress distribution is mostly not known over the whole component. Therefore mapping of some stresses on a part of a component leads to a calculation of an equilibrium state in a balancing step, in which certain redistribution of the defined stresses and node displacements take place. In order to minimise these changes, a Matlab tool has been developed, whose operating sequence is schematically displayed in Figure 3. The initialisation from the stress state in Abaqus is introduced by means of the internal subroutine SIGINI. The tool passes a text file to Abaqus with the intended residual stress values as test variables, starts the calculation, and estimates the deviation between the test and the equilibrium residual stress values. It evaluates new test data by subtracting the deviation from the initial values and passes the information again to Abaqus. After a number of iterations specified by the user a final node correction is carried out. For this purpose a new node position is calculated by comparing the initial node position and the node position computed in the last iteration which is used for further simulations.
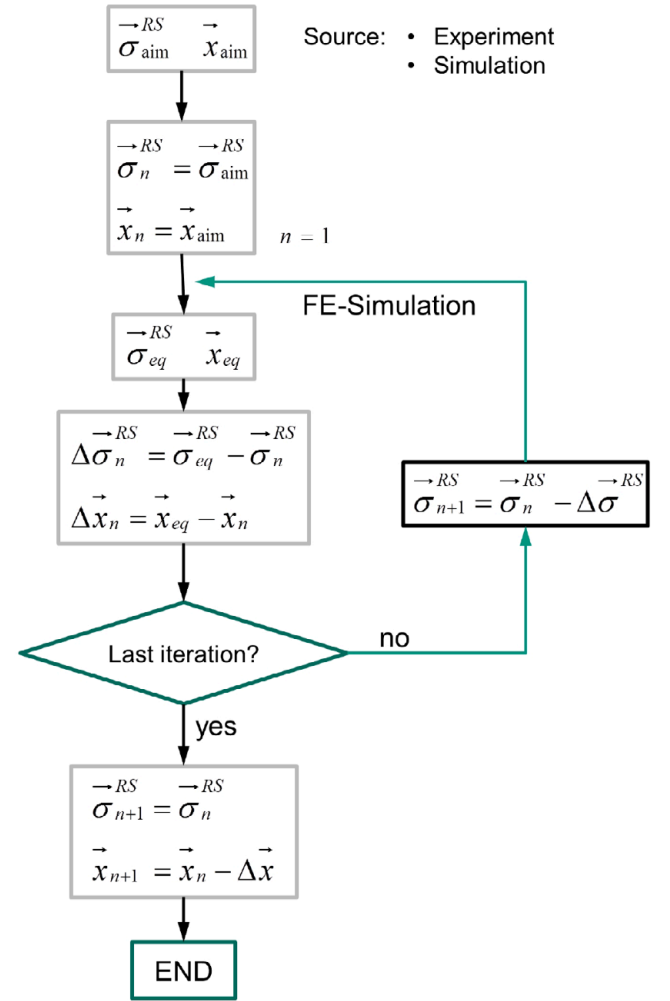
Figure 3: Operating sequence of the Matlab tool

2.3.2. Geometric model

The geometry used in project B within the Grako 1483 is a plane plate (9 x 19 x 50 mm) with three broached notches (root/addendum space width of 3,42/4,88 mm) (Figure 4 left). The first simplification is the consideration of only one fourth of the component due of symmetry reasons. Thereby a symmetry condition is defined on the separating planes and heat transfer conditions on the remaining surfaces. Further model abstraction in order to reduce the computing time is a plate representing the notch root only (Figure 4 middle). No further boundary conditions are specified on the additional cutting plane, while reducing the plate thickness to 1 mm. The mesh consists of hexahedron elements and is refined very strongly (Element edge 0,005 mm) near the upper surface (Figure 4 right), where the residual stresses have to be mapped in a thin layer of 0,05 mm. The input for the residual stresses was obtained from X-ray measurements in cutting direction at single points in one of the broached variants, which are displayed by symbols in Figure 5 and Figure 6. Along the notch, the residual stresses were

measured in three points which show that the residual stresses decline with increasing distance to the center of the specimen. These values were approximated by a linear function afterwards (Figure 5). Further measurements provide evidence of reduction of residual stresses with a value of 450 MPa on the surface with increasing surface distance. This decline can be described by an exponential function (Figure 6). A two dimensional stress state was mapped, assuming a rotational symmetry for the transversal stresses as a first approximation, since no data was available. The surface residual stress exceeds the elastic limit of the material in the undeformed state due to strain hardening. Therefore a different temperature-dependent yield strength was applied to the surface region, which corresponds to stress values at 0,1% plastic strain from the stress-strain-curve at different temperatures. Furthermore, the data from the two different initial stress states, one from the specimens aged at 250°C / 350°C and the other from the those at 450°/550°C, were evaluated separately. The thermal stress relaxation was implemented over the CREEP routine using the Garofalo approach, where an equivalent uniaxial creep strain increment is defined. The heat transfer was specified by means of heat transfer coefficient subjected to a variation from 10 W/(mm^2 K) for static air over 50 W/(mm^2 K) for moderately moving air up to 250W/(mm^2 K) for strongly moving air.
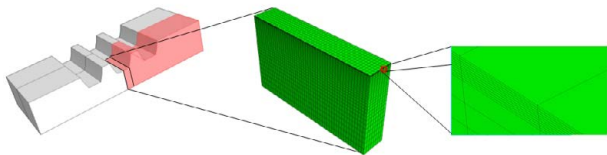
Figure 4: Geometric model
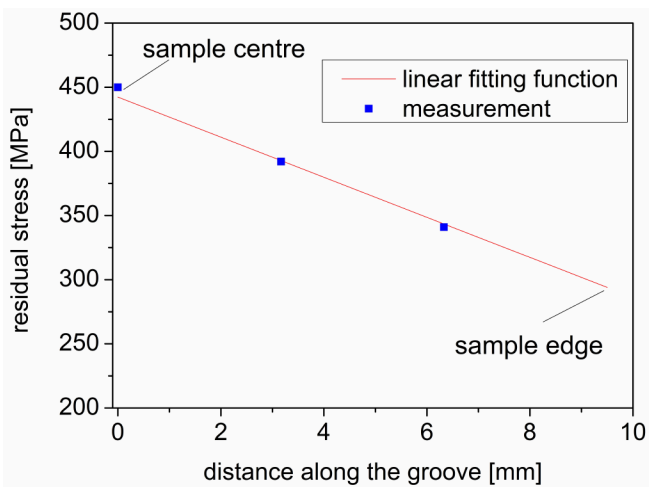
Figure 5: Measured residual stresses along the groove approximated by a linear function
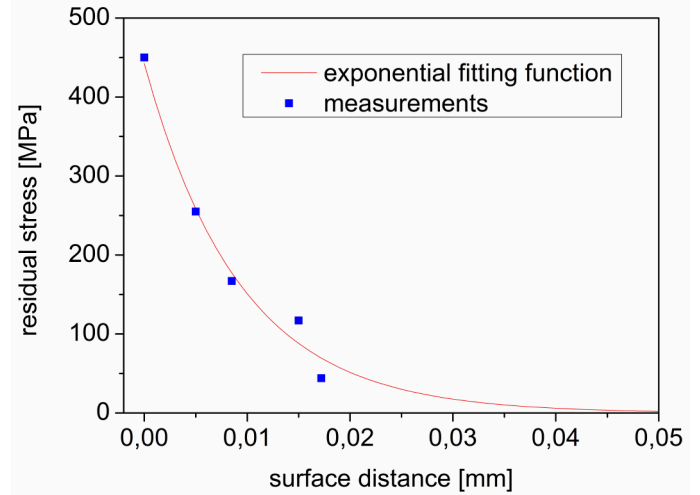
Figure 6: Mapped residual stresses in the depth described by an exponential function

3. Results and Discussion

The experimental results as well as the fitted parameters required for the simulations will be presented, followed by the simulation results.

3.1. Experimental Results and Modelling

The experimental results are summarised in Figure 7, where the ratio of the residual stresses before and after thermal aging are plotted versus the aging time at different temperatures. It can be observed that the relaxation of residual stresses increases considerably with higher temperatures, so that at 550°C the residual stress relaxation is nearly completed. Furthermore, a strong stress relaxation occurs within a short time, continuing thereafter with time but at much more moderate rates. Due to the measurement fluctuations, the transformation of the data in plastic strain rates is restrained and therefore the data were first fitted by Zener-Wert-Avrami approach (Figure 7). The data from the two different initial stress states, one from the samples aged at 250°C / 350°C and the other from those at 450°/550°C, were evaluated separately. With this approach, the parameters displayed in Table 3 were determined. The fact that this estimation leads to an activation energy of $1/2 \cdot \Delta H_{S,Fe}$ for the low temperatures and of $\Delta H_{S,Fe}$ for the high temperatures shows the validity of this proceeding (see section 2.2). Subsequently, the calculated data for the Garofalo approach based on parameters measured and fitted by Zener-Wert-Avrami are displayed in Figure 8 and Table 3. In order to preserve consistency, the fitting was performed again separately and the resulting fit parameters used for the simulations are listed in Table 3.
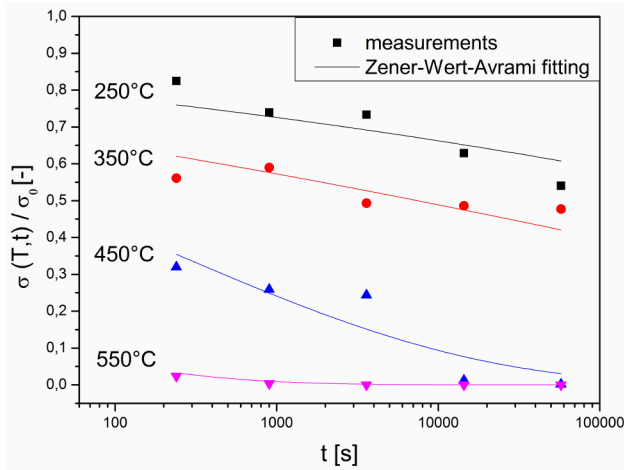
Figure 7: Experimental data and fitting by using the Zener-Wert-Avrami approach
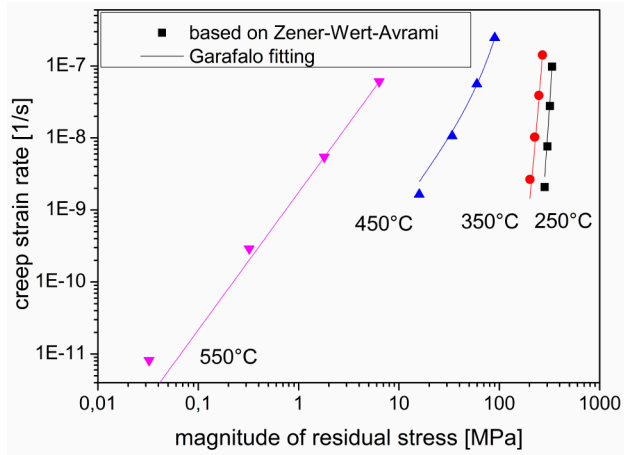
Figure 8: Experimental data and data fitting by using the approach of Garofalo

3.2. Simulation Results

In Figure 9, the development of the temperature, the residual stresses with and without creep and the creep strain are illustrated versus the time for one node on the surface in the middle of the notch. The temperature has a declining gradient. At the beginning of the

heating the decline of the residual stresses is dependent on the decrease of the Young's modulus for higher temperatures. After 20 s the temperature has reached a value of 250°C and creep applies, resulting in a strong decrease of the residual stresses.
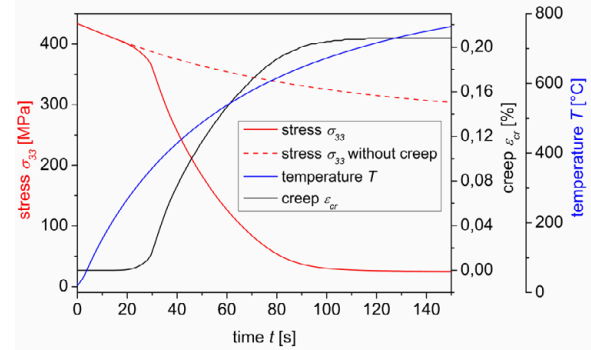
Figure 9: Development of residual stresses, creep strain and temperature over the time

Depending on the rising aging time during heat treatment, Figure 10 shows the relaxation of residual stress for several time points. Each curve presents the residual stress state versus the surface distance for specific time and temperature. It must be taken into account that the temperature also changes depending on the surface distance, but the differences are small. Furthermore, Figure 11 shows the distribution of the residual stresses along the groove. The residual stresses are mostly relaxed and nearly constant after an aging time of 1000 s.

Finally the development of the residual stresses depending on the heating rate is given in Figure 12. As a result of major time intervals for smaller heating rates, the relaxation of residual stresses starts earlier for low temperatures than for higher heating rates.

Zener-Wert-Avrami Parameters

T [°C]	250 / 350	450 / 550
σ^{RS} [MPa]	450	300
ΔH_a [J]	$2{,}29 \cdot 10^{-19}$	$4{,}43 \cdot 10^{-19}$
C [1/s]	$1{,}67 \cdot 10^{6}$	$9{,}23 \cdot 10^{16}$
m [-]	0,108	0,221
—	—	—

Garofalo Parameters

T [°C]	250 / 350	450 / 550
σ^{RS} [MPa]	450	300
ΔH_N [J]	$2{,}18 \cdot 10^{-19}$	$4{,}096 \cdot 10^{-19}$
A [1/s]	0,0022	$9{,}88 \cdot 10^{9}$
B [1/MPa]	0,0186	0,0243
n [-]	3,636	1,91

Table 3: Fitting parameters for both creep approaches
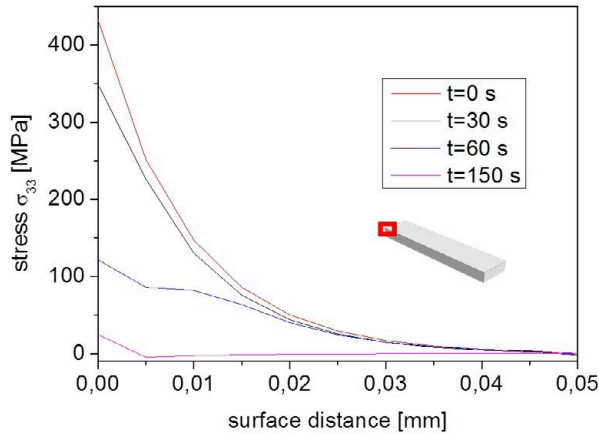
Figure 10: Relaxation of residual stress depth distribution after different times
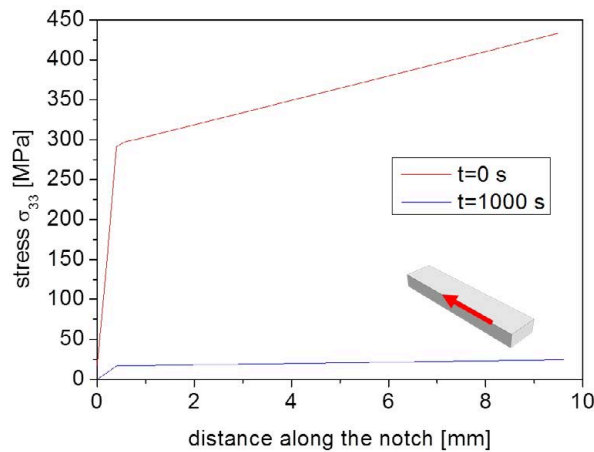
Figure 11: Residual stress along the groove for two different time points during the heating step of the simulation
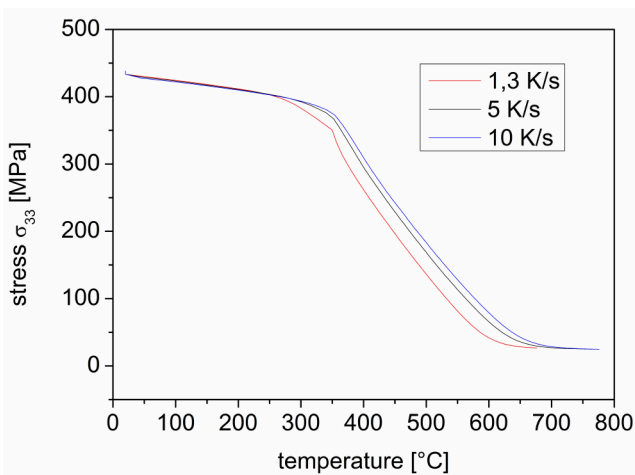
Figure 12: Development of residual stresses versus the temperature for different heating rates in a surface node in the middle of the geometry

The distortion due to thermal relaxation was determined by the occurring creep. With a maximum of $2 \cdot 10^{-5}$ mm in x-direction (see Figure 13), distortion is negligibly small considering the volume element.
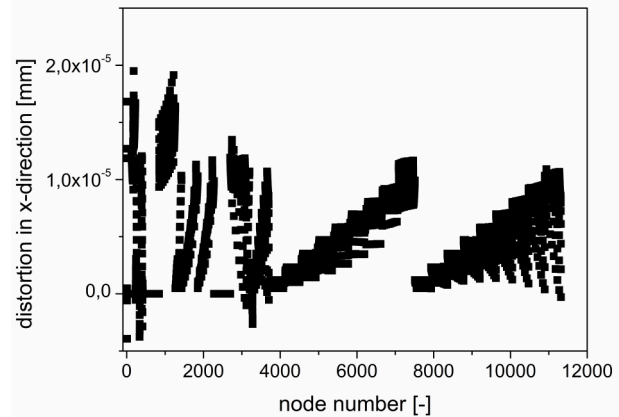
Figure 13: Node distortion in x-direction resulting from the heating

4. Summary

The residual stresses, induced by soft-machining, can be considerably reduced by thermal relaxation occurring during the heating step of a case hardening treatment, but not relaxed completely. As a result of the experimental determination and the simulations, the thermal relaxation increases especially on the surface and its immediate proximity, with higher temperatures and longer aging times. The distortion due to the heat treatment is negligibly small for the investi-gated geometry and the residual stress state considering the observed volume ratio.

5. References

[1] E. Macherauch, D. Löhe: Grundlagen der Wärmebehandlung, In: G. Spur, T. Stöferle (eds.), Handbuch der Fertigungstechnik Bd. 4 Wärmebehandeln, Teil 2, Hanser Verlag, München, 1987, pp. 592-639

[2] H.-U. Plaul, W. Grimm, R. Chatterjee-Fischer: Wärmebehandlung von Stählen, In: G. Spur, T. Stöferle (eds.), Handbuch der Fertigungstechnik Bd. 4 Wärmebehandeln, Teil 2, Hanser Verlag, München, 1987, pp. 715-920

[3] V. Läpple: Wärmebehandlung des Stahls, Verlag Europa-Lehrmittel, Haan-Gruiten, 2010

[4] E. Macherauch, P. Müller: Das sin²ψ-Verfahren der röntgenographischen Spannungsmessung, Zeit-schrift für angewandte Physik 13, 1961, pp. 340-345

[5] O. Vöhringer: Abbau von Eigenspannungen, In: V. Hauk, E. Macherauch (eds.), Eigenspannungen, DGM-Informationsgesellschaft, Oberursel, 1983, pp. 49-83

[6] Naumenko K, Altenbach H. Modeling of creep for structural analysis. Berlin [u.a.]: Springer; 2007

Graduate School 1483
Process Chains in Production:
Interaction, Modelling and Assessment of Process Zones
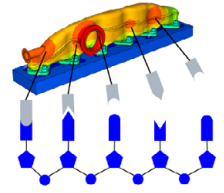
Examination of component state changes caused by machining with multi-edged tools for the example of broaching

V. Schulze, Rüdiger Pabst, J. Osterried

wbk Institute of Production Science, KIT Karlsruhe Institute for Technology

Components with complex geometries like transmission elements are applied in many cases in the automotive industry. These are manufactured with multi-staged process chains. Within a process chain there is an influence of the previous sub-process on the observed process, as well as an influence on the following sub-process due to pre-machining. Process chains often include sub-processes that use multi edged cutting tools like milling or broaching. The broaching process is a part of the process chain for a demonstrator component. Its modeling takes sequential cuts into account. The simulation sequence for multiple maching includes a transfer of component states between work piece models for every cutting edge machining the work piece. Part of the examination is the influence of the number of cutting edges and of process parameters on the component state.

FEM, sequential cuts, surface layer.

1. Introduction

Technical components used in powertrains like gears or shift collars (see Figure 1) have complex geometries in order to fulfill their requirements. These components have notches and are highly stressed when in use.
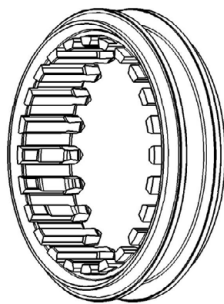
Figure 1: Demonstrator component shift collar

The interaction of high loads, notches and the components residual stress state is important for the durability. Therefore residual stress states have great importance for an economic application of components [1]. The residual stress state depends on how the component has been manufactuered. Due to the complex geometry the manufacturing is done with a multi-stage

process chain. Besides a heat treatment, gears are typically produced by machining processes like milling, or broaching for the inner geometries, see Figure 1. These processes use tools with multiple cutting edges, so that the component condition, especially the surface layer, is affected by sequential cutting. The Research Training Group 1483 "Process Chains in Manufacturing: Interaction, Modeling and Assessment of Process Zones" examines a process chain for a shift collar chosen as a demonstrator component, Figure 2.
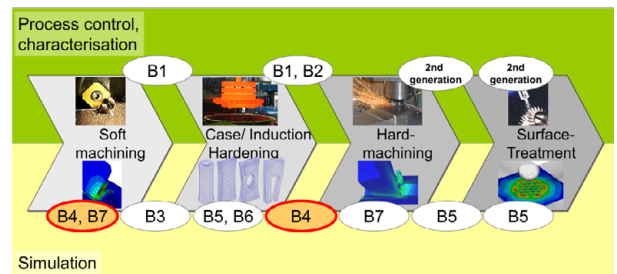
Figure 2: Process chain and related research topics

The inner gearing of the shift collar is machined by the broaching process. The broaching tool used in the experiments has 89 cutting edges that are arranged one behind another along the length of the tool. The Research Training group 1483 deals on the one hand with process control and characterization, and on the

other hand with the simulation of all processes within the process chain. The work of topic B4, which is related to this paper, is about the simulation of soft and hard machining done by broaching, see Figure 2. For the examination of such a process chain, the key questions are:

- What component state results from a single sub-process?

- How are these states changed by a specific process?

- What influence has the linking of processes?

The aim for Topic B4 is to model sequential cutting for the example of broaching, to examine the influence of process parameters e.g. the number of cutting edges and to examine the influence of a initial component state due to premachining.

2. Procedure of numerical study

Generally the work is divided into three main levels. First of all, the chip formation itself has to be modeled by means of finite element method. Therefore a small section of the workpiece and the geometry of the cutting edge have to be modeled, see Figure 3. The model includes a description of the material behavior and the material separation in front of the cutting edge. To get high detailed information about the characteristics of the surface layer, small element sizes are required.
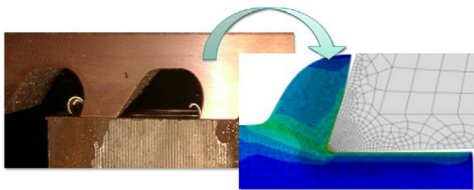
Figure 3: Modelling the single chip formation

The next step takes the single chip formation model and upgrades it to simulate multiple chip formations by connecting several single simulations one after another, see Figure 4.
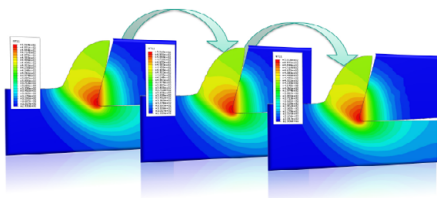
Figure 4: Modelling multiple chip formation

The third level is about predefining component states that are defined by the previous sub process e.g. heat treatment and how they influence the result of the

machining process concerning residual stress states in the surface layer, see Figure 2.

3. Simulation of broaching process

3.1. Modelling of single chip formation

For the simulation of the chip formation with a single cutting edge, a 2D model is built up for ABAQUS/ Standard. The model consists of a small workpiece section and a cutting edge, depicting an orthogonal cut situation. The discretization of the geometries is done with thermo-mechanical coupled elements of type CPE4T. Both geometries, workpiece and tool, have an initial mesh, whereas the tool mesh is not changed during the simulation. The displacement of the work piece is constrained on the lowerside in the model, resulting in a relative motion to the tool whose position is fixed. The demonstrator component, a shift collar, is made of SAE 5120 steel. For the simulation of the soft machining sub process, a material model describes the behavior of SAE 5120 in a normalized state, see [2] for information regarding material parameters. Due to the high temperatures and high deformation rates occurring during machining, the yield stress is modeled dependent on the strain rate and the temperature. The yield stress consists of a thermal and an athermal flow stress part and also models a material softening at high temperatures, see Figure 5 and [3] for details about the corresponding equations as implemented in the model.
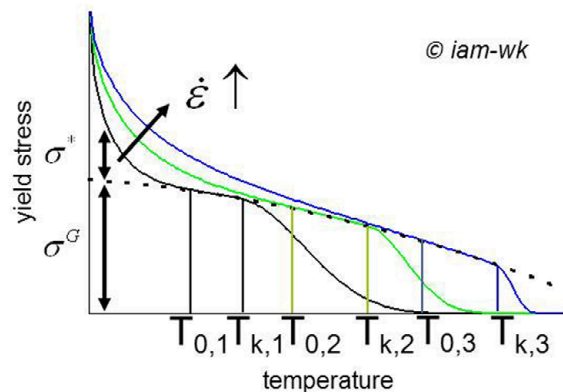
Figure 5: Modelling of yield stress

The material separation in front of the cutting edge is realized by a remeshing technique. The mesh along the cutting face and the tool flank is frequently remeshed during the chip formation, see Figure 6, right. Remeshing leads to very small element edge sizes from 1-2 μm. The advantage of remeshing is that there is no loss of information, because no elements are deleted at the materials surface. As a result, the surface layer can be characterized with a high resolution, e.g. with stress profiles, see Figure 6, left. So the

local component state can be determined very accurate.
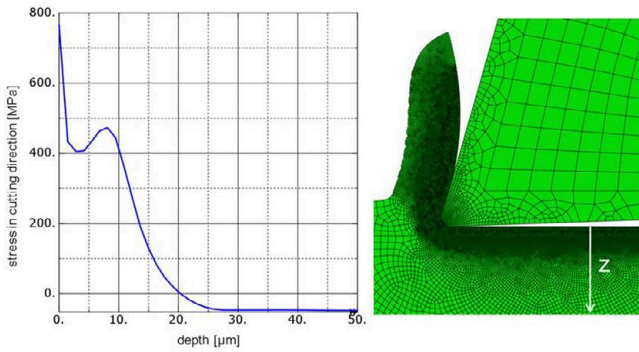
Figure 6: Remeshing (right) and resulting high detailed stress profiles (left)

3.2. Modelling of multiple chip formation

There are different methods to model sequential cutting. One approach is to model one workpiece and several cutting edges [4]. In project B4 one tool model and one workpiece model serve for the simulation. The number of simulated cutting edges is only limited by computation time. In order to simulate the cutting operations of several cutting edges, a so called transfer module and a control module are added. The transfer module uses an implementation in Python and Fortran. Its function is to extract the component state after each single chip formation and to set it as an initial state on a new, unmachined work piece model, see Figure 7.
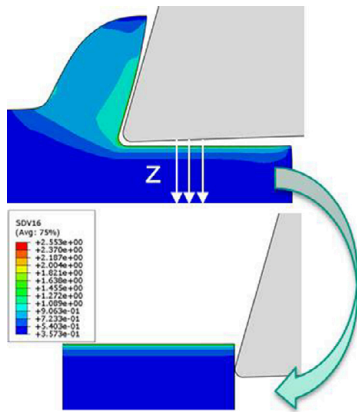
Figure 7: Transfer of component states

The control module, which is a script written in Perl, starts several simulation steps and controls process parameters like the distance between two following cutting edges (the pitch t) and the number of cutting edges on the virtual tool. The simulation sequence begins with a single chip formation. Afterwards the tool is removed out of the contact with the work piece in an additional simulation step to respect the pitch t. For a time span dependent on cutting velocity and pitch t the work piece is mechanically unstressed.

Then the component state is extracted. Stress components, plastic strain and nodal temperatures are read out along several equidistant paths along depth z and are averaged (Figure 7). By means of linear interpolation the component state is then mapped as an initial state on a new unmachined work piece model as shown in Figure 7. Extracted and mapped information show a very good match, as the initial mesh on the new work piece model also has small element edge sizes, see Figure 8. After the transfer is done, the control module starts a new simulation sequence with the next cutting edge of the broaching tool continuing the sequential cutting.
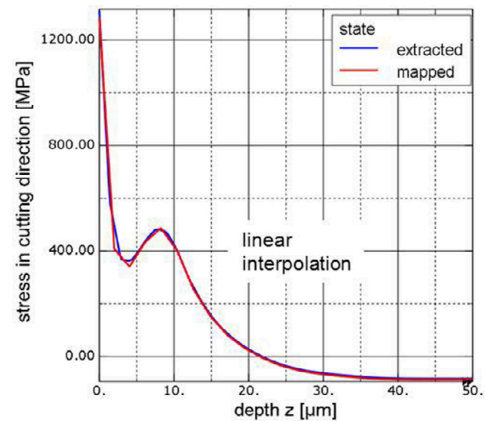
Figure 8: Linearinterpolation of depth profiles

3.3. Variation of process parameters

For the simulation of sequential cutting up to five single chip formations have been linked following the method explained in chapter 3.2. To identify the influences withtin the sub process soft machining, in this case broaching, some process parameters have been varied including the number of cutting edges, cutting velocity, uncut chipping thickness and the tool starting temperature.
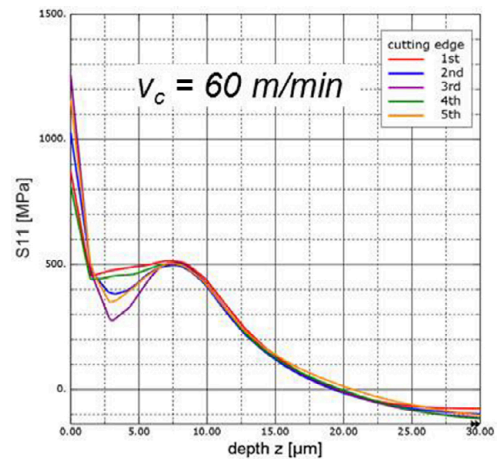
Figure 9: Residual stress profile, v_c=60 m/min

Figure 9 shows residual stress profiles in cutting direction for the example of cutting velocity v_c=60 m/min and five simulated cutting edges. It can be seen that the stresses beneath the surface change dependent on the number of cutting teeth. Variations of v_c show that this effect increases with increasing cutting velocity. Also different cutting thicknesses were simulated, e.g. in Figure 10.
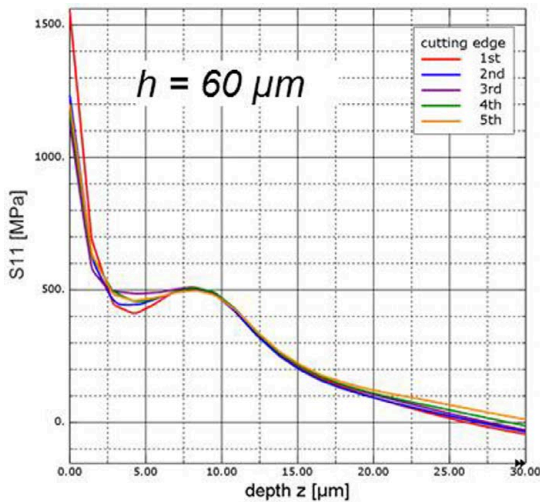
Figure 10: Residual stress profile, h=60 µm

The number of cutting egdes shows an effect on the surface layer. Stresses on the surface change and the overall depth of the tensile stresses is reaching deeper for an increasing number of teeth. The specific local minimum at about 5 µm of depth is less distinctive for increasing cutting thicknesses.
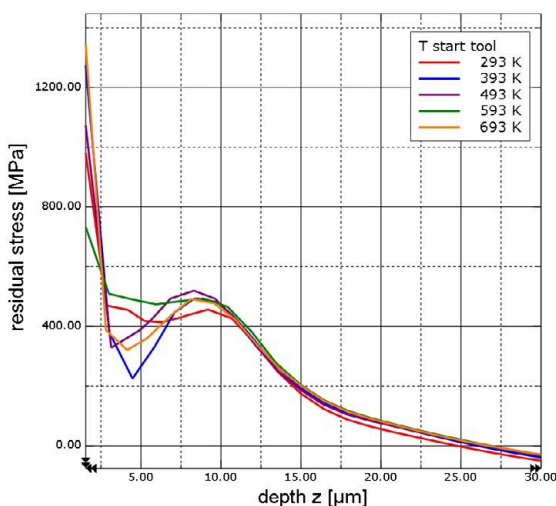
Figure 11: Residual stress profiles, variation of $T_{tool,start}$

Due to the fact that the cutting distance in the experiments is much more longer than it can reasonably be simulated when very small element sizes are required, the tool starting temperature is also interesting to look at. With a tool starting temperature higher than room temperature, a situation may be simulated as it is expected after a longer virtual cutting distance. Different starting temperatures lead to different residual stress profiles beneath the work piece surface, see Figure 11.

4. Conclusion

A 2D simulation model for a single chip formation is built up. It uses a strain rate and temperature dependent material model for SAE 5120 to compute the yield stress during chip formation. Realisation of material separation done by remeshing allows to define very small element edge sizes. The local component state can be determined in high detail. The model also respects multiple chip formation which is part of the sub process broaching. The influence of process parameters on the component state after machining is examined. Future work will continue the variation of process parameters. Also the influence of different predefined component states caused by previous sub processes within the process chain will be examined.

5. Acknoledgement

6. References

[1] Guo, Y.B., Liu C.R., 2002, FEM analysis of mechanical state on sequentially machined surfaces, Machining Science and Technology, 6(1), pp. 21-41

[2] Schulze V., Osterried J., Meier H., Zanger F., 2011, Simulation of multiple chip formation when broaching SAE5120 low alloy steel, Sintra, Portugal, Trans Tech Publications, J.C. Outeiro, Modelling of Machining Operations - Proceedings of the 13th CIRP Conference on Modelling of Machining Operations, Switzerland, pp. 37-45

[3] Weber M., Hochrainer T., Gumbsch P., Autenrieth H., Delonnoy L., Schulze V., Löhe D., Kotschenreuther J., Fleischer J., 2007, Investigation of Size-Effects in Machining with Geometrically Defined Cutting Edges, Machining Science and Technology, Oct-Dec 2007, Vol. 11 Issue 4, pp. 447-473

[4] Li J.L., Jing L.L., Chen M., 2009, An FEM study on residual stresses induced by high-speed end-milling of hardened steel SKD1, Journal of Materials Processing Technology 209, pp. 4515-4520

Graduate School 1483
Process Chains in Production:
Interaction, Modelling and Assessment of Process Zones
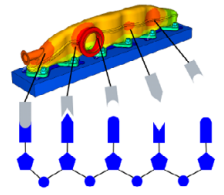
Process simulation of dual frequency induction surface hardening

M. Schwenk, J. Hoffmeister, V. Schulze

Institut for Applied Materials – Materials Science and Engineering, Karlsruhe Institute of Technology

A 2-D computational model of simultaneous dual frequency induction hardening has been developed. Process specific aspects such as nonlinear magnetic material behavior as well as phase transformation kinetics of quenched and tempered AISI 4140 are considered. Induction surface hardening experiments have been conducted for validation purpose. Measuring methodologies used to extract input data such as the magnetic material behavior and current is presented. Metallurgical characterization and hardness profiles are compared with the results obtained from simulation. The temperature history, hardness depth profile and hardness distribution are in good agreement.

Process Simulation, Dual Frequency, Magnetic Properties

1. Introduction

Surface hardening is used to improve the fatigue strength and wear resistance of components [1]. Surface hardening generally leads to high compressive residual stresses in the hardened zone, further contributing to an increase in fatigue strength. Within the group of thermal surface hardening processes, induction hardening is important. Is easy to integrate in product lines and has a high reliability allowing mass production at low costs as compared to other surface hardening processes [2]. Although induction surface hardening is widely used in industry, process understanding of the combined induction heating and quenching is not well developed and mainly based on "trial and error" [1]. For this reason, numerical modeling using the finite element method (FEM) has become an essential field of research.

This paper presents a simultaneous dual frequency simulation model using the finite element method. They are validated in terms of temperature and hardness distribution. The finite element electromagnetic-thermal model considers the nonlinear magnetic behavior as well as process specific phase transformation kinetics during the induction heating process. The developed dual frequency model is based on electromagnetic sub-models, consisting of medium and high frequency simulations.

At the beginning of this paper, an overview of the experimental work conducted is given, describing the extraction of input and validation data needed for modeling. Thereafter the computational model is presented, describing the sub-modeling strategy implemented in order to simulate the dual frequency induction hardening. Also the consideration of magnetic nonlinearity within the model is discussed. The results include the validation of the numerical model for both single frequencies as well as for the dual frequency

2. Experimental Work

The finite element simulation of a manufacturing process chain requires experimental data in terms of process parameters as well as material and validation data. For surface induction hardening the current applied to the induction coil is the main process parameter to be determined, since no direct measurement at the coil is possible. Temperature dependent magnetization curves are necessary in order to consider the influence of the nonlinear magnetic behavior on the eddy current losses. For the model validation, in-situ temperature measurements were conducted at the surface as well as inside the specimens using thermocouples [3]. Furthermore, hardness depth profiles were extracted from separate specimens in order to allow a direct comparison of the mechanical properties after the induction surface hardening. For a global validation, the

cylindrical specimens were cut in axial direction and etched for comparison of microstructure distribution.

2.1. Current Measurement

The current was measured by using a so-called Rogowski coil, which allows the measurement of alternating currents. In case surface hardening, the coupling distance between the induction coil and work piece is too small for direct measurements. For this reason the output current was measured directly at the output of the frequency converter.

Figure 1 shows predefined input current in % over measured output current. Due to the experimental setup, the medium frequency (MF) was 12 kHz and the high frequency (HF) 325 kHz. The linear correlation of the current setting and the measured output current underlines the validity .
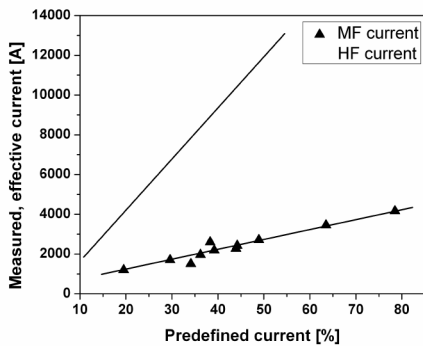
Figure 1: The current measured for the medium (MF) and high (HF) frequency induction heating experiments with MF = 12 kHz and HF = 325 kHz.

2.2. Magnetization curve

The nonlinear magnetic behaviour is described by the magnetisation curves. The temperature dependent measurement were conducted using an annular ring made of ASIS 4140 as shown in Figure 2. The primary coil is used for excitation and the secondary coil to pick up the induced magnetisation or rather magntic flux. The evaluation of the magnetic field H and the magnetic flux B leads to the characteristic hysteresis curves as shown in Figure 3.
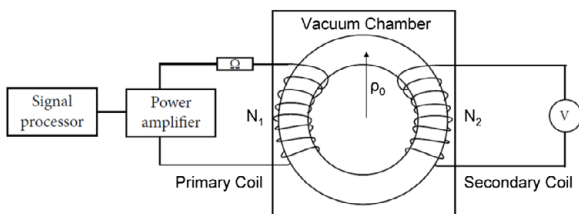
Figure 2: Experimental setup for measuring magentisation curves
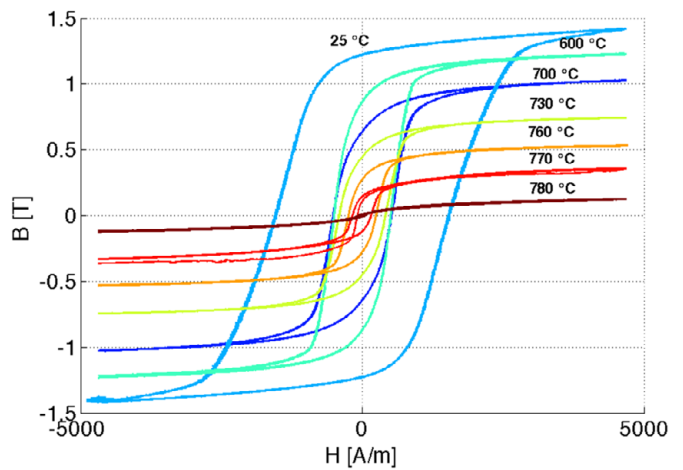
Figure 3: Temperature dependent hysteresis curves of AISI 4140

3. Computational Model

The computational model of induction surface hardening consists of an electromagnetic-thermal and a thermo-mechanical analysis. The electromagnetic-thermal model is developed using MSC.Marc®, whereas the thermo-mechanical model was developed in ABAQUS/Standard®. In order to allow decoupling into two separate analyses – electromagnetic-thermal followed by thermo-mechanical – the stress influence onto phase transformation as well as deformation heat was neglected. In order to consider the latent heat, the austenitization model developed in [4] is used in the electromagnetic-thermal model, ensuring that decoupling of the two models loses no information.

The modeling strategy implemented for the dual frequency induction hardening simulation is shown in Figure 4. At the beginning of each time step, an iterative determination of the fictitious, equivalent permeability is conducted in order to capture the influence of the nonlinear behaviour on the heat source distribution. The current parameters used for the electromagnetic simulations are taken from the single frequency experiments conducted. Thereafter, the heat sources for the medium and high frequency power portions of the dual frequency are calculated. Both heat sources are superimposed and used in a thermo-metallurgical simulation. The time step used for this simulation is automatically adjusted until the global temperature change does not exceed 10 K. This convergence criteria can be set arbitrary or might be adjusted in regions of interest, such as during the phase transformation or around the Curie temperature. Once the convergence criteria is met, the new material data and temperature field is transferred to the electromagnetic simulation, where the fictitious permeability is determined again.
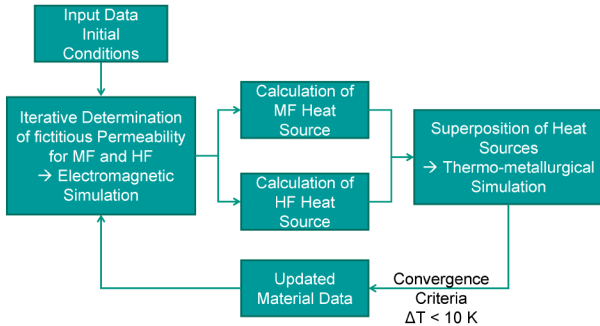
Figure 4: Flow diagram of dual frequency induction hardening simulation

Figure 5: Surface temperature distribution for dual frequency induction hardening

4. Results and Discussion

The comparison of the numerical and experimental results has been conducted locally by comparing the surface temperature and hardness depth in the middle of the cylindrical specimen and more globally by looking at the micro section, revealing the hardness distribution.

Two dual frequency experiments were conducted, labelled SDF 1 and 2. For SDF 1, the specimen was heated for 500 ms (486 ms effective heating time) using 30 % medium frequency (MF) current and 50 % high frequency (HF) current at the same time. In the case of the SDF 2 sample, the time was reduced to 400 ms (384 ms effective) and only the HF current was changed to 60 %. Figure 5 shows the surface temperature for the first 2 seconds of the whole hardening cycle in order to emphasise the fairly good agreement between the simulation and the measured values.

The intial temperature gradient due to the high heating rates is captured fairly well by the simulation. In case of SDF 1, the temperature measurement shows two tilts at around 500 °C and around the Curie temperature. The former may be explained by the temperature measurement, since there is no physical reason to explain the bump. No such behaviour has been observed for the high frequency experiments and so it must be attributed to the measurement or heating equipement. The dreased power input due to the loss of ferromagnetism of the surface layer is captured by the simulation, been marked by an abrupt decrease in heating rate. Furthermore, the simulation matches the measurements during the holding time (exponential temperature decrease due to heat conduction into the workpiece) fairly well and only shows some major differences once the quenching fluid wets the thermocouple. However, this mismatch may be amplified due to the boundary condition assumed. In both cases, the quenching was activated 0.5 sec after the end of the heating cycle. The exact holding time may vary somewhat due to the quenching system.
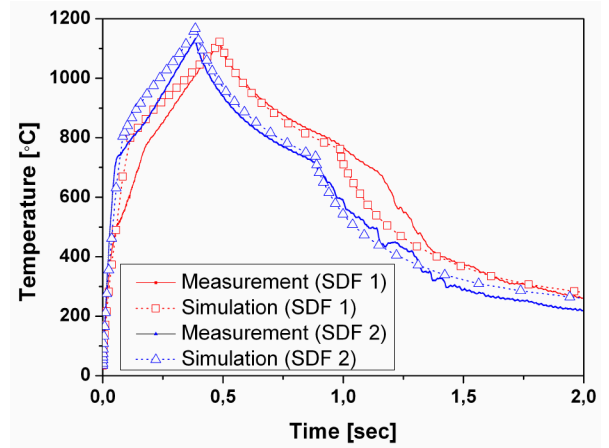
Figure 6 shows the hardness distribution along the center line in radial direction of the cylindrical specimen. The hardness measurements vary due to the relative low testing load of 100 g as well as the influence of residual stresses which may influence the measurements within the range of 10-20 % [5]. In both cases, the effective hardness depth matches the measured one, however the transition zone shows differences, revealing that the simulation can not account for the relative step gradient caused by this process. This may be explained by the descritization and hence the mesh used. It may be assumed that a finer mesh allows a better resolution and therefore also a more precise prediction.

Figures 7 and 8 give a more global view of the process model and its capability of predicting the final results. In both experiments, the specimens were not aligned perfectly with the induction heating coil, which can be seen by the unsymmetric hardness pattern at the ends.
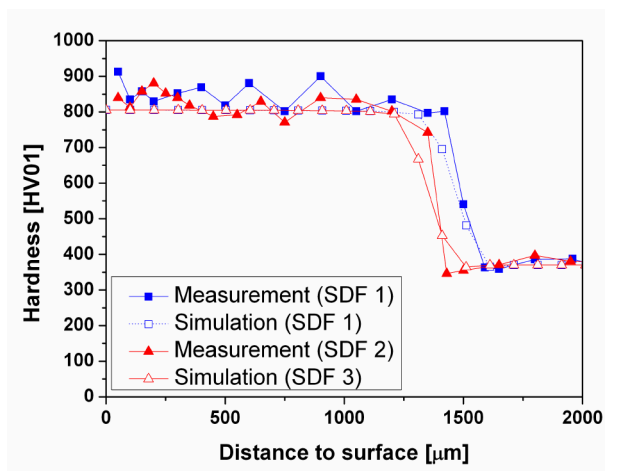
Figure 6: Hardness depth profile

The magnified ends shall underline the good predictability of the model. Although the dual frequency simu-

lation consists of the superposition of two separate heat soures, the final results show that this simplification gives good results, especially under the consideration that no interaction of the magnetic fields caused by each frequency portion is considered.
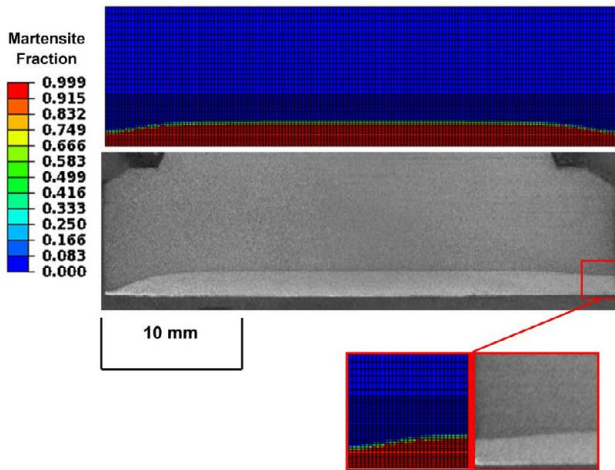
Figure 7: Micro section for SDF 1
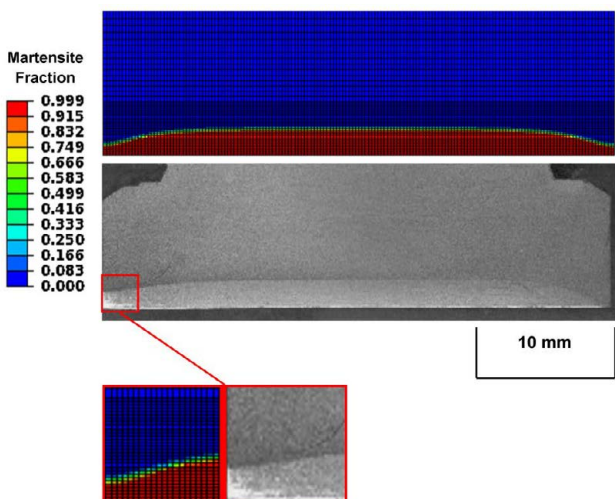
Figure 8: Micro section for SDF 2

5. Conculsion and Outlook

The present dual frequency induction hardening model is capable of predicting the hardenss distribution. However, first results have shown that the residual stresses are overestimated by over 50%. This may be explained by the mechanical model as well as the material data used so far, since only isotropic hardening with material data from literature were used.

In order to consider the residual stresses from the preceding maching process, the decoupling of the electromagnetic-thermal and thermo-mechanical model will be used further. In order to allow sufficient resolution of the relative high stress gradients within a surface layer of only 30-50 μm, the workpiece needs to be meshed much finer than needed for the electromagnetic modelling and hence increasing computational time extensively. In order to reduce the computational time, the thermal history due to induction heating will be mapped onto a much finer mesh, where only the workpiece needs to be considered. This will minimize the computational effort while at the same time considering effects from preceding processes. Since the mapping occurs from a coarser to finer mesh, the loss of information may be neglected.

6. References

[1] Zoch H-W. Randschichtverfestigung - Verfahren und Bauteileigenschaften. HTM. 1995; 50(5):287–94.

[2] Grum J. Induction Hardening. In: Handbook of Residual Stress and Deformation. ASM International; 2002. p. 220–47.

[3] Schwenk M, Strauss T, Hoffmeister J, Schulze V. Data acquisition for numerical modelling of induction surface hardening – process specific considerations. Proceedings of 26th ASM Heat Treating Society Conference, Cincinnati, 31. Oct. - 2. Nov. 2011; 26(1):167–76.

[4] Miokovic T, Schwarzer J, Schulze V, Vohringer O, Lohe D. Description of short time phase transformations during the heating of steels based on high-rate experimental data. JOURNAL DE PHYSIQUE IV. 2004 Dez; 120:591–8.

[5] Gibmeier J, Scholtes B. About the Effect of Residual Stresses on Microhardness Readings. Materials Science Forum. 2002; 404-407:349–54.

Graduate School 1483
Process Chains in Production:
Interaction, Modelling and Assessment of Process Zones
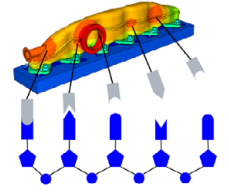
Simulation of diffusion and microstructure evolution in the Fe-C system

Authors: C. Qin[1], A. Choudhury[2], B. Nestler[1,2]

1: Institute of Materials and Processes (IMP) Karlsruhe University of Applied Sciences Moltkestr. 30, D-76133 Karlsruhe, Germany

2: Institute of Applied Materials (IAM), Karlsruhe Institute of Technology (KIT), Haid und Neu Str. 7, D-76131 Karlsruhe, Germany

We use a phase-field model to simulate phase transformations occurring during the heat treatment in the Fe-C alloy by utilizing the thermodynamic and kinetic properties of the material system. At first we develop a diffusion model for simulating grain boundary (GB) diffusion, which occurs during the carburization in austenite, in a static polycrystalline structure. Profiles of the carbon concentrations obtained in simulations are compared with experimental data. Next, we develop a multi-phase field model which allows to simulate the phase evolution of a multiphase system consisting of austenite, ferrite and a stoichiometric compound, i.e. cementite. We study the two-dimensional growth of lamellar pearlite structure in the austenite matrix at the eutectoid concentration and compare the growth velocity as a function of spacing between lamellae, with results obtained from an analytical model. In addition, we investigate the growth of cementite at grain boundaries from the initial polycrystalline austenitic structure.

Keywords: phase-field method, phase transformation, steel microsturcture.

1. Introduction

The phase transformations and the accompanying evolution of the microstructure determine the mechanical properties of the material. Therefore, modelling and simulation of the formation and evolution of the microstructure is an important task for the material research. The computational simulations which are based on thermodynamic principals are becoming very useful tools within this domain.

The purpose of the present work is to develop a model in the framework of the phase-field method for the simulation of isothermal diffusion-controlled phase transformation in the binary Fe-C system. Such a model may be utilized in applications, like the monitoring of heat treatment processes. The simulation results demonstrate that the ensemble properties of the material microstructure can be predicted if appropriate parameters are applied.

2. Phase field method

The phase-field formulation of the multi-phase system is based on the grand potential functional defined as,

$$\Omega(T, \mu, \boldsymbol{\phi}) = \int \Psi(T, \mu, \boldsymbol{\phi}) - (\varepsilon a(\boldsymbol{\phi}, \nabla \boldsymbol{\phi}) + \frac{1}{\varepsilon} \omega(\boldsymbol{\phi})) dV$$

where $\boldsymbol{\phi}$ is the vector of phase parameters that describe the volume fraction of the present phases. Ψ represents the grand chemical potential density. a is gradient energy potential and ω is the surface energy potential. ε is a length scale parameter which is related to the phase interface thickness. The phase evolution is determined by the minimization of the grand potential functional which gives rise to the evolution equation,

$$\tau \varepsilon \frac{\partial \phi_\alpha}{\partial t} = \varepsilon (\nabla \cdot a_{,\nabla \phi_\alpha} - a_{,\phi_\alpha}) - \frac{1}{\varepsilon} \omega_{,\phi_\alpha} - \Psi_{,\phi_\alpha} - \lambda$$

where λ is the lagrange parameter to maintain the constrain $\sum_{\alpha=1}^{N} \phi_\alpha = 1$ and τ is the phase-field relaxa-

tion parameter. The driving force of mass transport is the gradient of chemical potential μ which is utilized to write the evolution function for concentration as

$$\frac{\partial c_i}{\partial t} = \nabla \cdot \left(\sum_{j=1}^{K-1} M_{ij}(\boldsymbol{\phi}) \cdot \nabla \mu_i \right).$$

Here the M_{ij} is the mobility parameter matrix.

3. Carburization simulation

The interstitial diffusion of carbon in austenite (γ-Fe) is a technologically very important process and has been intensively investigated via experiments and modelling.

In polycrystalline microstructure, diffusion is enhanced in the grain boundary (GB) region due to lower activation energy of the diffusing atoms. Although the grain boundaries only take a minor fraction of the total volume of the material, rapid grain boundary diffusion can contribute significantly to the overall diffusive transport, expecially at lower temperature where the bulk diffusion is much less active.

In this work, we assumed that carbon atoms have a higher diffusivity in the austenite GB region. Consequently the final carbon concentration profile is a combined result of GB diffusion and a relative minor bulk diffusion.

3.1. Modeling and simulation of carbon boundary diffusion

A regular solution approach is chosen to model the free energy function of austenite which reads,

$$f_\gamma = Ac^2 + Bc + C + RT(c\ln c + (1-c)\ln(1-c))$$

$$\mu(c) = \frac{\partial f_\gamma}{\partial c} = Ac + B + RT\ln\left(\frac{c}{1-c}\right).$$

The data of free energy was acquired from the thermodynamic databank CALPHAD. The data points and the fitted curve are shown in Figure 1. The increased diffusivity at the GB is realized through the formulation of diffusion coefficient with spatial dependence written as,

$$D_i = \sum_{\alpha=1}^{N} D_i^\alpha(c)\phi_\alpha + \frac{1}{\varepsilon}\sum_{\alpha<\beta} D_i^{\alpha\beta}(c)\phi_\alpha\phi_\beta.$$

The diffusion coefficient of carbon in austenite is strongly dependent on the local carbon concentration. We choose a modified Leyens formulation for the effective diffusion coefficient [1]

$$D_{eff.}(c_C) = 0.43exp(-16.533 + 1.25c_C^{1.5})$$

which provides a good agreement with the measured data.
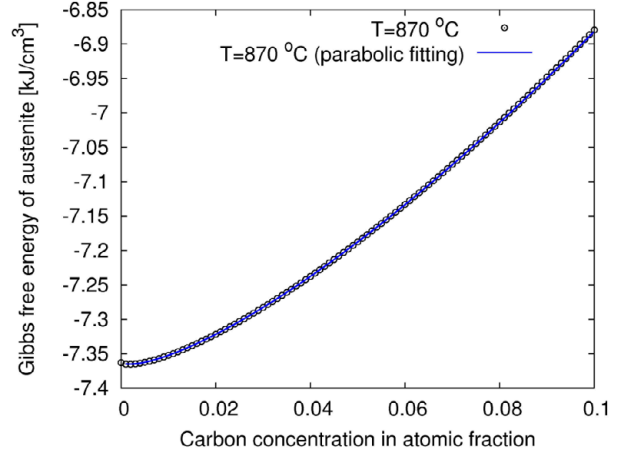
Figure 1 Fitting free energy from CALPHAD data

Based on the effective diffusivity, the diffusion coefficients in the GB and bulk were determined with the help of the Maxwell-Garnett equation [2]

$$D_{eff.} = \frac{D_{GB}(3-2g)D + 2gD_{GB}}{gD + (3-g)D_{GB}}$$

where g is the volume fraction of GB. Figure 2 shows the separated diffusion coefficients with $\frac{D_{GB}}{D} = 2$.
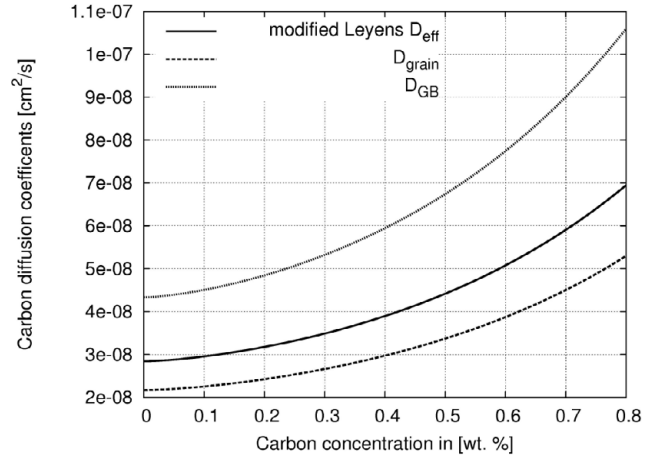
Figure 2 Diffusion coefficients with dependence of concentration

3.2. Comparison of the simulation and the experimental result

The calculated carbon concentration profiles from simulations are shown in Figure 3 along with the measured profile. There is generally good agreement between the two calculated profiles. The upturn in the C profile near the surface of the workpiece due to decrease of the surface carbon potential is observed in both simulation and measurement profiles.
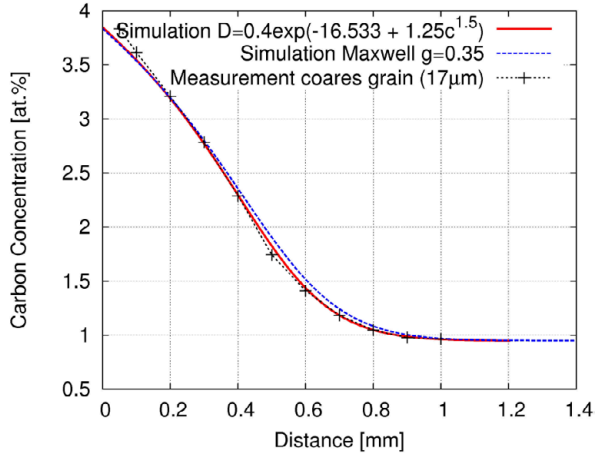
Figure 3 Carbon concentration profile at 870°C, Predictions vs. experimental result

4. Growth of grain boundary cementite

During the carburizing process at lower temperatures above the eutectoid temperature, the high carbon concentration in the near surface region may cross the maximum carbon solubility of austenite and into austenite (γ)-cementite (ϑ) two-phase region, which would lead to the nucleation and growth of cementite.

The cementite (Fe$_3$C) is metastable, but remains as a compound indefinitely at room temperature, with very slow kinetics involving decomposition into α-F and carbon (graphite) at 650 – 700 degrees celcius (occurring very slowly, within several years).

4.1. Multiphase Model of multi-component system

The Calphad data and the derived functions of free energy f for the two phases austenite f_γ and cementite f_ϑ are shown in Figure 4. We use a parabolic type of free energy using the following properties,

1. the derivative $\frac{\partial f_\vartheta}{\partial c}$ at the equilibrium (c=0.25) equals the slope of the common tangent between the free energy functions of austenite and cementite;

2. the curvature of the parabola for the cementite is kept large. Here we choose the value of the curvature at the vertex 500 times larger than the value of the austenite curve.

In the interface region, we assume that the existing phases have different carbon concentrations, which satisfy the relation $c_C = \sum_{\alpha=1}^{N} c_C^\alpha \cdot h(\phi_\alpha)$, where the individual phase concentrations are functions of the chemical potential μ_α of each phase.
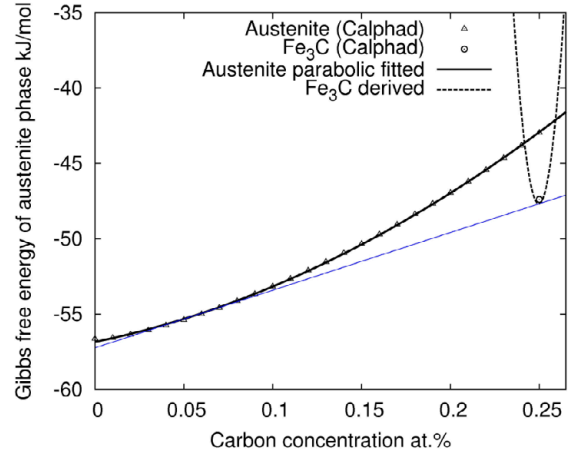
Figure 4 Free energy function of austenite and cementite

4.2. Simulation result

The fitted free energy functions of the two phases in simulation are given by,

$$f_\gamma = 17.7\, c_C^2 + 3.4\, c_C - 8.0 \ [\text{kJ/cm}^3]$$

$$f_\vartheta = 8870.8\, c_C^2 - 4430\, c_C + 546.4 \ [\text{kJ/cm}^3]$$

In a 2D-simulation domain, 4 circular nuclei of cementite phase are placed in the grain boundary area. To simulate the carburizing situation, a higher carbon concentration level is set on the left boundary of the domain. Figure 5 displays the grain structure at beginning and the end of the simulation. Because of the abundant carbon flux, the cementite phase in the near surface region attains a higher growth velocity.
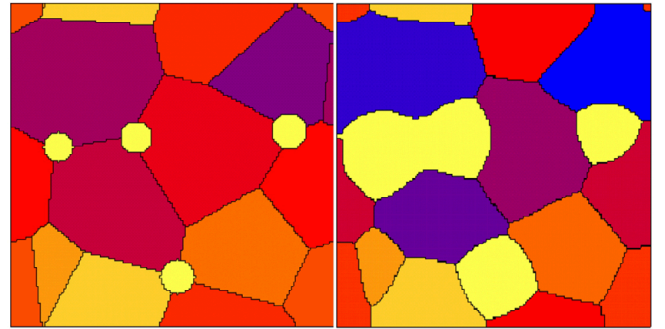
Figure 5 Simulation of growth of the cementite phase

5. The Austenite-Pearlite transformation

The multi-phase field model is next utilized to simulate the cooperative growth of eutectoid pearlite in binary carbon steel. Figure 6 shows a schematic pearlite microstructure. The carbon diffusion coefficients of ferrite and cementite are given a higher value than that of the austenite.
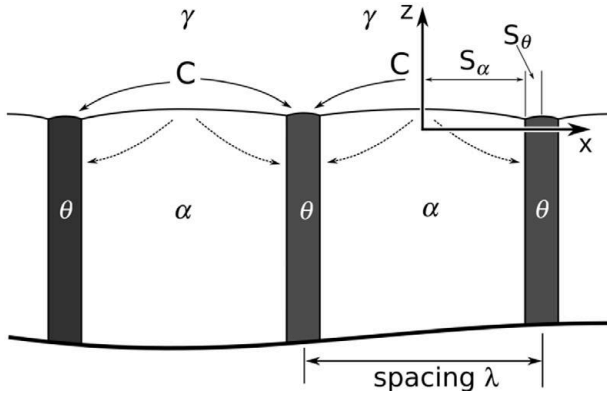
Figure 6 Scheme of lamellar pearlite structure. Phase θ is cementite; λ is the lamellar spacing factor. The arrows represent the possible transport paths for carbon diffusion.

5.1. Development of model

For simplicity the free energy function of the phases (α, γ, ϑ) within the concentration region are approximated by parabolas of the form, ($f_\alpha(c_C) = A_\alpha c_C^2 + B_\alpha c_C + C_\alpha$) through curve fitting (Figure 7). The chemical potential μ_C is obtained from $c_C = \sum_{\alpha=1}^{N} c_C^\alpha(\mu_C) \cdot \phi_\alpha$.
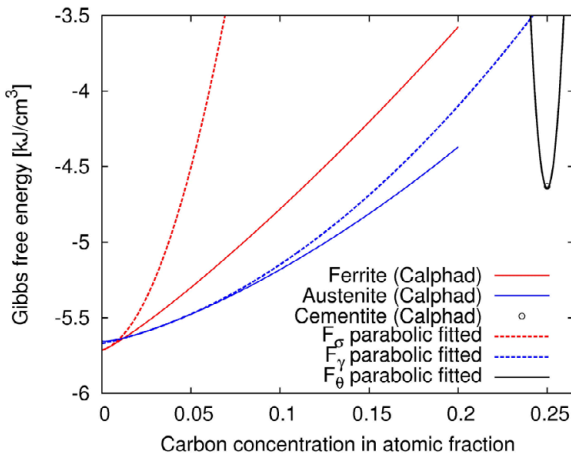
Figure 7 Fitting free energy functions T=975K.

5.2. Simulation results and disscusion

For each undercoolings a series of simulation with various lamellar spacings is performed (Figure 8).
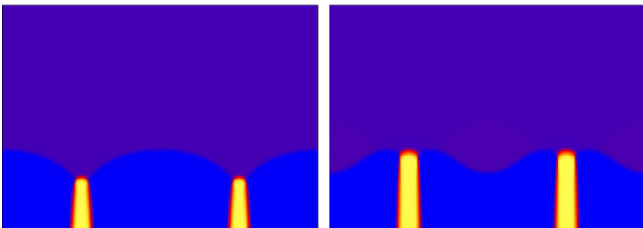
Figure 8 The stable growth front of pearlite lamellar structure, left: λ=0.2μm; right: λ=0.8μm.

The cementite behind the transformation front continues to grow because of the carbon flux inside the ferrite.

The growth velocity from the simulations are shown in Figure 9. The lines represent results of an analytic formulation based on Jackson-Hunt model [3, 4]. The simulation results show a similar dependence of growth velocity upon lamellar spacing as the analytic model.
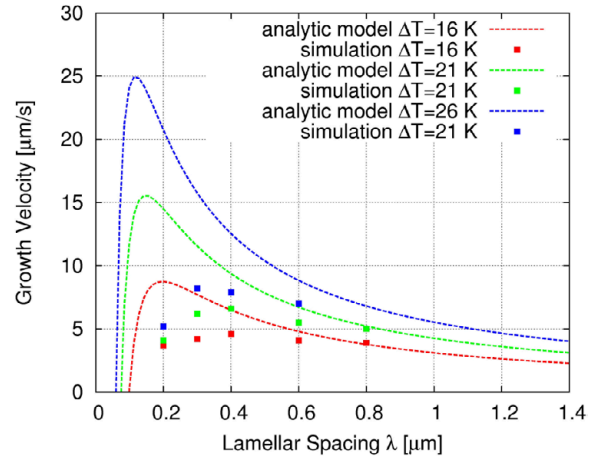
Figure 9 Dependence of growth velocity of pearlite upon lamellar spacing.

6. Conclusion

The evolution of microstructure in Fe-C alloys was simulated using a multi-phase field model for different concentration and temperature regions in the phase diagram. The presented phase transformation model can be applied to determine the influence of various process and material parameters, e.g. grain size, lamellar spacing, undercooling. A multi-component extension of the model should indeed be capable of predicting other solid phase transformations occurring during the treatment of steel.

7. References

[1] G. Leyens, G. Woelk, J. Wunning: Arch. Eisenhuttenwes. 47:385 (1976).

[2] J. C. Maxwell-Garnett: Philos. Trans. Royal Soc. London Vol. 203 (1904) p.385.

[3] K. A. Jackson, J. D. Hunt: Metal. Soc. of Aime 236, (1966) 1129–1141.

[4] A. Nemeth, Bachelor thesis: Analytische und numerische Studie über lamellares Wachstum von Perlit im Fe-C-System, (2011).

Graduiertenkolleg 1483
Prozessketten in der Fertigung:
Wechselwirkung, Modellbildung und Bewertung von Prozesszonen
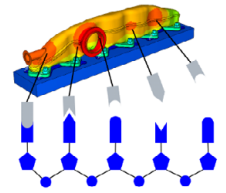
Development of a 2D remeshing methodology for finite element simulations with ABAQUS/Explicit and its application to metal microcutting modeling.

V. Pavlova, M. Weber

Institute of Applied Materials (IAM-ZBS), KIT - Karlsruhe Institute of Technology

It has always been of significant practical importance to find out more about the complex technological process of metal cutting. Despite active research in this area, there still appears to be a lack of information on what exactly happens during the chip formation: material behavior at the primary and secondary shear zones as well as effects which take place under different process conditions. Due to high temperature gradients and high deformation rates, it becomes very difficult to attain reliable experimental data to get an insight into the process. Only recently, simulation tools including finite element method opened more options to have a closer look into it.

The aim of B7 project at Graduate School 1483 is to develop an improved methodology for chip formation simulation under ABAQUS/Explicit. It will consequently allow enriching current research of extreme conditions during metal cutting process as well as depicting sophisticated contact condition with consideration of high friction coefficients. This research includes the analysis of the influence of process and material parameters on the process values and stability. The region of interest is the primary shear zone where most of the reaction and interaction take place. In order to achieve the goal of running FE-simulations with variation of parameters, a new remeshing tool developed at IAM-ZBS has been adopted as a basis for improvement and application on the metal cutting simulation model. The latter is continuously validated by experimental material and process data obtained from fellow B-projects.

remeshing, finite element simulation, metal cutting, friction, abaqus, explicit

1. Introduction

Due to industrial importance of metal shaping processes especially for production of components with complex geometry and fine tolerances, it becomes important to research and consequently optimize the manufacturing. The conditions inside the material during the machining process are extreme, i.e. there appear large plastic deformations of the material in combination with high strain rates which are rarely accessible in any other process.

So far the finite element method is the most suitable treat to the complexity issue when analytical methods fail [4]. Such a simulation should take into account a mechanism of material separation process in front of the tool tip, friction between the chip and the work-piece as well as heat generated by plastic deformation

and friction [1], and the resulting change in material behavior [2].

Due to severe distortion of finite elements when intense shear takes place the initial mesh becomes totally unsuitable from the accuracy point of view and has to be changed in order to stay with the minimal computational error [4]. This problem can be avoided with an appropriate remeshing method applied to the simulation. Such a remeshing algorithm essentially involves a new and better-conditioned mesh replacing the old one, as well as an accurate transfer of quantities at nodes and Gaussian points to the new mesh. The development and rapid improvement of the methodology of running a continuous FE-simulation under ABAQUS/Explicit is the subject of this paper.

2. Methodolgy

2.1. Remeshing method

Presently, there is no remeshing technique provided in ABAQUS/Explicit. It also does not contain the useful functionality as in ABAQUS/ Standard. In order to achieve the required simulation results quality under ABAQUS/Explicit, remeshing is done externally with the help of binaries and Python scripts. ABAQUS is basically used for generating a new mesh. The main difference between this remeshing method and re-finement remeshing used in ABAQUS/Standard lies in the fact that refinement by definition increases the number of degrees of freedom, and therefore, a computational effort as well. The new algorithm allows remapping the last relevant state variables onto the completely new mesh, while keeping the original element size [3].

The development of the method evolved into a set of fully automized working routines with a possibility to stop-restart the simulation flow when neccessary.
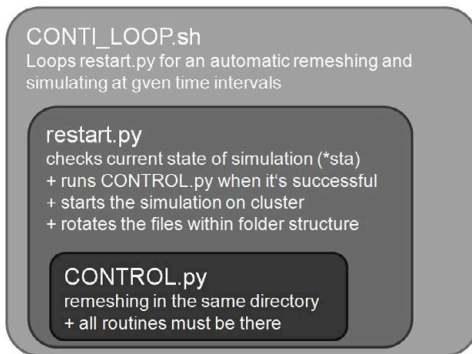
Fig. 1: stop-restart remeshing automatization

The main advantage of using ABAQUS/Explicit is the guaranty of convergence, provided the time steps are stable. Thus, it is suitable for higly dynamic non-linear problems, as is the simulation of chip formation. A disadvantage is the time consumption for such a simulation in comparison to implicit method. There are three ways to address this problem: reduction of remeshing time via parallelization, accuracy compromise, and reduction of degrees of freedom amount via local remeshing in the zone of interest.

2.2. Remeshing time

The main time consumption during remeshing process (fig. 2) is created by remapping algorithm and error analysis. Depending on number of degrees of freedom (nodes) and state variables it can take up to 10% of subsimulation (run) calculation time.
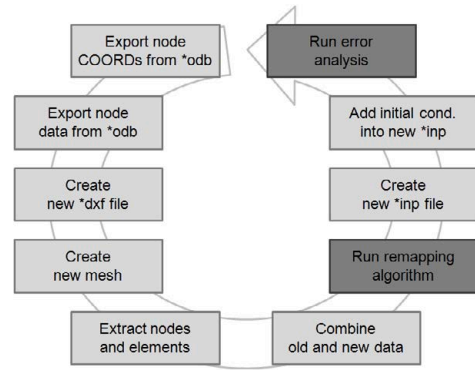
Fig. 2: remeshing workflow

Both remapping and consequent error analysis have been parallelized. Moreover, the arror analysis runs after the new input file is generated and the next sub-simulation has been started. This provides a consider-able reduction of overall remeshing time.

2.3. Calculation time

There are two ways of improving the accuracy of a simulation running with an explicit solver: manually setting the stable time increment smaller than the one suggested by CFL-criteria [7] or/and setting a high iteration number for material related calculations. Both ways lead to an immediate increase of overall calculation time.
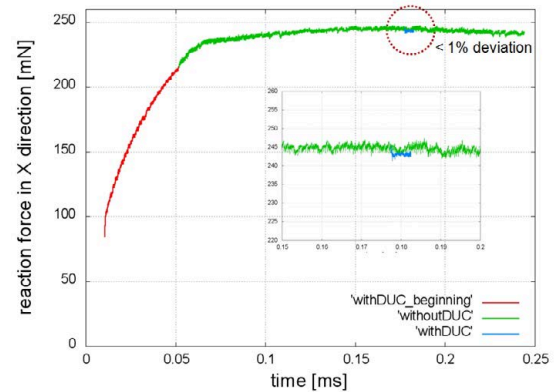
Fig. 3: influence of incrementation

An investigation of the influence of incrementa-tion has been performed and shown in fig. 3. The calcula-tion starts with direct user control (DUC) setting the stable time increment one order smaller (5-e10) than the one calculated with CFL (4-e9). Solution scatter-ing increases when the simulation continues without DUC, i.e. CFL-controlled (green). As soon as the sta-bility of chip formation is achieved one subsimulation is chosen to be the start of a parallel thread of calcula-tion with DUC (blue).

Afterwards, the mean lines for both curves on a selected straight time interval have been compared. There was a deviation of less than 1% , but the solution with smaller incrementation took triple the time. Therefore, a compromise between accuracy of a solution and calculation cost is necessary and is shown to be affordable.

2.4. Mesh quality

Another way to reduce the calculation time is the reduction of number of degrees of freedom to be calculated. One of the approaches is to use structured mesh where possible. In areas where the results quality is not the first priority, mesh can be coarser than at the relevant primary shear zone (fig. 4).
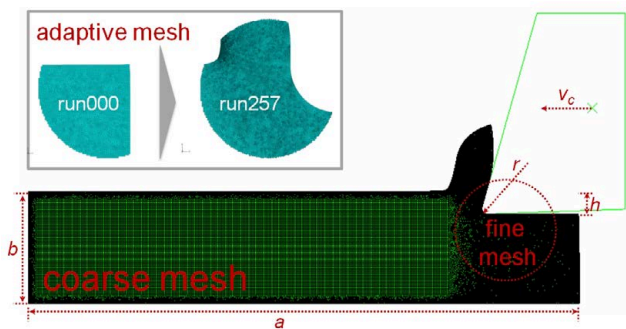
Fig. 4: complete and local remeshing strategies

The disadvantage of this approach is the increase of number of elements as the cutting proceeds further, since the area with free mesh increases. Therefore, a better way is to remesh only adaptively (locally). It also reduces the time required for remapping.

3. Simulation and Discussion

3.1. Explicit vs. Implicit

In order to compare the methods for orthogonal metal cutting 2D FE-simulation under ABAQUS/ Standard [9] and ABAQUS/Explicit, two models have been built with equal and same material, geometry and process parameters. A rectangular block (a x b) has been cut h deep with a rigid tool with the cutting edge radius r and cutting velocity v_c with friction coefficient μ (fig. 4).

Table 1: geometry and process parameters

a[μm]	b[μm]	h[μm]	r[μm]	v_c[m/min]	μ
1000	200	40	10	200	0.35

The material behavior for 20mnCr5 used in the simulation, has been equivalently modeled in subroutines

UHARD (for ABAQUS/Standard) and VUHARD (for ABAQUS/Explicit).

The main difference in the modeling concerns the relative workpiece-tool motion. In the implicit model the workpiece moves against the tool, which is also discretized. Whereas, in explicit model the tool moves against the workpiece. The tool is set to be a rigid body. Another difference is inertia, which is considered in explicit model and excluded in the implicit one [6].
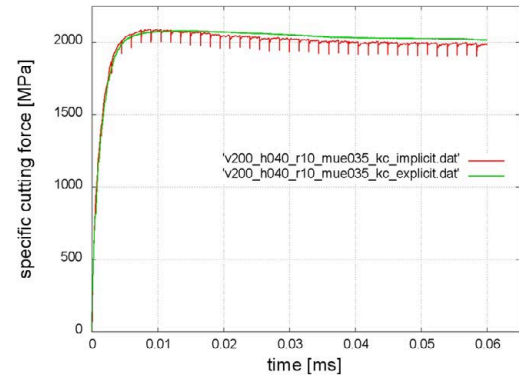
Fig. 5: specific cutting force for explicit/implicit

Hence, the two behavior patterns interesting for detailed research were the influence of inertia and simulation stability at high friction. The simulation showed the explicit curve (filtered with a floating mean filter) lies above the implicit one (fig. 5) as was predicted due to inertia. Implicit model does not allow simulating with high friction coefficients whereas explicit one does. Explicit simulation takes a longer time. A more detailed analysis is a subject of a separate article in cooperation with [9].

3.2. Friction

The possibility to simulate with sophisticated contact condition and high friction with μ over 0.5 is one of the advantages of using ABAQUS/Explicit, which can outweigh the computational cost.

A model with AISI 1045 material parameters described in VUMAT subroutine is used to run simulations with different friction coefficients. Experimental data obtained with pin-on-disc-tribometer at different starting temperatures and without lubrication [8] is taken as a basis for investigating the stability of simulation under high friction (fig. 6).
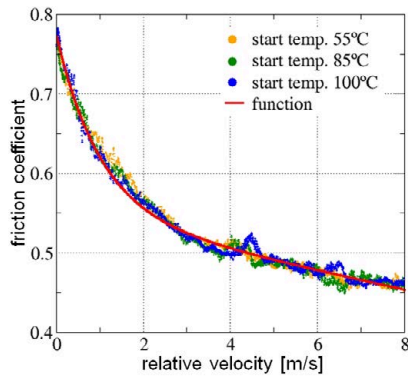
Fig. 6: friction experimental data [8]

A metal block is cut 100μm deep with 100μm rounded tool tip at 100m/min cutting speed. The simulation is run frictionless and with friction coefficients 0.58 and 0.75 (fig. 6, 7)
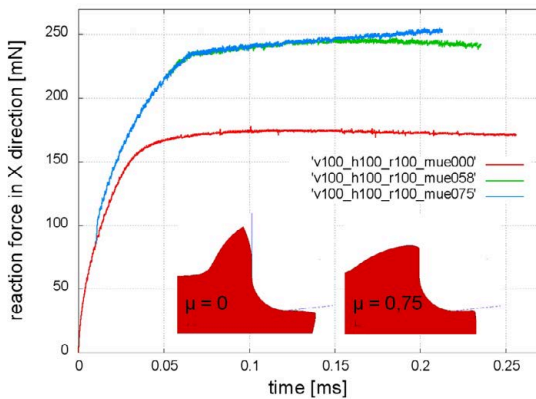
Fig. 7: variation of friction coefficient

Simulation has been proven to run effortlessly at friction up to 0.75 with minor increase of scattering (no mathematical filters applied here).

4. Summary and conclusion

A continuous automatic remeshing method has been brought to a fully automatic functionality. It was rapidly improved to be a part of a method of simulating metal cutting process under extreme conditions with ABAQUS/Explicit.

The two examples in 3.1 and 3.2 were shown to analyse the methodology developed for simulating orthogonal metal cutting with an explicit method. Firstly, equal implicit and explicit models have been compared to investigate the effects and stability of simulations. Results show that an implicit method can deliver a qualitative solution in a considerably shorter time, while explicit method allows stable simulating with high friction. Secondly, an investigation on simulating with high friction has been performed in more detail.

This allows research of stick-slip effect and material behavior at the rigion next to the tool tip.

There have been several ways of decreasing the time consumption shown here, which include parallelization of the remapping algorithm, reduction of degrees of freedom (nodes) for calculation, compromise on solution precision via FLC/DUC and iteration index, adaptive remeshing and mesh quality/orientation. Nevertherless, there is still potential for decreasing the computational cost.

5. References

[1] Autenrieth, H., Weber M., Schulze V., Gumbsch P., Fleischer J., 2007, Influence of friction and process parameters on the specific cutting force and surface characteristics in micro cutting, Proceedings of the 10th CIRP International Workshop on Modeling of Machining Operations, 539-546.

[2] Autenrieth H., Weber M., Deuchert M., Schulze V., 2009, Investigation of scaling behavior of subsurface work hardening and residual stress states after micro-cutting using finite element simulation, Proceedings of the 12th CRIP Conference on Modeling and Machining Operations, 639-646.

[3] Pavlova V., Weber M., 2010, Vorstellung eines 2D-Neuvernetzungsalgorithmus für Finite-Element-Simulationen mit ABAQUS/Explicit, Graduierten-kolleg 1483 Prozessketten in der Fertigung, Hrsg. R. Pabst, B. Nestler, V. Schulze, Shaker Verlag, 75-78

[4] Bäker M., 2004, Finite Element Simulation of Chip Formation, Materialwissenschaft, Shaker Verlag.

[6] SIMULIA, ABAQUS Analysis User's Manual: v. 6.9, 2009, Section 6.5.4: Fully coupled thermal-stress analysis

[7] Courant R., Friedrichs K., Lewy H., Über die partiellen Diff. Gln. der mathematischen Physik, 1928, Mathematische Annalen 100(1): 32–74

[8] Wallstabe R., Schneider J., K.-H. Z. Gahr, 2009, Influence of Surface Modification on Dry Friction Performance of Alumina Mated Against Steel, Wiley-VCH Verlag GmbH & Co. KGaA, 369-375

[9] Osterried J., B4 project at Graduate School 1483

Graduate School 1483